Carnegie Mellon University

CARNEGIE INSTITUTE OF TECHNOLOGY

THESIS

SUBMITTED IN PARTIAL FULFILLMENT OF THE REQUIREMENTS

FOR THE DEGREE OF Doctor of Philosophy

TITLE Elucidation of the Structure Formation of Polymer-Conjugated Proteins in Solution and Block Copolymer Templates

PRESENTED BY Rachel L. Ferebee

ACCEPTED BY THE DEPARTMENT OF

Materials Science and Engineering

Michael Bockstaller 02/19/2016
ADVISOR, MAJOR PROFESSOR DATE

Gregory S. Rohrer 02/23/2016
DEPARTMENT HEAD DATE

APPROVED BY THE COLLEGE COUNCIL

Vijayakumar Bhagavatula 02/24/2016
DEAN DATE

Elucidation of the Structure Formation of Polymer-Conjugated Proteins in Solution and Block Copolymer Templates

Submitted in partial fulfillment of the requirements for
the degree of
Doctor of Philosophy
in
Materials Science & Engineering

Rachel L. Ferebee

B.S., Materials Engineering, Rensselaer Polytechnic Institute
M.S., Materials Science and Engineering, Carnegie Mellon University

Carnegie Mellon University
Pittsburgh, PA

February 16, 2016

Copyright Notice

Acknowledgements

I would like to thank my advisor, Professor Michael Bockstaller, who has provided great guidance and support over the last four years. You have been very kind and patient in helping me become a better researcher, and I am very grateful for all of the time and energy you have devoted to my growth as a person and to the evolution of my research.

I would like to express my gratitude for my committee members: Professor Chris Bettinger, Professor Adam Feinberg, and Professor Newell Washburn. You have been so supportive of my efforts, and your insights have helped shape the work that has been done.

This work was supported by the Defense Threat Reduction Agency (via Grant #HDTRA1-13-C-0003), the NSF-IGERT program via NSF-0966227, and the John and Claire Bertucci Fellowship.

I would like to recognize my collaborators through the DTRA grant at FLIR Systems, Inc., Cornell University, Akita Innovations, and Terapore Technologies, Inc. In addition, I would like to acknowledge the IGERT Principal Investigator, Professor Jeanne VanBriesen, and all of the professors and students who made my time as an IGERT trainee special.

My sincere thanks goes to Dr. Ilhem Hakem, who has devoted a great deal of time and effort to this project and has been so welcoming and kind during my time at CMU.

I would like to thank Dr. George Fytas and Dr. Amelie Koch of the Max Planck Institute for Polymer Research for being such great hosts in Mainz, Germany as well as for providing invaluable assistance in conducting light scattering measurements and analyzing the results.

Thank you very much to Tom, Jason, Adam, and Bill for technical support and all the time you spent teaching me valuable skills. I also would like to acknowledge Roxann, Jeanna, Suzy,

Neetha, Kelly, Angie, Anita, and Marygrace for your support in everything form ordering chemicals to scheduling the defense date.

I would like to thank my professors at CMU and at RPI who gave me a strong foundation in the field of materials science to build upon in my graduate studies. I could not have pursued a Ph.D. without the support I received from Professor Dan Lewis at RPI, who gave me my first experience in a lab and who supported my applications to summer internships and to graduate schools.

I extend special thanks to past and present members of the Bockstaller group who have provided me with so many fond memories, including but not limited to camping, RazzyFresh, and Ali Baba lunches: Jess, Hyung Ju, Jihoon, Jeet, Sudarshan, Clare, Mike, Bongjoon, Lauren, Jaejun, Alei, Zhao, Zongyu, Jianan, Xin, Chaitrali, Lu, Beibei, Guangyuan, Soo, Shuo, Yi, Danli, Qingyun, and Tong. You have made the lab such a positive environment, and I have really cherished the time spent alongside each of you.

Thank you also to all of the undergraduate students who have worked with me the past few years: Chidimma, Ashley, Mariana, Haylie, Christine, Denny, Maggie, and Derek. You have all done such great work and have been so fun to be around. I wish you the best in your future endeavors and know that you will continue to do great things.

I have a special place in my heart for my officemates past and present: Joe, Steph, AB, Proud, Bongjoon, and Lauren. We have had so many great times talking about everything under the sun and playing soccer/basketball. I'll really miss you guys.

Of course some of my friends have already been mentioned here, but there are many dear people who have helped shape the past few years: Suze (I'm looking forward to our weddings!), Ellen, Aimon, Maiolei, Zenille, Lauren, Lily, Chetali, Noey, Brian, Prabhat, Howie, Melissa, and Mike

(thank you for the countless insights and hours of conversation). You are so special to me, and I thank you for the times we have shared together (and look forward to our future exploits).

I would like to show my appreciation for my entire family (especially my parents, grandparents, and Mr. and Mrs. Ginsberg) and specifically: thank you to Clare for helping me to be a better person everyday, thank you to Rosalie for the encouragement and the countless funny dog photos, and thank you to Katie and Dave for all the invitations to your place for food and games. You have collectively taught me that there is room in life for more than just school and research.

Lastly, I would like to thank my fiancé, Chris Maher, for endless love and support every step of the way. You have helped in many practical ways from formatting my documents to cooking and cleaning, but beyond this you have always been there to listen and to help me put things into perspective. I could not have finished this Ph.D. without you, and I look forward to a lifetime of memories together.

Abstract

The broader technical objective of this work is to contribute to the development of enzyme-functionalized nanoporous membranes that can function as autonomous and target selective dynamic separators. The scientific objective of the research performed within this thesis is to elucidate the parameters that control the mixing of proteins in organic host materials and in block copolymers templates in particular. A "biomimetic" membrane system that uses enzymes to selectively neutralize targets and trigger a change in permeability of nanopores lined with a pH-responsive polymer has been fabricated and characterized. Mechanical and functional stability, as well as scalability, have been demonstrated for this system. Additional research has focused on the role of polymeric ligands on the solubility characteristics of the model protein, Bovine Serum Albumin (BSA). For this purpose BSA was conjugated with poly(ethylene glycol) (PEG) ligands of varied degree of polymerization and grafting density. Combined static and dynamic light scattering was used (in conjunction with MALDI-TOF) to determine the second virial coefficient in PBS solutions. At a given mass fraction PEG or average number of grafts, the solubility of BSA-PEG conjugates is found to increase with the degree of polymerization of conjugated PEG. This result informs the synthesis of protein-conjugate systems that are optimized for the fabrication of block copolymer blend materials with maximum protein loading. Blends of BSA-PEG conjugates and block copolymer (BCP) matrices were fabricated to evaluate the dispersion morphology and solubility limits in a model system. Electron microscopy was used to evaluate the changes in lamellar spacing with increased filling fraction of BSA-PEG conjugates.

Table of Contents

List of Tables

Table of Figures

Chapter 1: Introduction

1.1 Motivation

Tunable membranes are of great interest for many applications, including breathable protection garments and filtration devices. One route toward the fabrication of nanoporous membranes that has attracted significant attention in the literature is based on the self-assembly of block copolymer thin films. For example, Mayes *et al.* fabricated a thin film membrane of PVDF-*g*-POEM, which phase separated to form channels of PEO in a semicrystalline PVDF matrix. The diameter of the PEO channels could be tuned based on the composition of a water/organic solvent mixture flowed through the membrane. The channels were able to successfully size-separate gold nanoparticles ranging from 3-10 nm in diameter [1]. Nanoporous polymer membranes are of interest across a wide range of separation applications because the nano-pore dimension generally allows for highly permeable and breathable films while at the same time enabling the size-selective separation of nanoparticles of biomolecular compounds. To further extend the range of separation of nanoporous membranes to small molecular systems – while retaining the high breathability of nanoporous structures – is a high value research objective in the context of next generation protective gear.

The work described in this document is part of a larger collaboration with industry and Cornell University working toward the realization of self-regulatory membranes used for breathable protective garments for military applications. The concept relies on the fabrication of nanoporous polymer membranes by the controlled non-solvent induced precipitation of a triblock copolymer and subsequent solvent evaporation (a process first invented by Peinemann and coworkers) [2]. The resulting films exhibit a two-layered structure comprised of a sponge-like substrate layer

(with characteristic feature sizes in the mm range) and a thin top-layer with nanopores that can be tuned in the 5-20 nm range by variation of the polymer and casting conditions [3–6]. Figure 1-1 depicts a scanning electron micrograph of a representative nanoporous membrane fabricated based on poly(isoprene-*b*-styrene-*b*-4 vinyl pyridine).

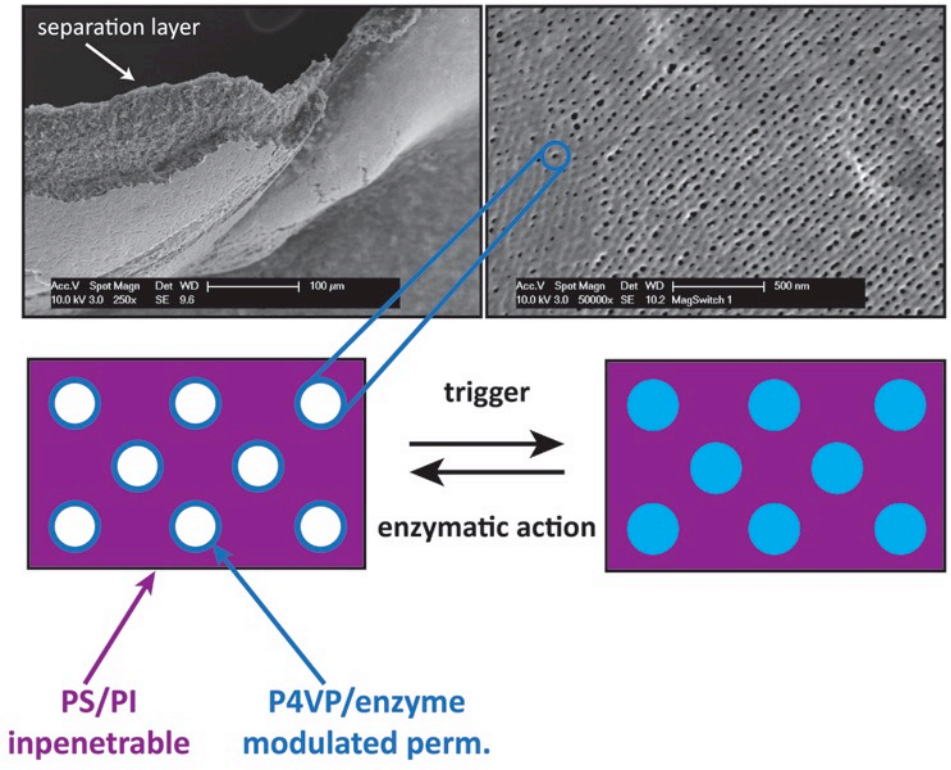

Figure 1-1. SEM micrographs showing the cross section and top view of the triblock copolymer membrane. The panel below is a schematic of the block copolymer/enzyme blend system in the pH-induced open and closed states.

In these membranes, the pores are lined with a pH-responsive polymer, poly(4-vinyl pyridine) (P4VP), that is capable of undergoing a swelling or collapsing transition by changes in pH. The vision of this project is that the pores (or block copolymer template) could be functionalized with enzymes that act as both sensors to designated chemical or biological targets and actuators that trigger a change in membrane permeability by modulating the pH of the pore interior. The

swelling of the pH-responsive pore material would effectively close the contaminated pores, preventing further contamination by the toxin, as shown in the schematic in Figure 1-2.

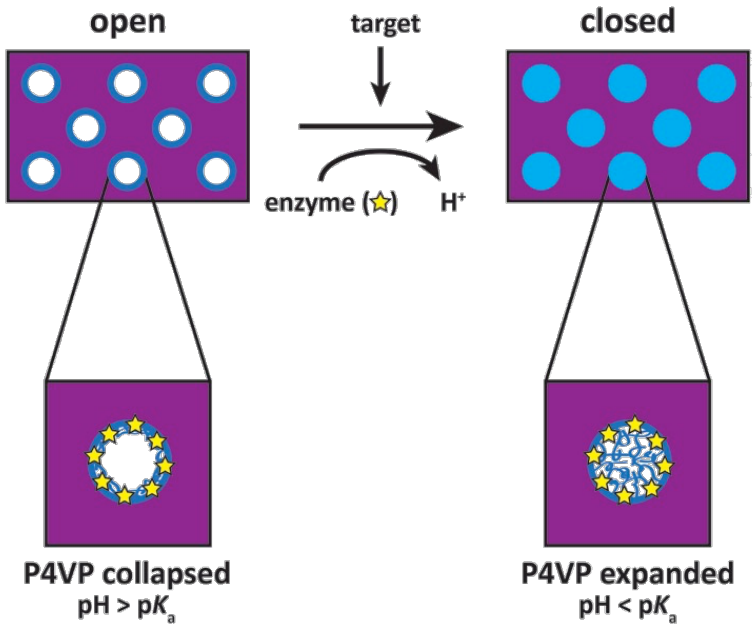

Figure 1-2. Schematic of the block copolymer/enzyme blend system in the pH-induced open and closed states.

There are many scientific challenges associated with this project, and the work included in this document focuses on two specific aspects: the solubility of polymer-modified proteins in solution and the phase behavior and structure formation of block copolymer/protein blends.

Polymer modification of proteins, and more specifically PEG modification of proteins, has been extensively studied in literature due to the beneficial aspects polymer functionalization can have on proteins for applications in drug delivery. The effect of PEGylation on the size, activity, and stability of enzymes has been studied by many researchers, and it has been shown that PEGylation increases all three of these characteristics over those of the native enzyme [7–12]. In particular, activity retention measurements performed by our collaborators at FLIR Systems have shown that the half time of thermal denaturation of a series of CB-active enzymes in aqueous and organic environments can be increased from 22 hours to 72 hours after functionalization with 3.5

kg/mol PEG [13]. Literature has shown the improvements of a wide range of physicochemical and biochemical properties attributed to polymer-modification of proteins; however, the role of graft architecture on solution behavior of proteins remains largely unknown.

A prerequisite for the fabrication of enzyme-filled block copolymer membranes is the understanding of the governing parameters that control the mixing and dispersion morphology of polymer-conjugated proteins in block copolymer matrices. A first step toward establishing this understanding is the consideration of the solubility of polymer conjugates in solvent media. As a measure of solubility, the second virial coefficient, a thermodynamic parameter that captures pairwise interactions of solutes in solvents, can be evaluated using light scattering. Although experiments measuring the second virial coefficient of individual proteins and polymers have been reported in literature, no systematic study of the effect of graft architecture (number of grafts and graft length) has been reported. Also, existing studies have suffered from the typically unknown contribution of compositional heterogeneity that is a characteristic feature of most polymer-conjugated protein systems.

Very little work on the co-assembly of block copolymers and polymer-functionalized proteins has been reported in literature. However, many studies of polymer-functionalized nanoparticles dispersed in block copolymers have been reported. Preliminary data is reported in this document regarding the effect of polymer graft architecture on the dispersion of polymer-conjugated protein systems in model block copolymers.

1.2 Research Objectives

The objective of this study is to understand the role of polymer conjugation on solubility characteristics of polymer-functionalized proteins, their compatibility in block copolymer

membrane blends, and the dispersion morphology in block copolymer/protein-conjugate blend materials. A "biomimetic" membrane system that uses enzymes to selectively neutralize targets and trigger a change in permeability of nanopores lined with a pH-responsive polymer has been fabricated and characterized. Mechanical and functional stability, as well as scalability, have been demonstrated for this system. To evaluate solubility characteristics of protein-polymer conjugates, photon correlation spectroscopy was used to determine the effect of length (molecular weight) and average number of polymer grafts on aggregation and the second virial coefficient. To evaluate blend miscibility, transmission electron microscopy was used to evaluate the lamellar spacing in block copolymer/protein-polymer conjugate blends.

1.3 Hypothesis

This study tests the following hypotheses:

1. The solubility (as measured by $A_{2,app}$) of polymer-conjugated proteins is sensitive to the graft architecture (average number, length, and volume fraction of grafts). For the particular case of PEGylated proteins in PBS solution, the second virial coefficient is expected to increase with increasing degree of polymerization and number of PEG tethers.
2. The governing parameters dictating structure formation in block copolymer/organic filler systems are expected to follow the trends observed in block copolymer/inorganic filler systems.

Chapter 2: Background

2.1 Solution Characteristics of Polymer Conjugated Proteins

2.1.1 Thermodynamics of Polymer Solutions

Polymer-modification of proteins is useful in tuning the interactions of proteins with their embedding medium, which can include solvent or polymers. Polymer-functionalization is ultimately necessary in enhancing miscibility of protein-polymer fillers in polymer matrices; however, an essential requirement is solubility in solution with the dissolved polymer.

The free energy of mixing of polymers in solution has an entropy term, which is negative and favors mixing, and an enthalpy term, which depends on the pairwise interactions between mixture components and can be positive or negative. These contributions to the free energy of mixing per site can be described by the Flory-Huggins equation:

$$\Delta\bar{F}_{mix} = kT\left[\frac{\phi}{N_A} ln\phi + \frac{1-\phi}{N_B}\ln(1-\phi) + \chi\phi(1-\phi)\right] \quad (1)$$

where k is the Boltzmann constant (1.38 x 10^{-23} J/K), ϕ is the volume fraction of species A, N is the degree of polymerization, and χ is the Flory interaction parameter. For dilute concentrations of species A in a solution of species B, the Flory-Huggins equation can undergo an expansion into a power series:

$$\Delta\bar{F}_{mix} = kT\left[\frac{\phi}{N_A} ln\phi + \phi\left(\chi - \frac{1}{N_B}\right) + \frac{\phi^2}{2}\left(\frac{1}{N_B} - 2\chi\right) + \frac{\phi^3}{6N_B}\right] \quad (2)$$

Osmotic pressure is the difference in pressure across a semi-permeable membrane that allows the flow of solvent but not the flow of species A. It can be described by the following equation:

$$\Pi = -\left(\frac{\delta\Delta F_{mix}}{\delta V}\right)_{n_A} \quad (3)$$

where V is the volume equal to $b^3 n_A N_A/\phi$, and n_A is the number of species A molecules equal to $n\phi/N_A$. By substituting the equation for volume in the denominator and taking the derivative of the free energy of mixing with respect to ϕ, the following equation can be obtained for osmotic pressure:

$$\Pi = \frac{kT}{b^3}\left[\frac{\phi}{N_A} + \frac{\phi^2}{2}\left(\frac{1}{N_B} - 2\chi\right) + \frac{\phi^3}{3N_B} + \cdots\right] \tag{4}$$

where b^3 is the volume of one molecule of species A. By replacing the volume fraction with a number density term ($\phi = b^3 c_n$), the osmotic pressure can be separated into excluded volume terms representing two-body interactions and three-body interactions:

$$\Pi = kT\left[\frac{c_n}{N_A} + \frac{v}{2}c_n^2 + wc_n^3 + \cdots\right] \tag{5}$$

where v is the excluded volume term for two-body interactions, and w is the excluded volume term for three-body interactions. When this general equation is applied to a dilute mixture consisting of polymer in solution, $N_A = N$ (polymer) and $N_B = 1$ (solvent), it takes the form:

$$\Pi = \frac{kT}{b^3}\left[\frac{\phi}{N} + \frac{\phi^2}{2}(1 - 2\chi)\right] \tag{6}$$

The second virial coefficient can be related to the χ parameter with the following relation:

$$\frac{v}{b^3} = \frac{2M_0^2}{b^3 N_{AV}} A_2 \approx 1 - 2\chi \tag{7}$$

valid near the θ temperature of the mixture [14,15]. When the χ parameter is decreased, the osmotic pressure is increased, due to the increased affinity for the polymer shown by the solvent. This behavior can also be affiliated with a positive A_2 (good solvent). In addition, an A_2 equal to zero is indicative of a theta solvent, while a negative A_2 is indicative of polymer affinity to itself over the solvent (bad solvent). This can lead to aggregation in solution to reduce the surface area of

polymer in contact with solvent. Therefore, A_2 can be related to the solubility limit of a protein-polymer conjugate in solution.

2.1.2 Static Light Scattering

The second virial coefficient, A_2, is a thermodynamic quantification of the pairwise interactions in a mixture that come from excluded volume effects. Static Light Scattering (SLS) is a commonly used tool to measure A_2 for dilute solutions. In this experiment, light is scattered by particles in a dilute solution. The light scattered is an electromagnetic field represented by the equation:

$$E(r,t) = E_0 exp[i(kr - \omega t)] \tag{8}$$

where E_0 is the amplitude, k is the wavevector, r is the position, ω is the frequency, and t is the time. The photodiode detects the intensity of the scattered light, which is proportional to the amplitude of the electromagnetic field squared:

$$I \sim |E^* \cdot E| = E_0^2 \sum_i \sum_j \langle \alpha_{ex,i} \alpha_{ex,j} exp\left[iq\left(r_i - r_j\right)\right] \rangle \tag{9}$$

where α is the polarizability and r is the position. The intensity arises from the dipole moment (the strength of which depends on the polarizability of the scattering particle) that is induced by the incident light wave. The intensity of the system components (sample, solvent, and a reference such as toluene) is used to calculate the Raleigh Ratio (R_θ) at each scattered angle:

$$R_\theta = \left(I_{sample} - I_{solvent}\right) * \frac{R_{toluene}}{I_{toluene}} * \left[\frac{n_{solvent}}{n_{toluene}}\right]^2 \tag{10}$$

where I is the scattering intensity and n is the refractive index.

The Raleigh Ratio measured can be related to sample characteristics via the equation:

$$R(q) = KcMP(q)S(q) \tag{11}$$

where $R(q) = R_\theta$, K is the optical constant, c is mass concentration, M is weight average molecular weight, $P(q)$ is the form factor, and $S(q)$ is the structure factor. The form factor describes intra-molecular scattering interference (from the same molecule), while the structure factor describes inter-molecular scattering interference (from different molecules in solution). The optical constant captures sample- and apparatus-specific characteristics:

$$K = \frac{4\pi^2 n^2 \left(\frac{\delta n}{\delta c}\right)^2}{\lambda^4 N_A} \tag{12}$$

where n is the refractive index of the solvent, $(\delta n/\delta c)$ is the refractive index increment of the sample, λ is the laser wavelength, and N_A is Avogadro's number (6.022×10^{23} mol^{-1}). The form factor is dependent on the shape of the scattering material and can be described for a sphere when $q \cdot (r_i - r_j) \ll 1$ as

$$P(q) = 1 - \frac{1}{3} q^2 R_G^2 \tag{13}$$

where R_G is the radius of gyration of the scattering particle. For very small particles, where $q^2 R_G^2 \ll 1$, the intra-molecular scattering is negligible, and $P(q)$ is assumed to be 1. The structure factor can be described by the Zernike-Prins function:

$$S(q,r) = 1 - 4\pi\rho_2 \int_0^\zeta r^2 \left(1 - \tilde{g}(r)\right) \left(\frac{\sin qr}{qr}\right) dr \tag{14}$$

where ρ_2 is the number density of dissolved particles and $g(r)$ is the pair correlation function. This function can be simplified and expressed as

$$S(r) = 1 - 2A_2\rho_2 \tag{15}$$

where A_2 is the second virial coefficient. When substituting ρ_2 with cN_A/M, the final equation

developed by Zimm takes the form:

$$\frac{Kc_p}{R_\theta} = \frac{1}{M}\left(1 + \frac{1}{3}q^2R_g^2\right) + 2A_2c \tag{16}$$

where A_2 is the second virial coefficient, which describes the pairwise interactions between scattering particles in solution [14,16].

A_2 can be calculated by constructing a Zimm plot and extrapolating the curve to $q = 0$ and to $c = 0$; however, this requires data acquired at several concentrations, and the position of total scattering intensity in the denominator can lead to error explosions at large intensities. Instead, the inverse of the Zimm equation can be used to determine A_2:

$$\left[\frac{Kc_p}{R_\theta}\right]^{-1} = \frac{1}{M}\left(1 + \frac{1}{3}q^2R_g^2\right) + 2A_2c \tag{17}$$

2.1.3 Dynamic Light Scattering

Dynamic Light Scattering (DLS) is a tool that can be used to determine the number of components present in a solution (the sample of interest and aggregates) and the size and percentage of the scattering they contribute to the total intensity. Fluctuations in intensity result in an intensity auto-correlation function, $g_2(t)$, which can be related to the field auto-correlation function, $g_1(t)$, via the Siegert relation, as shown in the following equation:

$$g_2(t) = \frac{\langle I(q,t) * I(q,0)\rangle}{\langle I(q,0)\rangle^2} = 1 + \beta|g_1(t)|^2 \tag{18}$$

The field correlation curve can be fit using the Kohlrausch-Williams-Watts (KWW) stretched exponential function:

$$g_1(t) = P_0 + P_1 * e^{-\left[\frac{t}{\tau_1}\right]^{\beta_1}} + P_3 * e^{-\left[\frac{t}{\tau_2}\right]^{\beta_2}} \tag{19}$$

where P_0 is the baseline, P_1 is amplitude of the fast process, τ_1 is the relaxation time of the fast

process, β_1 is the fast process stretching exponent, P_3 is the amplitude of the slow process, τ_2 is the relaxation time of the slow process, and β_2 is the slow process stretching exponent. A double exponential fit is necessary to capture both the fast process representing the particle and the slow process representing aggregates in the system. If the translational diffusion coefficient, $D = \Gamma/q^2$ where Γ is the relaxation rate equal to $1/\tau$, is experimentally found to be independent of concentration, then $D = D_0$, the self-diffusion coefficient. The self-diffusion coefficient, D_0, can be used to determine R_H using the Stokes-Einstein equation:

$$R_H = \frac{k_B T}{6\pi\eta_s D_0} \tag{20}$$

where R_H is the hydrodynamic radius, k_B is the Boltzmann constant (1.38×10^{-23} $m^2\,kg\,s^{-2}\,K^{-1}$), T is temperature, and η_s is the solvent viscosity.

2.2 Solutions of Polymer-Conjugated Proteins

2.2.1 Solution Behavior of Polymer-Conjugated Proteins

Since 1990, polymer modification of proteins has been used to improve stability, solubility, and immuno-retention of protein-based drugs [17]. Poly(ethylene glycol) (PEG) is most commonly used to conjugate proteins for protein-based therapeutics, since it is water soluble and non-toxic. However, applications of polymer-functionalized proteins extend beyond drug delivery and make use of a variety of polymer conjugates [18–30]. Understanding of the solution behavior of polymer-functionalized proteins is important for the development of technologies such as filtration membranes and breathable, self-regulatory military garments. The second virial coefficient, A_2, is a measure of pairwise interactions between particles in solution and an indicator of the solvent quality. Only two studies on A_2 of protein-polymer conjugates have been reported in the literature, to the author's knowledge. In the first study, Middelberg *et al*. used

Small Angle Neutron Scattering (SANS) to measure A_2 of a mono-PEGylated protein, human galectin 2. They found a positive value of A_2 (6.0 x 10^{-4} mol mL/g^2) which is indicative of a good solvent and repulsive forces acting between the PEGylated proteins [17]. In the second study, Mattiasson *et al.* used Photon Correlation Spectroscopy (PCS) to evaluate the dependence of antibody-poly(methacrylic acid) and antibody-poly(acrylic acid) conjugate solution behavior on pH. Although A_2 was reported for a neat polymer solution, it was not reported for the protein-polymer conjugates [31].

No systematic study, to the author's knowledge, has been conducted to determine A_2 for solutions of protein-polymer conjugates with varied graft length (molecular weight) and grafting density to determine the effect of graft architecture on solution properties of the conjugates, the understanding of which is essential to the optimization of protein-polymer conjugates for various applications.

The work presented in this dissertation document is focused on the solution behavior of a model protein-polymer conjugate, Bovine Serum Albumin-poly(ethylene glycol) (BSA-PEG). Previous solution studies have been performed on each individual component and reported in literature. Parameters of interest have included solution pH, buffer, and molarity [32]. In addition, measurements of BSA in solutions of PEG have been published [33]. The second virial coefficient, A_2, for BSA has been measured by Choi and Park using a colloid membrane osmometer on solutions of NaCl, KCl, and LiCl with molarities of 0.01M to 3M and was found to sensitively depend on both parameters. The measured values ranged from 0.26 to 2.29 x 10^{-4} mL mol/g^2 for BSA in these solutions [32]. J. Prausnitz *et al.* evaluated solutions of BSA in ammonium sulfate at concentrations of 0 to 25 g/L and molarity of 1 and 3 over a range of pH values (4 to 8) and found that the second virial coefficient was equal to 0.03 - 0.94 x 10^{-4} mL

mol/g^2 and increased with ionic strength and pH [34]. Vilker *et al*. found the second virial coefficient to be positive for all samples in 0.15 M NaCl solutions with pH ranging from 4.5 to 7.35 [35]. The second virial coefficient of BSA in 0.05 M potassium phosphate, pH = 6.2 buffer solution has been reported to be weakly negative (A_2 = -2 × 10^{-4} mL mol/g^2) by George and Wilson [36]. A_2 for PEG changes with molecular weight but is typically on the order of 1 x 10^{-3} mL mol/g^2 [36–39]. This work intends to fill a void in literature by evaluating the role of graft architecture on A_2 of a model protein-polymer system (BSA-PEG).

2.2.2 Compositional Heterogeneity of Polymer-Conjugated Proteins

PEGylation of proteins can be performed via several methods; however, first generation PEG coupling chemistry, which takes advantage of the ε-aminofunctionalities of lysine to couple activated PEG is still commonly used [40–46]. This PEGylation process inherently leads to heterogeneity in the resulting protein-polymer conjugates, which is often overlooked in literature. The resulting conjugate has a distribution of polymer grafts attached to the protein, which can be resolved using techniques such as High-Performance Liquid Chromatography (HPLC) and Matrix Assisted Laser Desorption/Ionization-Time of Flight (MALDI-TOF), as shown in Figure 2-1 [47].

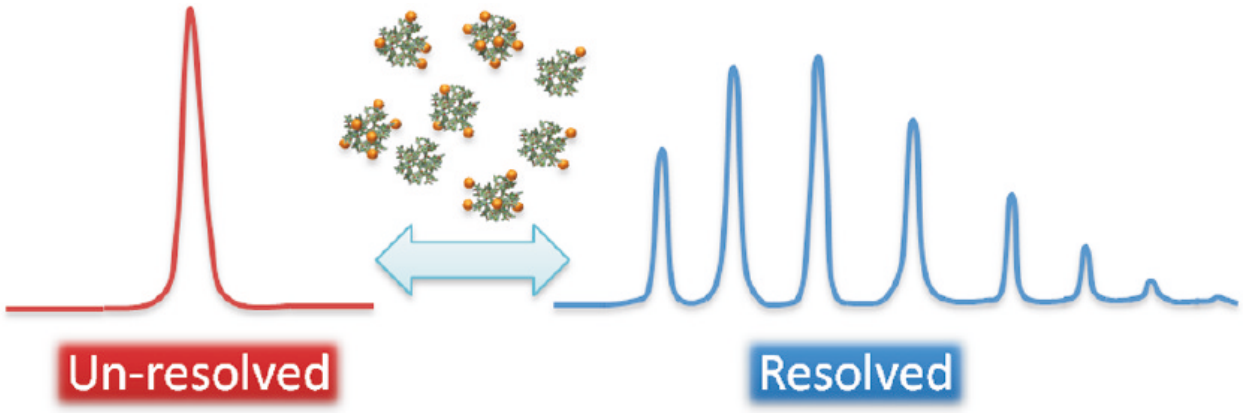

Figure 2-1. Schematic of the heterogeneity present in PEGylated proteins and the resulting spectra (HPLC or MALDI-TOF) that can be used to determine graft characteristics [47].

Banaszak Holl *et al.* and Hakem *et al.* have reported heterogeneity in ligand coupling characterized by HPLC and MALDI-TOF, respectively. While Banaszak Holl has proposed a Poisson distribution for the fitting of data, Hakem has developed a binomial distribution for protein-polymer conjugates with few grafts, shown in Equation 21 [13,47–49].

$$P(g) = \frac{g_{max}!\,\varepsilon^{g}(1-\varepsilon)^{(g_{max}-g)}}{g!\,(g_{max}-g)!} \tag{21}$$

From the peak amplitudes, the distribution of ligands, and hence the compositional

heterogeneity, can be determined by fitting with the theoretical predicted distribution P(g), where n_{max} is the total number of reactive sites per particle (for BSA, g_{max} = 59), g is the number of ligands bound to the particle surface at any given instant, and ε is the reaction efficiency, equal to the ratio of the average number of reacted sites to the total number of reactive sites ($<g>/g_{max}$). By applying this ligand distribution function, the average number of grafts, $<g>$, can be determined from $< g >= \int gP(g)dg$. A schematic of protein-polymer conjugates of equal grafting efficiency with uniform and non-uniform grafting is shown in Figure 2-2.

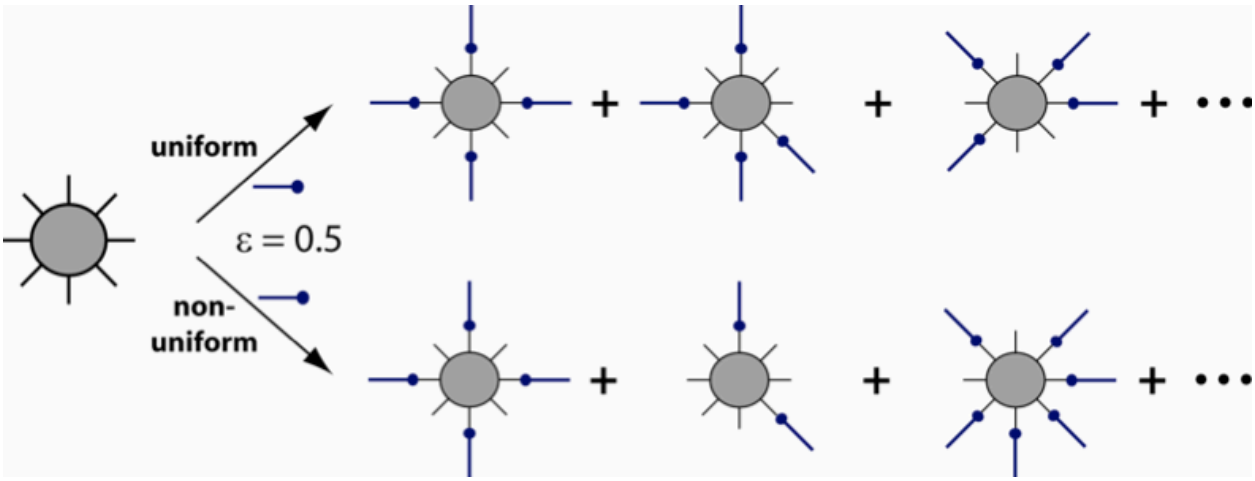

Figure 2-2. Schematic of the heterogeneity that occurs with PEGylation of proteins. In the top row, each particle has the same number of ligands. In the bottom row, the number of ligands fluctuates among distinct particles but still results in the same efficiency [49].

These probability distributions can be used to determine important graft characteristics, such as grafting efficiency, the average number of grafts, and the molecular weight of the conjugate. In this study, the approach used by Hakem *et al.* is successfully applied to a model protein-polymer system (BSA-PEG) to characterize and identify the differences in graft architecture between samples.

2.3 Block Copolymers

2.3.1 Structure Formation in Pristine Block Copolymer Systems

Block copolymers consist of covalently bonded polymers that can form unique morphologies depending upon the Flory-Huggins interaction parameter, the degree of polymerization, and the volume fraction of each component [50]. For diblock copolymers, four distinct equilibrium structures can be formed including lamellae, gyroids, cylinders, and spheres, as shown in Figure 2-3 [51]. A positive χ parameter indicates that two non-polar homopolymers would prefer to de-mix. However, in the case of a block copolymer, the two homopolymer components are covalently bonded together, preventing macrophase separation. Instead, the block copolymer microphase separates with an enthalpic gain that is balanced by an entropic penalty from ordering and interfacial energy.

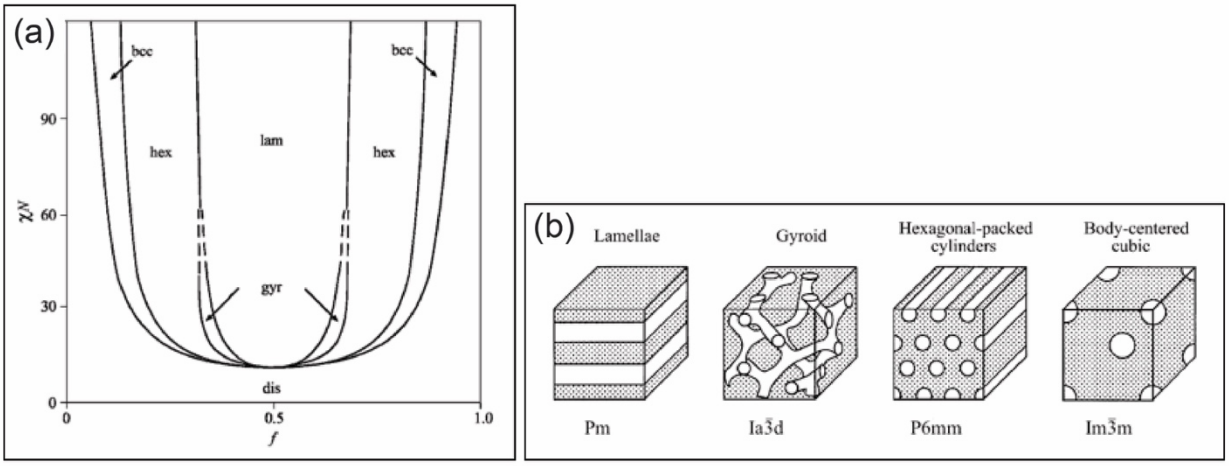

Figure 2-3. (a) Phase diagram of a diblock copolymer. The vertical axis is a weighted interaction parameter, and the horizontal axis is the volume fraction of polymer A. (b) Diblock copolymer morphologies, from left to right: L-lamellae, G-gyroids, C-cylinders, and S-spheres [51].

Block copolymers have found use in lithography and thermoplastic elastomer applications [52–54]. In addition, their ordered structures can facilitate the creation of nanostructured composite

materials that improve the functionality (mechanical, thermal, or optical) of the polymer film without sacrificing the formability of the polymer matrix.

2.3.2 Block Copolymer/Nanoparticle Blends

2.3.2.1 Conditions for Particle Solubility

Several parameters contribute to whether or not a particle is soluble in a matrix. Leibler *et al.* established a self consistent field (SCF) approximation to examine the entropic interactions that occur in an enthalpically neutral system of a flat polymer brush (analogous to our BSA-PEG) and a polymer melt (analogous to our BCP matrix) [55,56]. They found that positive surface tension of the brush leads to partial wetting of the melt and possible phase separation and aggregation. The system parameters most relevant to this behavior are the degree of polymerization of the graft (N), the degree of polymerization of the melt (P), and the brush graft density (σ). At low grafting density, the brush takes on a mushroom configuration consisting of isolated random coils, with a height equal to the Flory radius ($N^{3/5} P^{-1/5}$). As the grafting density increases, the grafts begin to stretch, causing a decrease in configurational entropy. To offset this penalty, the melt chains reconfigure to penetrate and swell the brush, increasing their entropy. The height of the brush in this case is equal to $N \sigma^{1/3} P^{-1/3}$. As the grafting density increases further, space for melt chain penetration becomes more limited, resulting in a dry brush (no penetration of the elongated chains) with a height equal to $N \sigma$.

2.3.2.2 Structure Formation in Block Copolymer/Nanoparticle Blends

Dispersion of nanoparticle fillers can be controlled via polymer functionalization of the filler surface to make it compatible with one particular domain of the block copolymer. Control in the

spatial and orientational distribution of nanoparticle fillers in the block copolymer matrix is important in the development of new functional composite materials.

A large body of literature details the work done by several research groups on block copolymer/nanoparticle blend systems. In 2001, Balasz *et al.* combined density functional theoretical and self-consistent field theoretical computer simulations to examine nanoparticle dispersion in a lamellar block copolymer system. It was found that for small particles (D/L = 0.2), segregation at the intermaterial dividing surface (IMDS) occurred, while for large particles (D/L = 0.3), center segregation in the compatible domain occurred (D: particle diameter, L: lamellar spacing) [57]. This difference in dispersion behavior of nanoparticles depending on particle size can be explained by the balance between the conformational entropy penalty of the block copolymer's accommodation of particles in a domain and the translational entropy gain of the nanoparticles freely dispersing. In addition, the authors indicated that the geometry rather than the chemical identity of the filler is the determining characteristic of structure formation in block copolymer/filler systems.

In the early 2000s, Bockstaller and Thomas performed experiments that supported these computational findings. A blend of PS-*b*-PEP with ~3 nm diameter $AuSC_{12}H_{25}$ nanoparticles was compared with a blend of PS-*b*-PEP with ~22 nm diameter SiO_2-(C_3H_9) nanoparticles. The small gold nanoparticles dispersed along the IMDS, while the large silica nanoparticles segregated to the middle of the PEP domain (compatible with the aliphatic ligands on the particles), as shown in Figure 2-4. With equal enthalpic contributions in both cases, the difference in particle dispersion can be attributed to the entropic contributions described previously [58].

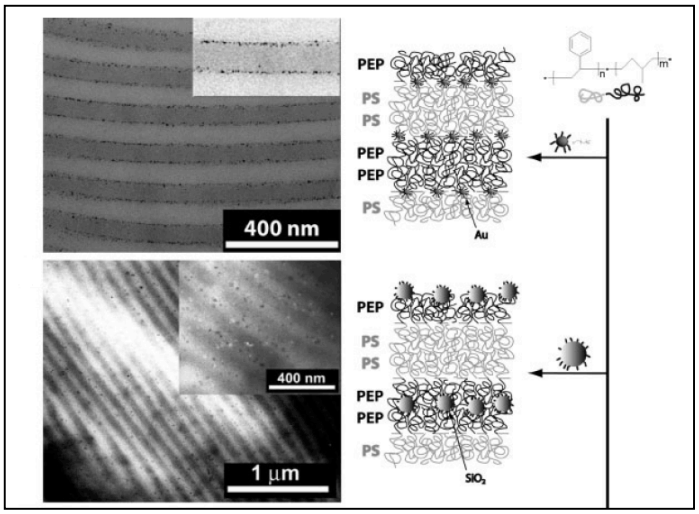

Figure 2-4. (a) TEM micrograph and schematic of PS-*b*-PEP/$AuSC_{12}H_{25}$ depicting the nano-fillers distributed at the boundary between the PEP and PS. (b) TEM micrograph and schematic of PS-*b*-PEP/SiO_2-(C_3H_9) depicting the nano-fillers distributed in the middle of the PEP domain [58].

This segregation behavior has also been observed for related BCP/homopolymer blends by Hashimoto *et al.* in a PS-*b*-PI/hPS system. For low molecular weight hPS, dispersion occurred throughout the PS domain and near the IMDS. Higher molecular weight hPS was limited to center segregation in the PS domain, while extremely high molecular weight hPS experienced aggregation and macrophase separation [59].

In the same year, Winey *et al.* reported a systematic study of PS-*b*-PI/hPS with varied hPS molecular weight and concentration. At a fixed molecular weight, as concentration increased, the difference between dispersion in low and high molecular weight hPS was identified by SAXS. High molecular weight hPS segregated to the center of the PS domain, increasing the lamellar spacing of the PS domain without affecting the PI domain. Low molecular weight hPS dispersed uniformly in the PS domain, causing the PS domain spacing to increase and the PI domain spacing to decrease [60].

The effect of enthalpic interactions has been studied by Kramer *et al*., who created blends of PS-*b*-P2VP with gold nanoparticles (mutual affinity to both polymer domains) bound to PS ligands.

Upon variation of grafting density, the particles with a high grafting density of PS segregated to the center of the PS domain (favorable enthalpic interactions), while the particles with a low grafting density of PS experienced only partial shielding and dispersed along the IMDS (neutral enthalpic interactions) [61].

Finally, Listak *et al.* evaluated the effect of particle size and polymer connectivity on the segregation of particle fillers and observed both center segregated and uniform particle distributions for large and small particle fillers, respectively. The authors also observed that both morphological states can be distinguished by the effect of particle addition on the characteristic domain spacing of the copolymer. In particular, they predicted that for center segregation, the lamellar spacing depends on particle loading as $L=L_o*(1+\phi_P)$ whereas for uniform distribution, $L=L_o*(1+(1/3)\ \phi_P)$ is expected [62].

More recent studies have been focused on the effect of filler concentration on order-order and order-disorder transitions of the polymer host, the effect of block copolymer architecture on the dispersion morphology of sequestered particle fillers, as well as the effect of particle additives on the stabilization of defect structures in BCP/NP blends [63–66].

2.3.2.3 Block Copolymer/Protein Composites

Although extensive research has been done on block copolymer/polymer-functionalized nanoparticle blends, little work has been performed on blends of block copolymer/polymer-functionalized proteins formed via co-assembly. Co-assembly is one of three major routes used to incorporate proteins into block copolymers, the other two being adsorption of proteins to the surface of the BCP and substitution of the protein as one block in the BCP [18,67].

Preferential adsorption of BSA to the PS domain in ordered PS-*b*-PI was demonstrated by Liu and coworkers [68]. Olsen *et al.* have investigated the incorporation of proteins into matrices by synthesizing a protein-polymer BCP, mCherry-*b*-PNIPAM [69–71]. Upon solvent annealing the sample, they observe lamellar and cylindrical structures using TEM and SAXS. They also maintained 70-95% of the protein function after casting.

There are three reports of the co-assembly of protein-polymer conjugates with a BCP, the focus of this study, to the author's knowledge. Xu *et al.* demonstrated that biologically active proteins and their cofactors could be incorporated together in thin films of cylindrical PS-*b*-PEO while preserving the protein's structure and activity [72]. Russell *et al.* demonstrated in 2005 that ferritin-PEG conjugates could be incorporated into lamellar diblock copolymer thin films via the co-assembly process (P2VP-*b*-PEO) [73]. They observed a suppression of PEO crystallization with the addition of the ferritin-PEG using optical microscopy and AFM. In 2010, Russell *et al.* cast thin films of PS-*b*-PEO with neat ferritin and ferritin-polyPEGMA that maintained their cylindrical structure but experienced an increase in spacing [74]. Beyond the work cited here, no systematic study on dispersion of polymer-functionalized proteins in a BCP has been reported in literature, exhibiting a lack of understanding of structure formation processes in BCP/'protein particle' systems and specifically, how structural parameters such as number and molecular weight affect the solubility limit, order-order transition, and dispersion characteristics of polymer-conjugated protein in BCP matrices.

2.4 Approach

Polymer-functionalized proteins are emerging as intriguing materials for a variety of composite materials with applications ranging from pharmaceuticals to stimuli-responsive membranes. In

order to realize these protein-based technologies, a fundamental understanding of the parameters governing solubility as well as dispersion in polymer matrices must be developed. To determine the role of graft architecture on solubility of polymer-functionalized proteins, a model system of Bovine Serum Albumin (BSA) conjugated with poly(ethylene glycol) (PEG) was synthesized with varied graft length (molecular weight) and grafting density. The second virial coefficient, A_2, was evaluated as a measure of solution properties. To determine the role of graft architecture on dispersion of polymer-functionalized proteins, blends of poly(styrene-*b*-methyl methacrylate) (PS-*b*-PMMA) and BSA-PEG were co-assembled and studied using electron microscopy. Both studies allow for understanding of the role of graft architecture on behavior in solution and in polymer media and can ultimately lead to the optimization of protein-polymer conjugates for various applications. One such application was demonstrated with the development of a stimuli-responsive membrane consisting of a porous triblock terpolymer decorated with enzymes. The membrane underwent permeability, mechanical, and stability testing to demonstrate its ability to effectively neutralize a nerve agent simulant and prompt a decrease in permeability. Additional characterization in the form of electron microscopy and ellipsometry provided insight into the dispersion of the enzymes with respect to the triblock terpolymer.

Chapter 3: Experimental

3.1 Sample Preparation

3.1.1 Materials: Enzyme Actuated Polymer Membranes

All compounds and solvents were used as received unless otherwise noted. Phosphotriesterase (PTE) was obtained from Novozymes (Davis, CA) and exchanged into 50 mM potassium phosphate, 100 uM cobalt chloride, pH 8.0 for storage at 4 °C until use. Enzyme variants PTE(RN-YT) and PTE(C23) were prepared in-house according to previously published procedures [75,76]. pH-Sensitive dye 1 was custom synthesized and purchased from American Dye Source, Inc. (Quebec, Canada). Ethyl paraoxon (>98%) was purchased from Chem Service, Inc., and Diisopropylfluorophosphate (>97%) was acquired from Sigma-Aldrich.

3.1.2 Polymer and Membrane Preparation

The detailed preparation of the triblock terpolymer ISV, and mesoporous asymmetric membranes derived from ISV, has been described elsewhere [5]. Here five ISV triblock terpolymers were synthesized by anionic polymerization. Total number average molar mass, M_n, weight fraction, f, and polydispersity index, PDI, for these terpolymers as experimentally determined by gel permeation chromatography (GPC) and proton nuclear magnetic resonance (^{1}H NMR).

ISV membranes were fabricated by employing a combination of self-assembly and non-solvent induced phase separation, now referred to as SNIPS [77]. An ISV polymer casting solution was prepared by dissolving ISV polymer into a co-solvent mixture comprised of a 7:3 ratio (by weight) of 1,4-Dioxane (DOX) and tetrahydrofuran (THF). The solution was pipetted onto a glass substrate for neat, unsupported membranes. Supported membranes were cast directly onto

porous nylon substrates, purchased from Sterlitech Inc., taped to glass substrates. The polymer solution was cast by a doctor blade with a gate height of 220 μm and allowed to evaporate for a specified amount of time before the films were immersed into a deionized water bath. Unless mentioned otherwise, membranes were cast from a 16% (ISV43), 12% (ISV99 and ISV118) or 11% (ISV117 and ISV119) (by weight) polymer solution. Membranes were cast on top of a 0.2 μm (ISV117), 0.1 μm (ISV43, ISV99, ISV119) or 0.04 μm (ISV118) nylon support. Membranes cast from ISV117 and ISV118 exhibited an open "finger-like" substructure while membranes cast from ISV43, ISV99 and ISV119 showed a dense "sponge-like" substructure [6,78]. It is assumed here that membranes cast from solutions that vary slightly in polymer concentration have similar properties and performance values.

3.1.3 Materials: Protein-Polymer Conjugates in Solution and BCP Templates

Bovine Serum Albumin (BSA, $M_w \approx 67$kDa) was purchased from Sigma Aldrich, and methoxy-PEG-succinimidyl carboxymethyl ester (mPEG-NHS) and methoxy-PEG (mPEG); M_w = 2kDa, 3kDa, 5kDa, 10kDa, and 30kDa were purchased from JenKem Technology USA. The block copolymers, poly(styrene)-*b*-poly(methyl methacrylate) (PS-*b*-PMMA, $M_{w\,PS}$ = 42.2k g/mol, $M_{w\,PMMA}$ = 42.2k g/mol, PDI = 1.06; PS-*b*-PMMA, $M_{w\,PS}$ = 21k g/mol, $M_{w\,PMMA}$ = 21k g/mol, PDI = 1.07; PS-*b*-PMMA, $M_{w\,PS}$ = 203.5k g/mol, $M_{w\,PMMA}$ = 203.5k g/mol, PDI=1.10), were purchased from PolymerSource (42k) and PSS (84k and 407k). Phosphate buffered saline (PBS) was purchased from Sigma Aldrich (pH 7.4, 0.0027 M KCl, 0.138 M NaCl). Pyridine, acetonitrile, and trifluoroacetic acid were purchased from Fisher Scientific. All materials were used as received.

3.1.4 Synthesis

Initially, PEGylation was performed at FLIR Systems, Inc. using a standard protocol that they have successfully applied to several protein-polymer conjugate systems. Molar concentration ratios of mPEG-NHS:lysines were 10:1, 15:1, and 20:1, corresponding to a large excess of polymer to protein in solution. mPEG-NHS of each molecular weight (2000, 5000, 10,000, and 20,000 g/mol) was dissolved in DMSO at a concentration of 100 mg/mL. BSA was dissolved in a 50 mM borate buffer solution at a concentration of 0.5 mg/mL. Both solutions stirred separately until dissolved (approximately 1 hr). The solutions were combined and allowed to react for 24 hours. The resulting solution was concentrated and underwent a solvent exchange replacing the solution buffer with water 10x while refrigerated at 4°C. UV-Vis was performed on the sample to ensure that the protein was still in solution and the free mPEG-NHS had been filtered out. SDS-PAGE was used to confirm PEGylation by revealing an increase in the molecular weight of the samples with molar concentration ratio and with degree of polymerization of the grafting PEG. There was indication of successful grafting for each sample except for those grafted with mPEG-NHS 20,000 g/mol. Ultimately these samples were not used, since quality MALDI spectra could not be obtained, and since the yield was very low for the amount of mPEG-NHS required in the reaction.

The protein-polymer conjugates used in this study were synthesized using a non-specific coupling reaction between mPEG-NHS and the lysine residues of BSA in a phosphate buffered saline solution. For each molecular weight, synthesis was performed for different molar concentration ratios of mPEG-NHS:lysine residues to vary the number of PEG grafts on BSA. Literature has indicated that a ratio of 0.57:1 is ideal to optimize the average number of grafts, which is consistent with the findings reported here [79]. The solutions were stirred for 1 hour

before 3 μL of 0.1 M HCl solution was added to end the reaction. The unreacted mPEG-NHS was filtered by dialysis using a 50kDa membrane filter for 72 hours in DI water. The samples were lyophilized for 24 hours using a Labconco Cascade FreeZone Plus 2.5 Freeze-Dry System operated at -84 °C and 0.035 mBar.

3.1.5 Block Copolymer/Protein-Polymer Blend Preparation

A neat film of PS-*b*-PMMA was solvent cast from an 8.5 wt. % polymer solution in pyridine over two weeks. Slow solvent evaporation in a solvent environment combined with thermal annealing allows for an equilibrium structure to be obtained. Three samples were made from the resulting 1 mm thick film: 'as cast' and '3 days thermally annealed' with the thermal annealing taking place in a vacuum oven set to 150°C, above the glass transition temperatures of the constituent blocks. Blends were made by adding 1, 5, and 10 wt.% BSA-PEG samples to the block copolymer solutions in pyridine followed by solvent casting, described for the neat block copolymer films.

3.2 Characterization Techniques

3.2.1 Moisture Vapor Transport Rate (MVTR)

An evaporative dish method, based on the British Standard BS 7209, was used to determine the MVTR in membrane samples [80]. The Turl dish assembly consists of a dish, triangular support, and cover ring. The test specimen is comprised of two circular membrane samples, with a total area of 402 mm^2, anchored to a circular transparency film, purchased from C-Line Products, Inc. (No. 60837), using epoxy. The test specimen was sealed over the mouth of the dish containing deionized water and the triangular support to maintain a ~10 mm air gap. The cover ring was

placed above the test specimen and adhesive tape was applied around the circumference of the competed assembly. The assembly was positioned into a turntable and the experiment was conducted in a controlled atmosphere of 20 °C and 65% relative humidity. The assemblies were weighed on a balance with a resolution of 0.01g. Each assembly was weighed daily up to five days in order to assure full equilibration. Data for calculation of MVTR values were taken on day five.

The MVTR (g m^{-2} day^{-1}) was calculated as:

$$\text{MVTR} = 24M(At)^{-1} \tag{22}$$

where M is the loss in mass of water in grams, t is the time period in hours, and A is the area of the membrane sample in m^2.

In addition to the three nylon-supported ISV membranes (ISV43, ISV99, and ISV199), dishes were evaluated in the open and closed states for reference. Values obtained from these measurements were used as benchmarks in addition to literature values reported for relevant commercially available material (i.e. PTFE and PU) [81].

3.2.2 Intrinsic Water Vapor Resistance

Intrinsic water vapor resistance was calculated as:

$$R_{et} = R_f(RT)\left(M_W \Delta H_{vap}\right)^{-1} \tag{23}$$

where R_f is the intrinsic mass transfer resistance of the sample, R is the universal gas constant, T is temperature, M_w is molar mass of water, and ΔH_{vap} is the enthalpy of vaporization of water.

3.2.3 Tensile and Flex Deformation

Tensile testing of the membranes was performed on an Instron (model 4442) equipped with a 1 kN load cell with loading strain rates of 1, 10, and 100 mm min^{-1}. The samples were 13 mm x 20 mm with a thickness of 0.11 mm. Stress-strain curves were constructed, and the Young's Modulus was determined by calculating the slope within the proportionality limit of the curve. The toughness was calculated by integrating the stress-strain curve over the entire deformation range. Samples were fixated and repeatedly flexed (three sets of 10 flexes) to a curvature of 3 cm^{-1} at a rate of 0.5 Hz.

3.2.4 ISV Enzyme / Dye Adsorption

Supported ISV membranes were incubated in solutions of PTE enzyme (1-20 mg mL^{-1}, 10 mM CAPSO, pH 9.4, 500 μL per 100 mm^2 membrane surface area) for 16 hours at 4 °C on an orbital shaker at low speed. For samples containing dye 1, 100 μL of a 10 mg mL^{-1} stock solution in water was added to the protein solution for every 100 mm^2 membrane surface area. Post-immobilization, samples were washed (3x) with 10 mM CAPSO, pH 9.4 buffer for 30 minutes at 4 °C on an orbital shaker at low speed prior to testing.

3.2.5 Colorimetric and Fluorescent Visualization

Visual images of colorimetric results were recorded using a Cannon PowerShot A4000 IS HD camera. Supported ISV117 membranes functionalized with enzyme (PTE(C23) or PTE(YT)) and dye 1 were dried under ambient conditions for 5 minutes prior to challenge with simulant and control solutions (1 uL). Colorimetric response was observed and recorded within 1 minute of liquid challenge.

Vapor-induced fluorescence emission images of supported ISV117 membranes functionalized with PTE(C23) and dye 1 were captured on an Oculus Photonics imager equipped with a ThorLabs 800 nm long pass filter operating in monochrome video mode. Fluorescent samples were excited using a HHE 735 nm LED on high power. Membranes were dried under ambient conditions for 5 minutes and suspended from the top of a closed vessel prior to simulant challenge (neat DFP (5 uL) deposited in the bottom of a 30 mL test vessel). Continuous video was recorded over 10 minutes and still frames were extracted for relevant time points (time = 0 or 2.5 minutes).

3.2.6 Permeability Studies

Permeability measurements were performed by placing membranes into a stirred cell concentrator (Amicon 8010, Millipore Co.; EMD Millipore 5121) with 50 mM buffers (imidazole, acetate) at various pH. Pressure was applied using nitrogen and, while stirring, the liquid that passed through the membrane was collected in a beaker positioned on a balance. Mass data collected at specified time intervals (10 or 15 seconds) and used to determine permeability in liters per meter squared per hour per bar ($Lm^{-2}h^{-1}bar^{-1}$). Measurement of enzyme-mediated permeability change was completed using PTE(RN-YT)-bound membranes. For these samples, an open pore state permeability was established with 1 mM imidazole, pH 6.5 (ISV119, L_p = 50-75 $Lm^{-2}hr^{-1}bar^{-1}$). The average permeability values of the protein-functionalized membranes were slightly lower than that measured for native membrane samples due to enzyme binding. Once the residual buffer volume above the membrane reached approximately 1 mL, paraoxon solution (40 mM in methanol, 70, 150, or 200 uL) was delivered through a septum in a modified stirred cell apparatus. Final material permeability was measured in the closed state for each

simulant challenge level (70 uL, L_p = 20 $Lm^{-2}hr^{-1}bar^{-1}$ and >150 uL, L_p = 1.2 $Lm^{-2}hr^{-1}bar^{-1}$). The percent permeability was normalized using the absolute difference between the open and closed state measured for each membrane over the time scale of the experiment.

3.2.7 Ellipsometry Studies

Ellipsometry measurements were conducted using a Beaglehole Instruments Picometer phase-modulated ellipsometer equipped with a helium-neon laser (λ=632.8 nm). The angle of incidence was varied from 70-80°, and analysis was completed using TF Companion software (Version 3.0, Semicon Software, Inc.) and a four layer, homogeneous film model (semi-infinite silicon + silicon dioxide + polymer + adsorbed enzyme + semi-infinite air). Thin films of PI, PS, P4VP, and ISV with thicknesses between 10 – 20 nm were spin cast from 0.1 wt. % solutions in toluene (PI, PS, and ISV) and a 1:1 mixture of acetone and ethanol (P4VP) onto silicon wafers. The polymer-coated wafers were incubated in a solution of PTE enzyme (9.7 mg mL^{-1}, 10 mM CAPSO, pH 9.4) for 16 hours at 4°C on an orbital shaker at low speed. The layer thickness was successively determined for the silicon dioxide layer (2-3.5 nm), the polymer layer (10-20 nm), and the adsorbed enzyme. Literature values of refractive indices for PI (1.51), PS (1.59), P4VP (1.581), ISV (1.5707), and dry enzyme (1.53) were used for the analysis [82–84].

3.2.8 PTE Enzyme Activity and Adsorption

Direct phosphotriesterase hydrolysis assays were performed on a Molecular Devices SpectraMax M2e spectrophotometer in 96 well plates for solution-phase enzyme samples (100 μL reaction volume, 0.35 mm path length, 5 min kinetic duration) and on a Beckman Coulter DU530 UV/VIS spectrophotometer, transferring aliquots of assay solution samples to a cuvette for solid-

phase enzyme samples (1 mL volume, 1 cm path length, 10 min kinetic duration). All assays were completed at 25 °C against ethyl paraoxon and the rates were measured by monitoring the release of p-nitrophenol (ε_{405} = 17100 $M^{-1}cm^{-1}$). Substrate stock solutions were prepared by the dissolution of diethyl paraoxon in dry methanol (152 mM) followed by dilution of the methanol stock in deionized water (15.2 mM). For the enzymatic reaction, aliquots of the 15.2 mM paraoxon stock were added to a mixture of enzyme in reaction buffer (50 mM CAPSO, 50 μM $CoCl_2$, pH 9.0) to give a final concentration of 1.52 mM. A dilution series of enzyme concentrations was used for solution-phase samples (final enzyme concentrations range from 1 ng-10 μg mL^{-1}) to achieve a linear rate. For solid-phase samples, a section of membrane was submerged in an adequate volume as to maintain a linear rate over the course of the kinetic assay (typical conditions: 3 mm diameter circle, 2 mg mL^{-1} enzyme incubation, 12 mL assay buffer). The initial enzymatic rates were corrected for the background rate of spontaneous paraoxon hydrolysis in the absence of enzyme. Specific activity values of the solution-phase samples were calculated using the following formula:

Specific Activity (umol min^{-1} mg^{-1}) = ΔmAU min^{-1} x (1 x 106) x DF x (1000 x 17100 x 0.35 x C)$^{-1}$, where $\Delta mAU\ min^{-1} = \Delta mAU\ min^{-1}\ test$ - $\Delta mAU\ min^{-1}\ blank$, *DF* is the dilution factor, *17,100* $M^{-1}\ cm^{-1}$ is the molar extinction coefficient of p-nitrophenol, *C* (in mg L^{-1}) is the protein concentration of enzyme stock solution and *0.35 cm* is the path length of light.

Quantitation of active enzyme loading of solid-phase samples was calculated using a calibration curve prepared from the rates of enzymatic paraoxon hydrolysis (linear regression of absorbance vs. time) for a series of solution-phase enzyme standards of known concentration and identical specific activity as that incubated with the membrane. The resulting equation was then compared

against the hydrolysis rates obtained for the solid-phase samples to calculate enzyme mass loading (ng) per unit area (mm^2).

Enzyme stability during dry storage on supported ISV119 membranes was assessed in the presence and absence of stabilizing excipient for a range of temperatures over a 30 day incubation period. Enzyme functionalized membranes were prepared as described in the *Materials: Enzyme Actuated Polymer Membranes* section. Upon completion of the final rinse, excipient stabilized membranes were subjected to an additional incubation in a 1% collagen hydrolysate solution (3 mm diameter ISV119, 500 uL solution, 30 min, 4 °C), after which both native and stabilized membranes were lyophilized to dryness and individually packaged under nitrogen in Mylar bags for storage. Samples were incubated at 4, 25, 40, or 60 °C for up to 30 days, with activity time points collected on days 0, 10, and 30. At each time point the enzyme activity was assessed by >4 replicates. Pretreatment of samples with excipient significantly helped to maintain enzyme activity of the dried samples as measured on day 0.

3.2.9 Matrix Assisted Laser Desorption/Ionization-Time of Flight (MALDI-TOF)

MALDI-TOF mass spectrometry was performed on an Applied Biosystems Voyager DE-STR mass spectrometer (mass range 1-400000 Da) equipped with positive and negative ion modes, linear and reflector modes, and a nitrogen laser operating at λ = 337 nm. The recommended sample concentration for proteins is 0.1 – 10 pmol/µL (0.1 – 10 x 10^{-6} M), so the lyophilized sample was dissolved in a solution of 70% DI water / 30% acetonitrile (ACN) at concentration of 3.33 mg/mL (50 pmol/µL) and shaken until it was dissolved [85]. Two stock solutions of matrices were mixed – ferulic acid dissolved at a concentration of 8.65 mg/mL in a solution of 70% DI

water / 30% ACN / 0.1% trifluoroacetic acid (TFA) and sinapinic acid dissolved at a concentration of 10 mg/mL in a solution of 70% DI water / 30% ACN / 0.1% trifluoroacetic acid (TFA). On a 100 well MALDI plate, 1 μL of the sample solution was deposited onto a well followed immediately by 1 μL of the matrix solution. This was done for all samples, resulting in two wells for each sample (one for each matrix). In addition, a solution was mixed containing both sample and matrix and deposited (1 μL) onto a third and fourth well for each sample.

3.2.10 Photon Correlation Spectroscopy

An ALV/LSE-5004 goniometer/correlator setup with a HeNe laser (λ = 633 nm) at 20 °C over the time range 10^{-7} to 10 s was used to measure the autocorrelation function $g_2(q,t)$

$$g_2(q,t) = \frac{\langle I(q,0)\, I(q,t)\rangle}{\langle |I(q,0)^2| \rangle} \tag{24}$$

of the light scattering intensity $I(q)$ at a scattering vector $q = 4\pi n\lambda^{-1}\sin(\theta/2)$ where n is the medium refractive index, λ is the vacuum wavelength of the incident light, and q is the scattering angle over the range 30° to 150°.

DLS/SLS data were collected using an ALV/LSE-5004 goniometer/correlator setup with a HeNe laser (λ = 633 nm) at 20 °C. The detection angle was varied from 30° to 150° in increments of 10° for SLS and 30° for DLS. BSA-PEG samples were dissolved in PBS at a concentration of 10 g/L and were filtered through 0.22 μm Millipore filters into round quartz cells (outer diameter of 1 cm). Measurements were performed with vertical (VV) polarization. The Siegert relation is used to compute the normalized light scattering intensity autocorrelation function $g_2(q,t)$

$$g_2(q,t) = 1 + f^* |\alpha g_1(q,t)|^2 \tag{25}$$

where f^* is an experimental instrument factor relating the scattering area to the coherence area via a standard, and α is the fraction of total scattered intensity stemming from fluctuations with correlation times longer than 10^{-7} s.

The normalized correlation function of the scattered electric field is described by $E(q,t)$

$$g_1(q,t) = \frac{\langle E^*(q,0)\, E(q,t)\rangle}{\langle |E(q,0)^2| \rangle} \quad (26)$$

and can be related to the experimental correlation function, $C(q,t) = \alpha g_1(q,t)$. In a first step, regular cumulant analysis (assuming mono-modal behavior) is performed to qualitatively establish dispersity of samples. In a second step, the Kohlrausch-Williams-Watts (KWW) function $g_1(t) = P_0 + P_1 * e^{-\left[\frac{t}{\tau_1}\right]^{\beta_1}} + P_3 * e^{-\left[\frac{t}{\tau_2}\right]^{\beta_2}}$, where P_0 is the baseline, P_1 is amplitude of the fast process, τ_1 is the relaxation time of the fast process, β_1 is the fast process stretching exponent, P_3 is the amplitude of the slow process, τ_2 is the relaxation time of the slow process, and β_2 is the slow process stretching exponent, is used to establish characteristic relaxation times. For uniform systems, such as low M_w mPEG-NHS, agreement is found between the two types of analysis. Using the diffusion coefficient, $D = \Gamma/q^2$, where Γ is the relaxation rate equal to $1/\tau$, the hydrodynamic radius can be determined using the Stokes-Einstein equation, $R_h = \frac{k_B T}{6\pi\eta_s D_0}$, where R_H is the hydrodynamic radius, k_B is the Boltzmann constant (1.38×10^{-23} m^2 kg s^{-2} K^{-1}), T is temperature, and η_s is the solvent viscosity.

Doubly distilled and filtered toluene was used as a standard to evaluate absolute scattering intensities. The absolute scattered intensities are given by the Rayleigh ratio: $R(q) = \left(I_{sample} - I_{solvent}\right) * \frac{R_{toluene}}{I_{toluene}} * \left[\frac{n_{solvent}}{n_{toluene}}\right]^2$ where n is the refractive index. The reduced Rayleigh ratio, $R(q)/(Kc)$ includes the concentration, c, and an optical constant, $K =$

$4\pi^2 n^2 \left(\frac{\delta n}{\delta c}\right)^2 (\lambda^4 N_A)^{-1}$, where n is the refractive index of the solvent, $(\delta n/\delta c)$ is the refractive index increment of the sample, λ is the laser wavelength, and N_A is Avogadro's number (6.022 x 10^{23} mol^{-1}).

3.2.11 Electron Microscopy (TEM and SEM)

Solutions of 10 g/L of BSA-PEG in pyridine or in DI water were drop cast onto carbon-coated grids for TEM imaging. To preserve the microstructure of PS-*b*-PMMA, a 1 mm thick film was microsectioned at −120 °C using a LEICA EM FCS cryoultramicrotome. To enhance contrast, 70 nm thick microsections were stained using ruthenium tetroxide (obtained from EM Sciences) for 5-10 minutes, which preferentially stains the PS domain [86]. ISV membranes were stained for 2-30s with Phosphotungstic Acid (PTA) to increase the contrast between the P4VP / enzyme components and the membrane. TEM was performed using a JEOL 2000 EX electron microscope operated at 200 kV. Imaging was done by amplitude and phase contrast, and images were acquired using a Gatan Orius SC600 high-resolution camera.

Membrane surface morphology and cross section were characterized using a Philips XL30 Scanning Electron Microscope after coating sample surfaces with 5 nm of platinum at Carnegie Mellon University. Field Emission SEM (Tescan Mira3 FESEM) was performed at Cornell University after coating sample surfaces with gold palladium at a current of 40 mA for 6 seconds (Denton Vacuum Desk II). Average pore sizes from SEM micrographs were analyzed with Mathematica and ImageJ.

3.2.12 Optical Interferometry

The refractive indices of BSA, mPEG-NHS, and BSA-PEG conjugates in PBS were measured at concentrations of 1, 2.5, 5, 7.5, and 10 g/L using a Reichert AR7 Series automatic refractometer at 20°C after calibration with DI water. The recorded values were plotted against concentration, and the slope of the line was taken as the refractive index increment of the sample ($\delta n/\delta c$): BSA (0.1684 mL/g), mPEG-NHS2k (0.1246 mL/g), mPEG-NHS3k (0.1261 mL/g), mPEG-NHS5k (0.1216 mL/g), mPEG-NHS10k (0.1216 mL/g), mPEG-NHS30k (0.1293 mL/g), BSA-PEG2k (0.1647 mL/g), BSA-PEG3k (0.1799 mL/g), BSA-PEG5k-1 (0.1569 mL/g), BSA-PEG5k-2 (0.1569 mL/g), BSA-PEG10k-1 (0.1285 mL/g), BSA-PEG10k-2 (0.1216 mL/g), BSA-PEG30k (0.1454 mL/g).

3.2.13 Ultraviolet-Visible Spectroscopy (UV-Vis)

UV-Vis was performed on a Cary UV-Vis Spectrophotometer at 20°C in absorption mode over the wavelength range of 200 – 300 nm using a quartz micro cuvette filled with dilute solutions of BSA and mPEG-NHS in DI water. UV-Vis was used to confirm that BSA was retained in the membrane during dialysis while free mPEG-NHS was removed.

3.2.14 Small Angle X-ray Scattering (SAXS)

SAXS data was acquired under vacuum using a Rigaku S-Max3000 with a 2D multiwire detector. Two-dimensional SAXS patterns were azimuthally integrated to obtain plots of scattered intensity vs. momentum transfer vector, $q = (4\pi/\lambda) \sin \theta$, where θ is half the scattering angle and $\lambda = 1.54$ Å. Peaks were fit with Gaussian functions to determine the locations of the peak maxima.

Chapter 4: Applications in Innovative Materials Technologies: Enzyme-Actuated Polymer Membranes for Protective Garments

Reference: A manuscript on the work presented in the following chapter has been submitted: J.L. Poole, S. Donahue, D. Wilson, Y.M. Li, Q. Zhang, Y. Gu, R. Ferebee, Z. Lu, R.M. Dorin, L.F. Hancock, L. Takiff, I.F. Hakem, M.R. Bockstaller, U. Wiesner, and J. Walker, "Enzyme-Actuated Asymmetric Block Terpolymer Membranes for Localized Autonomous Sensing and Protective Applications."

4.1 Background and Motivation

Protective suits against chemical and biological agents are in increasing demand worldwide [87]. Current protective suit technology is based on static closed systems with low permeability to moisture and heat that exert a significant thermal burden on the wearer, shortening their effective time of use. To overcome these limitations, here we introduce the concept of a dynamically responsive suit, which only at the point of contact with an agent, locally switches into a closed protective state. Proof of principle experiments are demonstrated by integrating self-assembly with non-solvent induced phase separation (SNIPS) derived asymmetric and stimuli responsive block copolymer membranes characterized by narrow mesopore size distributions with enzymes displaying high substrate specificity and fast response times [2,88–90]. These act as highly selective actuators, triggering the closure of the pores upon encounter of an agent via local acidification. The materials are compatible with large area fabrication and integration with other support and protective membranes to achieve required properties including material strength, moisture vapor transmission rates (MVTR), as well as fast response times.

The current state of the art in chemical and biological protective clothing utilizes layering technology, wherein static barrier materials are stacked to mitigate contaminant breakthrough. In recent years, these materials have been enhanced by incorporating additives such as sorbents, metal catalysts, oxidizers, quaternary amines or enzymes to act as rudimentary decontaminants

and biocides [91–94]. While such additions can offer enhanced protection, they do not provide the speed, selectivity, or molecular capacity to address complex threats as they arise in dynamic environments. In addition, the complexity of production and limited lifetime of these materials result in unsustainable financial costs that limit the benefits of protective technologies to small numbers of personnel. The most significant challenge, however, is that these enhancements do not address the significant physical burden to the user due to the poor water vapor transport, heat management, and sheer bulk of the material. As a result of these barriers, wearers typically can only operate in full protective state for less than an hour.

To advance the field of protective materials, a paradigm change must be accomplished which enables a logic-gated sense and rapid response capability against threats. The design of such a platform hinges on the development of a molecular algorithm to effectively sense and transduce the presence of a threat into a localized dynamic material response capable of providing necessary protective functions such as, shedding, decontamination, or permeability reduction, in the immediate area of impact. This "smart" material function should not affect the non-contaminated portion of the suit and should not disturb the user in any way. Such a solution requires the combination of a high quality stimuli-responsive material with a sensing element capable of specific and rapid agent recognition. Finally, the material must be amenable to low-cost manufacturing to be a truly viable solution to this real-world problem.

An inspiration can be found in the function of biological skin in which embedded molecular systems sense the environment and locally actuate vapor, fluid, and heat transport processes in response to external conditions. Here we present a "molecular algorithm" towards actively-gated membrane systems with molecular recognition that mimics skin-like functionality by integration of enzymes into mesoporous and pH-responsive asymmetric polymeric films. The resulting bio-

mimetic membranes are capable of a rapid and spatially selective response to specific threat agents and can be integrated into robust material systems consistent with clothing or suit applications. A simplified illustration (top surface only) of the asymmetric structure and functionality of the new membrane system is provided in

Figure **4-1**.

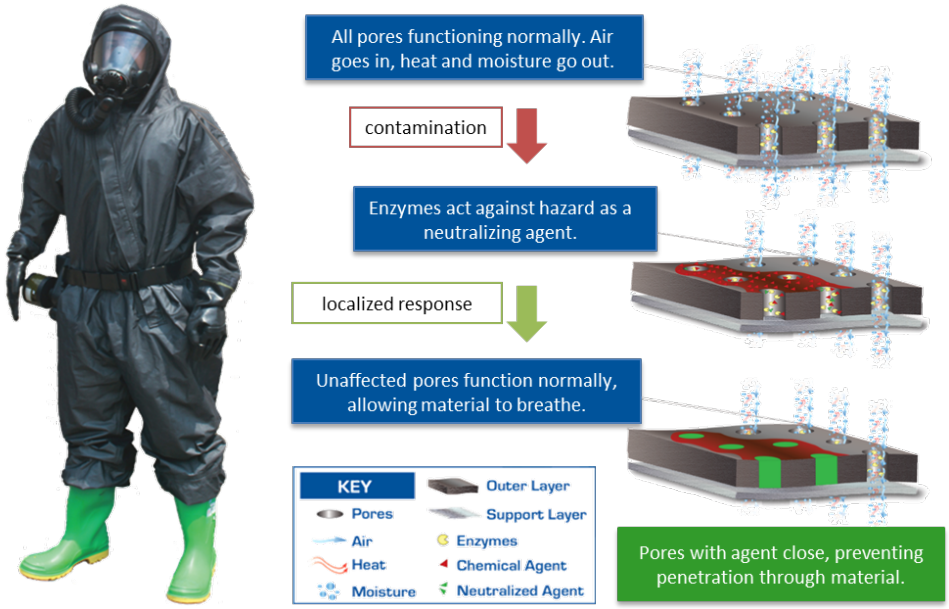

Figure 4-1. Design of an autonomous dynamic response material for protective applications. Substance recognition via enzymatic sensors locally activates a permeability response within the dynamic material. Active or passive removal of enzyme substrate and products leads to reset of the material for additional rounds of response. For simplicity, only the top surface layer of the asymmetric block copolymer membrane is shown.

Initially, the enzyme-linked material is highly permeable, allowing unhindered air, heat, and moisture flux. Upon exposure to a recognized threat (i.e. enzyme substrate), the agent is catalytically destroyed. Acidic enzymatic decomposition products induce a localized reduction in chemical diffusion across the membrane while unexposed portions of the material remain freely permeable. Once the threat is neutralized the material can be reset for additional rounds of response.

4.2 Sample Preparation

4.2.1 Materials

All compounds and solvents were used as received unless otherwise noted. Phosphotriesterase (PTE) was obtained from Novozymes (Davis, CA) and exchanged into 50 mM potassium phosphate, 100 uM cobalt chloride, pH 8.0 for storage at 4 °C until use. Enzyme variants PTE(RN-YT) and PTE(C23) were prepared in-house according to previously published procedures [75,76]. pH-Sensitive dye 1 was custom synthesized and purchased from American Dye Source, Inc. (Quebec, Canada). Ethyl paraoxon (>98%) was purchased from Chem Service, Inc., and Diisopropylfluorophosphate (>97%) was acquired from Sigma-Aldrich.

4.2.2 Polymer and Membrane Preparation

The detailed preparation of the triblock terpolymer ISV, and mesoporous asymmetric membranes derived from ISV, has been described elsewhere [5]. Here five ISV triblock terpolymers were synthesized by anionic polymerization. Total number average molar mass, M_n, weight fraction, f, and polydispersity index, PDI, for these terpolymers as experimentally determined by gel permeation chromatography (GPC) and proton nuclear magnetic resonance (^{1}H NMR) are summarized in Table 4-1.

Table 4-1. ISV triblock terpolymer characteristics.

Sample	M_n [kg mol^{-1}]	f_{PI}	f_{PS}	f_{P4VP}	PDI
ISV43	43	0.24	0.56	0.20	1.02
ISV99	99	0.23	0.63	0.14	1.20
ISV117	117	0.26	0.60	0.14	1.13
ISV118	118	0.21	0.67	0.12	1.12
ISV119	119	0.19	0.65	0.16	1.17

ISV membranes were fabricated by employing a combination of self-assembly and non-solvent induced phase separation, now referred to as SNIPS [77]. An ISV polymer casting solution was prepared by dissolving ISV polymer into a co-solvent mixture comprised of a 7:3 ratio (by weight) of 1,4-Dioxane (DOX) and tetrahydrofuran (THF). The solution was pipetted onto a glass substrate for neat, unsupported membranes. Supported membranes were cast directly onto porous nylon substrates, purchased from Sterlitech Inc., taped to glass substrates. The polymer solution was cast by a doctor blade with a gate height of 220 μm and allowed to evaporate for a specified amount of time before the films were immersed into a deionized water bath. Unless mentioned otherwise, membranes were cast from a 16% (ISV43), 12% (ISV99 and ISV118) or 11% (ISV117 and ISV119) (by weight) polymer solution. Membranes were cast on top of a 0.2 μm (ISV117), 0.1 μm (ISV43, ISV99, ISV119) or 0.04 μm (ISV118) nylon support. Membranes cast from ISV117 and ISV118 exhibited an open "finger-like" substructure while membranes cast from ISV43, ISV99 and ISV119 showed a dense "sponge-like" substructure [6,78]. It is assumed here that membranes cast from solutions that vary slightly in polymer concentration have similar properties and performance values.

4.3 Characterization Techniques

4.3.1 Moisture Vapor Transport Rate (MVTR)

An evaporative dish method, based on the British Standard BS 7209, was used to determine the MVTR in membrane samples [80]. The Turl dish assembly consists of a dish, triangular support, and cover ring. The test specimen is comprised of two circular membrane samples, with a total area of 402 mm^2, anchored to a circular transparency film, purchased from C-Line Products, Inc. (No. 60837), using epoxy. The test specimen was sealed over the mouth of the dish containing

deionized water and the triangular support to maintain a ~10 mm air gap. The cover ring was placed above the test specimen and adhesive tape was applied around the circumference of the competed assembly. The assembly was positioned into a turntable and the experiment was conducted in a controlled atmosphere of 20 °C and 65% relative humidity. The assemblies were weighed on a balance with a resolution of 0.01g. Each assembly was weighed daily up to five days in order to assure full equilibration. Data for calculation of MVTR values were taken on day five.

The MVTR (g m^{-2} day^{-1}) was calculated as:

$$\text{MVTR} = 24M(At)^{-1} \tag{27}$$

where M is the loss in mass of water in grams, t is the time period in hours, and A is the area of the membrane sample in m^2.

In addition to the three nylon-supported ISV membranes (ISV43, ISV99, and ISV199), dishes were evaluated in the open and closed states for reference. Values obtained from these measurements were used as benchmarks in addition to literature values reported for relevant commercially available material (i.e. PTFE and PU) [81].

4.3.2 Intrinsic Water Vapor Resistance

Intrinsic water vapor resistance was calculated as:

$$R_{et} = R_f(RT)\left(M_W \Delta H_{vap}\right)^{-1} \tag{28}$$

where R_f is the intrinsic mass transfer resistance of the sample, R is the universal gas constant, T is temperature, M_w is molar mass of water, and ΔH_{vap} is the enthalpy of vaporization of water.

4.3.3 Tensile and Flex Deformation

Tensile testing of the membranes was performed on an Instron (model 4442) equipped with a 1 kN load cell with loading strain rates of 1, 10, and 100 mm min^{-1}. The samples were 13 mm x 20 mm with a thickness of 0.11 mm. Stress-strain curves were constructed, and the Young's Modulus was determined by calculating the slope within the proportionality limit of the curve. The toughness was calculated by integrating the stress-strain curve over the entire deformation range. Samples were fixated and repeatedly flexed (three sets of 10 flexes) to a curvature of 3 cm^{-1} at a rate of 0.5 Hz.

4.3.4 ISV Enzyme / Dye Adsorption

Supported ISV membranes were incubated in solutions of PTE enzyme (1-20 mg mL^{-1}, 10 mM CAPSO, pH 9.4, 500 μL per 100 mm^2 membrane surface area) for 16 hours at 4 °C on an orbital shaker at low speed. For samples containing dye 1, 100 μL of a 10 mg mL^{-1} stock solution in water was added to the protein solution for every 100 mm^2 membrane surface area. Post-immobilization, samples were washed (3x) with 10 mM CAPSO, pH 9.4 buffer for 30 minutes at 4 °C on an orbital shaker at low speed prior to testing.

4.3.5 Colorimetric and Fluorescent Visualization

Visual images of colorimetric results were recorded using a Cannon PowerShot A4000 IS HD camera. Supported ISV117 membranes functionalized with enzyme (PTE(C23) or PTE(YT)) and dye 1 were dried under ambient conditions for 5 minutes prior to challenge with simulant and control solutions (1 uL). Colorimetric response was observed and recorded within 1 minute of liquid challenge.

Vapor-induced fluorescence emission images of supported ISV117 membranes functionalized with PTE(C23) and dye 1 were captured on an Oculus Photonics imager equipped with a ThorLabs 800 nm long pass filter operating in monochrome video mode. Fluorescent samples were excited using a HHE 735 nm LED on high power. Membranes were dried under ambient conditions for 5 minutes and suspended from the top of a closed vessel prior to simulant challenge (neat DFP (5 uL) deposited in the bottom of a 30 mL test vessel). Continuous video was recorded over 10 minutes and still frames were extracted for relevant time points (time = 0 or 2.5 minutes).

4.3.6 Permeability Studies

Permeability measurements were performed by placing membranes into a stirred cell concentrator (Amicon 8010, Millipore Co.; EMD Millipore 5121) with 50 mM buffers (imidazole, acetate) at various pH. Pressure was applied using nitrogen and, while stirring, the liquid that passed through the membrane was collected in a beaker positioned on a balance. Mass data collected at specified time intervals (10 or 15 seconds) and used to determine permeability in liters per meter squared per hour per bar ($Lm^{-2}h^{-1}bar^{-1}$). Measurement of enzyme-mediated permeability change was completed using PTE(RN-YT)-bound membranes. For these samples, an open pore state permeability was established with 1 mM imidazole, pH 6.5 (ISV119, L_p = 50-75 $Lm^{-2}hr^{-1}bar^{-1}$). The average permeability values of the protein-functionalized membranes were slightly lower than that measured for native membrane samples due to enzyme binding. Once the residual buffer volume above the membrane reached approximately 1 mL, paraoxon solution (40 mM in methanol, 70, 150, or 200 uL) was delivered through a septum in a modified stirred cell apparatus. Final material permeability was measured in the closed state for each

simulant challenge level (70 uL, L_p = 20 $Lm^{-2}hr^{-1}bar^{-1}$ and >150 uL, L_p = 1.2 $Lm^{-2}hr^{-1}bar^{-1}$). The percent permeability was normalized using the absolute difference between the open and closed state measured for each membrane over the time scale of the experiment.

4.3.7 Electron Microscopy

Membrane surface morphology and cross section were characterized by field emission scanning electron microscopy (Tescan Mira3 FESEM). Sample surface was coated with gold palladium at a current of 40 mA for 6 seconds (Denton Vacuum Desk II) prior to imaging. Average pore sizes from FESEM micrographs were analyzed with Mathematica.

Transmission Electron Microscopy (TEM) was performed using a JEOL 2000 EX electron microscope operated at 200 kV. Imaging was done by amplitude and phase contrast, and images were acquired using a Gatan Orius SC600 high-resolution camera. Samples were stained for 2-30s with Phosphotungstic Acid (PTA) to increase the contrast between the P4VP / enzyme components and the membrane.

4.3.8 Ellipsometry Studies

Ellipsometry measurements were conducted using a Beaglehole Instruments Picometer phase-modulated ellipsometer equipped with a helium-neon laser (λ=632.8 nm). The angle of incidence was varied from 70-80°, and analysis was completed using TF Companion software (Version 3.0, Semicon Software, Inc.) and a four layer, homogeneous film model (semi-infinite silicon + silicon dioxide + polymer + adsorbed enzyme + semi-infinite air). Thin films of PI, PS, P4VP, and ISV with thicknesses between 10 – 20 nm were spin cast from 0.1 wt. % solutions in toluene (PI, PS, and ISV) and a 1:1 mixture of acetone and ethanol (P4VP) onto silicon wafers. The polymer-coated wafers were incubated in a solution of PTE enzyme (9.7 mg mL^{-1}, 10 mM

CAPSO, pH 9.4) for 16 hours at 4°C on an orbital shaker at low speed. The layer thickness was successively determined for the silicon dioxide layer (2-3.5 nm), the polymer layer (10-20 nm), and the adsorbed enzyme. Literature values of refractive indices for PI (1.51), PS (1.59), P4VP (1.581), ISV (1.5707), and dry enzyme (1.53) were used for the analysis [82–84].

4.3.9 PTE Enzyme Activity and Adsorption

Direct phosphotriesterase hydrolysis assays were performed on a Molecular Devices SpectraMax M2e spectrophotometer in 96 well plates for solution-phase enzyme samples (100 μL reaction volume, 0.35 mm path length, 5 min kinetic duration) and on a Beckman Coulter DU530 UV/VIS spectrophotometer, transferring aliquots of assay solution samples to a cuvette for solid-phase enzyme samples (1 mL volume, 1 cm path length, 10 min kinetic duration). All assays were completed at 25 °C against ethyl paraoxon and the rates were measured by monitoring the release of p-nitrophenol (ε_{405} = 17100 $M^{-1}cm^{-1}$). Substrate stock solutions were prepared by the dissolution of diethyl paraoxon in dry methanol (152 mM) followed by dilution of the methanol stock in deionized water (15.2 mM). For the enzymatic reaction, aliquots of the 15.2 mM paraoxon stock were added to a mixture of enzyme in reaction buffer (50 mM CAPSO, 50 μM $CoCl_2$, pH 9.0) to give a final concentration of 1.52 mM. A dilution series of enzyme concentrations was used for solution-phase samples (final enzyme concentrations range from 1 ng-10 μg mL^{-1}) to achieve a linear rate. For solid-phase samples, a section of membrane was submerged in an adequate volume as to maintain a linear rate over the course of the kinetic assay (typical conditions: 3 mm diameter circle, 2 mg mL^{-1} enzyme incubation, 12 mL assay buffer). The initial enzymatic rates were corrected for the background rate of spontaneous paraoxon

hydrolysis in the absence of enzyme. Specific activity values of the solution-phase samples were calculated using the following formula:

Specific Activity (umol min^{-1} mg^{-1}) = ΔmAU min^{-1} x (1 x 106) x DF x (1000 x 17100 x 0.35 x C)$^{-1}$, where $\Delta mAU\ min^{-1} = \Delta mAU\ min^{-1}\ test - \Delta mAU\ min^{-1}\ blank$, *DF* is the dilution factor, $17{,}100\ M^{-1}\ cm^{-1}$ is the molar extinction coefficient of p-nitrophenol, *C* (in mg L^{-1}) is the protein concentration of enzyme stock solution and *0.35 cm* is the path length of light.

Quantitation of active enzyme loading of solid-phase samples was calculated using a calibration curve prepared from the rates of enzymatic paraoxon hydrolysis (linear regression of absorbance vs. time) for a series of solution-phase enzyme standards of known concentration and identical specific activity as that incubated with the membrane. The resulting equation was then compared against the hydrolysis rates obtained for the solid-phase samples to calculate enzyme mass loading (ng) per unit area (mm^2).

Enzyme stability during dry storage on supported ISV119 membranes was assessed in the presence and absence of stabilizing excipient for a range of temperatures over a 30 day incubation period. Enzyme functionalized membranes were prepared as described in the *Materials: Enzyme Actuated Polymer Membranes* section. Upon completion of the final rinse, excipient stabilized membranes were subjected to an additional incubation in a 1% collagen hydrolysate solution (3 mm diameter ISV119, 500 uL solution, 30 min, 4 °C), after which both native and stabilized membranes were lyophilized to dryness and individually packaged under nitrogen in Mylar bags for storage. Samples were incubated at 4, 25, 40, or 60 °C for up to 30 days, with activity time points collected on days 0, 10, and 30. At each time point the enzyme activity was assessed by >4 replicates. Pretreatment of samples with excipient significantly helped to maintain enzyme activity of the dried samples as measured on day 0.

4.4 Results & Discussion

The material system to demonstrate the general "molecular algorithm" for suit production required the use of a responsive base material with uniform pore size and robust mechanical properties. Block copolymer (BCP) self-assembly (SA) based asymmetric ultrafiltration membranes derived from industry-proven non-solvent induced phase separation (NIPS) process have recently emerged as an alternative class of stimuli responsive materials [2]. In particular, working with the triblock terpolymer poly(isoprene-*b*-styrene-*b*-4-vinylpyridine) (ISV) has allowed combination of narrow pore size distributions with high toughness down to pore sizes below 10 nm while at the same time opening pathways to large-scale membrane fabrication [5,6]. Here membranes were prepared using SA plus NIPS (SNIPS) of five ISV terpolymers with molar masses in the range of 40-120 kg mol^{-1} (ISV43, ISV99, ISV117, ISV118 and ISV119, see *Polymer and Membrane Preparation* section). ISV membranes exhibited a hierarchical structure comprised of a thin top surface separation layer of vertically aligned uniform mesopores and a substructure of graded meso- to macropores, with all surfaces lined by the poly-4-vinylpyridine (V) block of the terpolymer [5]. Due to the sensitivity of P4VP (pKa 5.62) to protonation, mesoporous ISV membrane permeability was highly pH-sensitive, as seen in Figure 4-2a&b. Membranes featured a rapid and effective transition between "open" and "closed" states upon pH change from Lp = 1522 $Lm^{-2}hr^{-1}bar^{-1}$ (at pH = 7) to Lp = 11 $Lm^{-2}hr^{-1}bar^{-1}$ (at pH = 3) as a result of electrostatic repulsive interactions leading to poly-4-vinylpyridine chain stretching in the mesopores (Table 4-2). Beyond the ordered top surface separation layer, two types of substructures (Figure 4-2c) with either a densely packed "sponge-like" or large open "finger-like" morphology were observed. Figure 4-2 depicts SEM micrographs revealing the uniform mesopore top surface structure and the hierarchical substructure of supported ISV membranes.

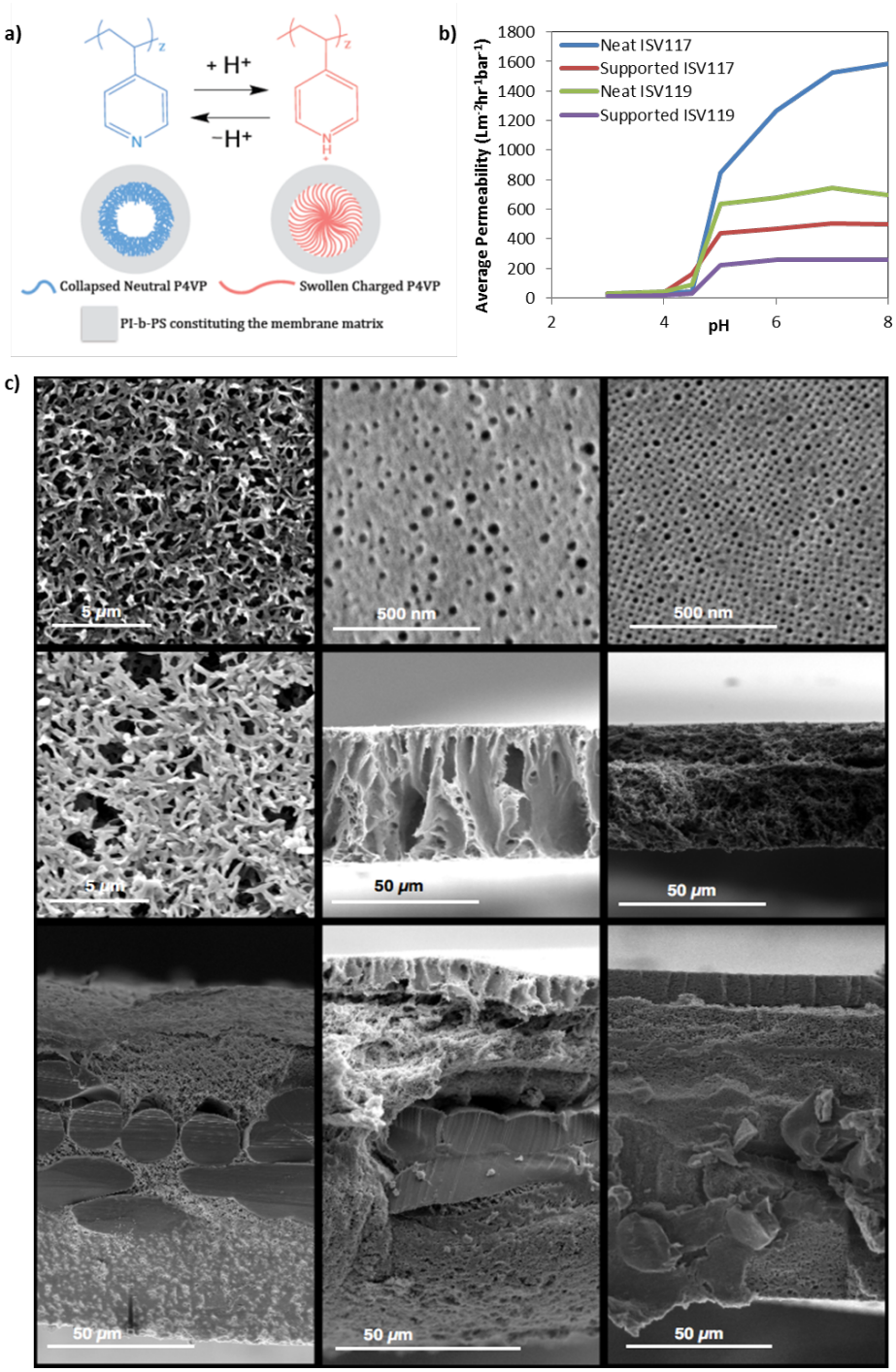

Figure 4-2. Characterization of native ISV behavior and structure. a) Schematic of pH dependent behavior of the P4VP block of ISV membranes. Pores in open (deprotonated) and closed (protonated) states are responsible for membrane permeability changes. b) Material permeability of neat and supported ISV117 and ISV119 membranes in buffer solution as a function of pH. c) SEM structural characterization of nylon support (left, top: 0.1 µm top surface; middle: 0.2 µm top surface; bottom: 0.2 µm cross section), nylon-supported ISV117 membrane with finger-like substructure (middle), and ISV119 membrane with sponge-like substructure (right). For ISV membranes top images show surface structures, middle images show the neat ISV membrane cross sections and bottom images show cross sections of nylon supported membranes.

Table 4-2. Absolute permeabilities in the "open" and "closed" state of neat and supported ISV117 and ISV119 membranes.

	"open" state (pH=7) ($Lm^{-2}hr^{-1}bar^{-1}$)	"closed" state (pH=3) ($Lm^{-2}hr^{-1}bar^{-1}$)
Neat ISV117	1522	32
Supported ISV117	504	27
Neat ISV119	747	29
Supported ISV119	257	11

Membranes with "finger-like" substructures were obtained with ISV117 and ISV118 while "sponge-like" substructures were obtained with ISV119 under the conditions described in the *Polymer and Membrane Preparation* section. Variations in permeability can be attributed to the difference in substructure, as shown in Figure 4-3a&b.

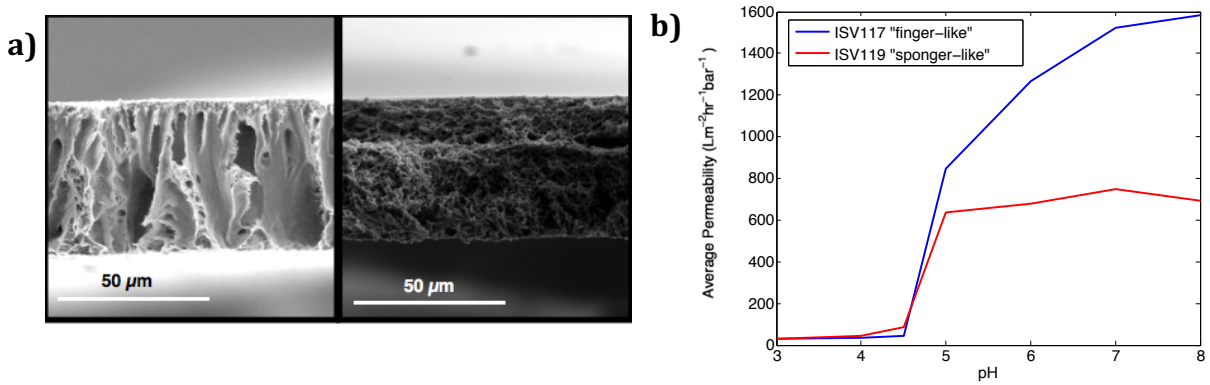

Figure 4-3. a) SEM micrographs of neat cross sections of ISV117 membrane with "finger-like" substructure (left) and ISV119 membrane with "sponge-like" substructure (right). b) Permeability of neat ISV117 and ISV119 membranes in buffer solution as a function of pH.

As shown in Figure 4-4, membranes cast from ISV117 at 11% (left) and 9% (right) polymer solution have similar surface morphologies and "finger-like" substructures. As expected, these membranes perform similarly (i.e. permeability as a function of pH) but differ in absolute permeability values due to polymer concentration.

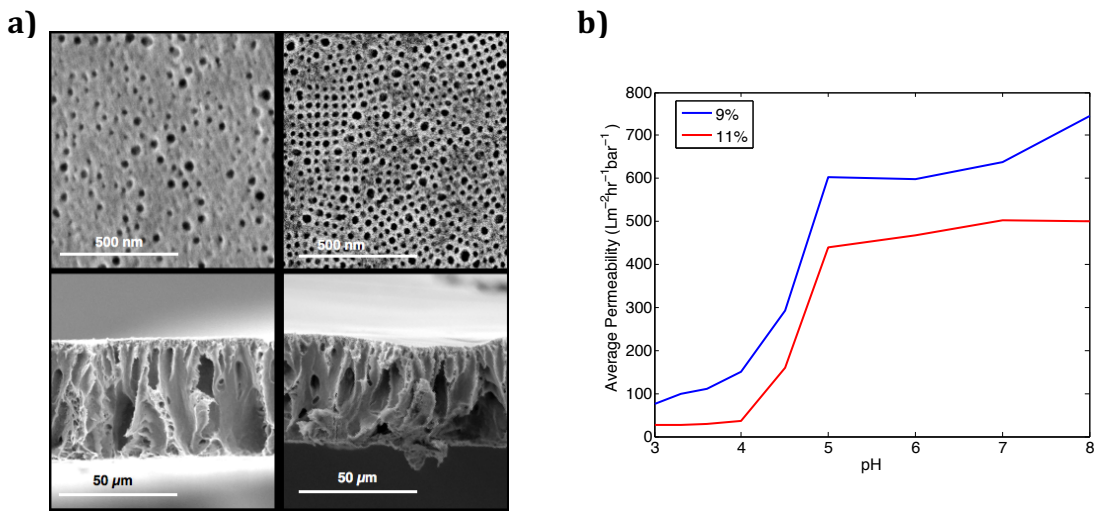

Figure 4-4. a) SEM micrographs of ISV117 membranes casted from 11% (left) and 9% (right) polymer solution with "finger-like" cross sections of neat ISV117 membranes (bottom). The top images show surface morphology of nylon-supported ISV117 membranes. b) Permeability of supported ISV117, casted from 11% and 9% polymer solution, membranes in buffer solution as a function of pH.

Large area fabrication of ISV118 membranes on 0.04 μm nylon supports was achieved while retaining the expected surface morphology and permeability response, as presented in Figure 4-5.

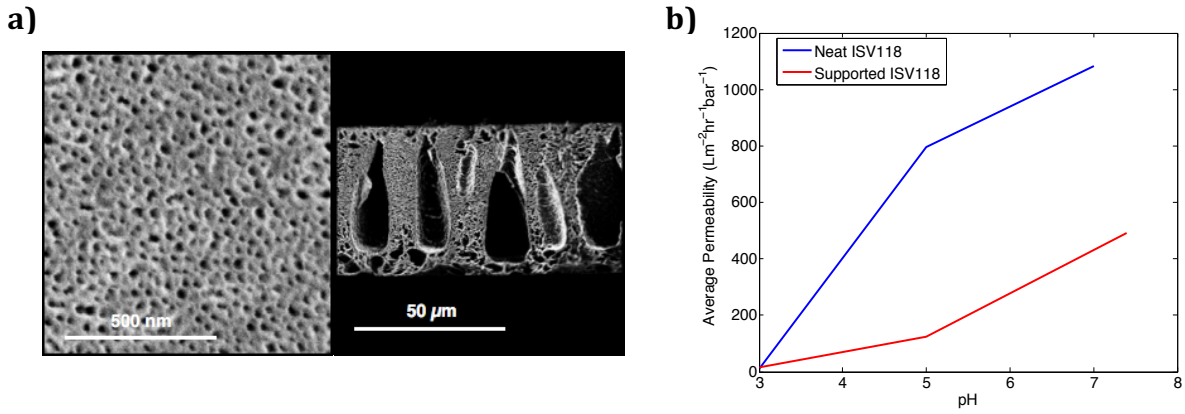

Figure 4-5. a) SEM micrographs of the surface morphology and neat cross section of ISV118 membrane with "finger-like" substructure b) Permeability in buffer solution as a function of pH for supported ISV118 membranes cast on 0.04 μm nylon supports.

Additional images of supported ISV 119 and ISV118 membranes from SEM and TEM analysis show the physical appearance, top structure, cross-section, and separation layer in Figure 4-6.

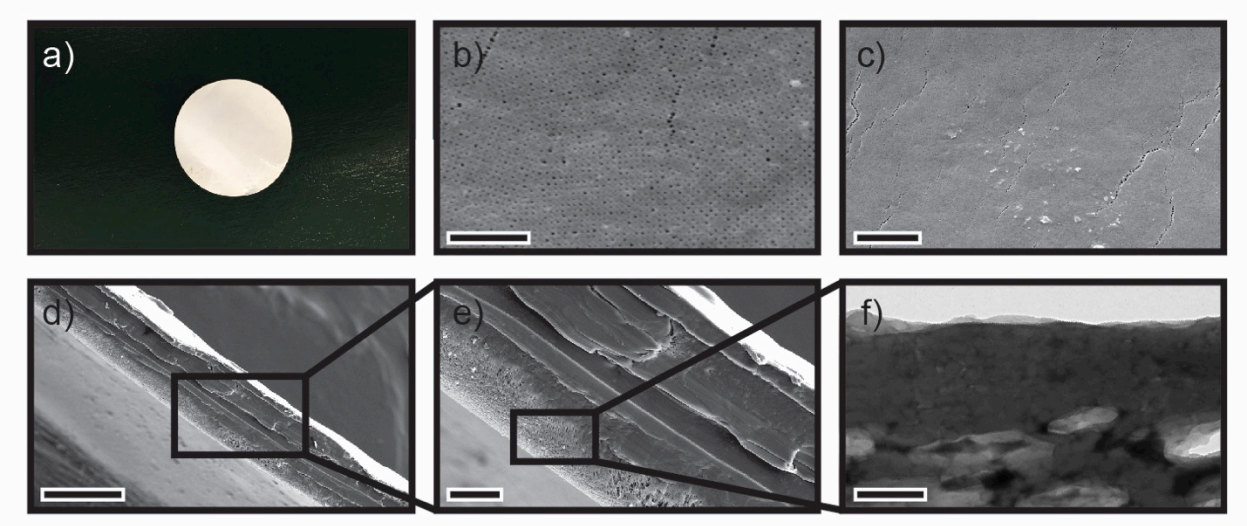

Figure 4-6. a) Image of ISV119 membrane cast on nylon. (b&c) SEM micrographs of the top surface of ISV119 membrane. (d&e) SEM micrographs of the cross section of the ISV119 membrane. (f) TEM micrograph of ISV118 membrane separation layer stained with PTA.

Values for the absolute permeabilities in the "open" and "closed" state of neat and supported ISV118 membranes are presented in Table 4-3.

Table 4-3. Absolute permeabilities in the "open" and "closed" state of neat and supported ISV118 membranes.

	"open" state (pH=7) ($Lm^{-2}hr^{-1}bar^{-1}$)	"closed" state (pH=3) ($Lm^{-2}hr^{-1}bar^{-1}$)
Neat ISV118	1082	10
Supported ISV118	491	15

Variation in polymer composition and membrane casting conditions can be used to control pore size, shape, density and substructure architecture to match the permeability profile of the resulting membrane to respective specifications [6]. In order to improve the mechanical stability of the mesoporous polymer films, ISV membranes were cast on nylon supports (Figure 4-2c). The resulting membranes were pliable yet robust (Figure 4-7a); maintaining physical and mechanical integrity under extensive experimental manipulation, including permeability testing under pressures up to 30 psi. All membrane systems were found to exhibit "open" state

permeability in excess of L_p = 200 $Lm^{-2}hr^{-1}bar^{-1}$ and the fidelity of pH-induced permeability changes was found to exceed 1 db. Most importantly, permeability and transduction characteristics were uniform across large area membranes – a prerequisite for a suit-based textile application.

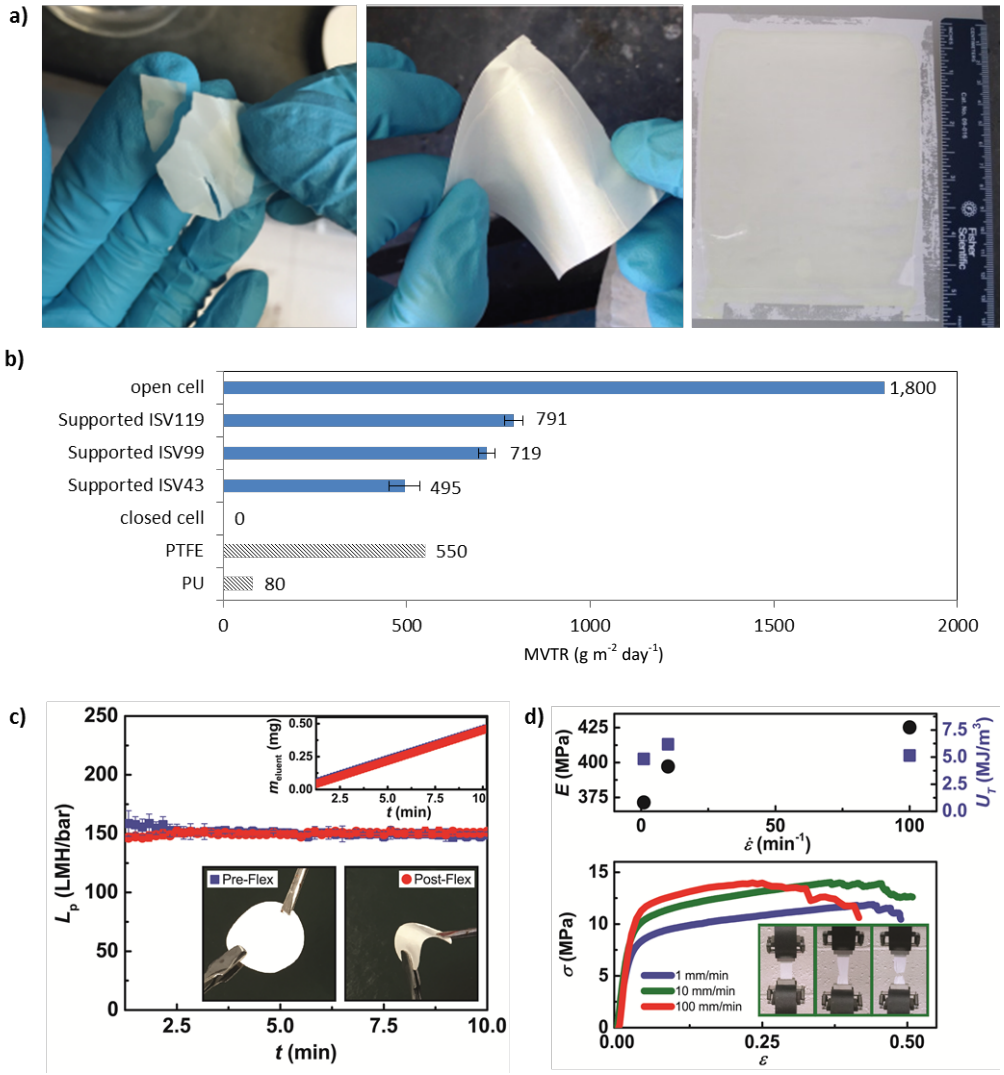

Figure 4-7. Characterization of unfunctionalized ISV membrane properties. a) Images demonstrating brittle character of neat ISV119 membrane (left), pliable quality of nylon supported ISV119 membrane (middle), and scale-up potential of membranes via large area (4"x5") blade casting with ISV118 (right). b) Moisture vapor transport rates (MVTR) based on the British Standard BS 7209 of supported ISV membranes varying in molar mass as compared to reference samples (open and closed dish) and in relation to commercial materials (PTFE, PU). c) ISV119 permeability profile shown to be essentially unchanged post flex testing. d) Supported ISV119 tensile testing stress vs. strain curves with photographs of the test setup.

To evaluate critical textile properties of the supported membranes, moisture vapor transport rate (MVTR), intrinsic water vapor resistance, and durability were assessed including tensile and flex deformation, as depicted in Figure 4-7b-d and summarized in Table 4-4. In general, ISV membranes provided MVTR values similar to those of standard commercial membrane textiles, such as PTFE (MVTR ~ 550 g m^{-2} day^{-1}). Evaluation of MVTR across several ISV membrane compositions (ISV43, ISV99, ISV119) revealed a range of accessible vapor transport (~500-800 g m^{-2} day^{-1}) and highlighted the tunable properties of the membrane as a function of polymer molar mass, casting conditions and membrane pore size. Elastic moduli (E ~ 400 MPa) and ductility (ε_{max} ~ 0.5) were found to be comparable to commercial materials, such as GoreTex^{TM}, and approximately independent of strain rate. Figure 4-8 depicts SEM micrographs of nylon supported ISV119 before and after tensile testing. Permeability response of the supported material was unaffected by repeated (10x) flex deformation to film curvatures of 3 cm^{-1}. The scalability of the compound membrane structure was demonstrated through the fabrication of mid-gauge membrane swatches. These samples, produced in a single continuous casting process, measured approximately 4”x5” and displayed the same homogeneity, consistent pore structure, and permeability response observed at smaller scales.

Table 4-4. ISV triblock terpolymer resistance to evaporative heat transfer.

Sample	R_{et} [m^2 Pa $Watt^{-1}$]
tefzel film	2690
ISV119 “open”	8.8
ISV119 “closed”	9.6
Supported ISV119 “open”	13.2
Supported ISV119 “closed”	14.2
open cell	6.2

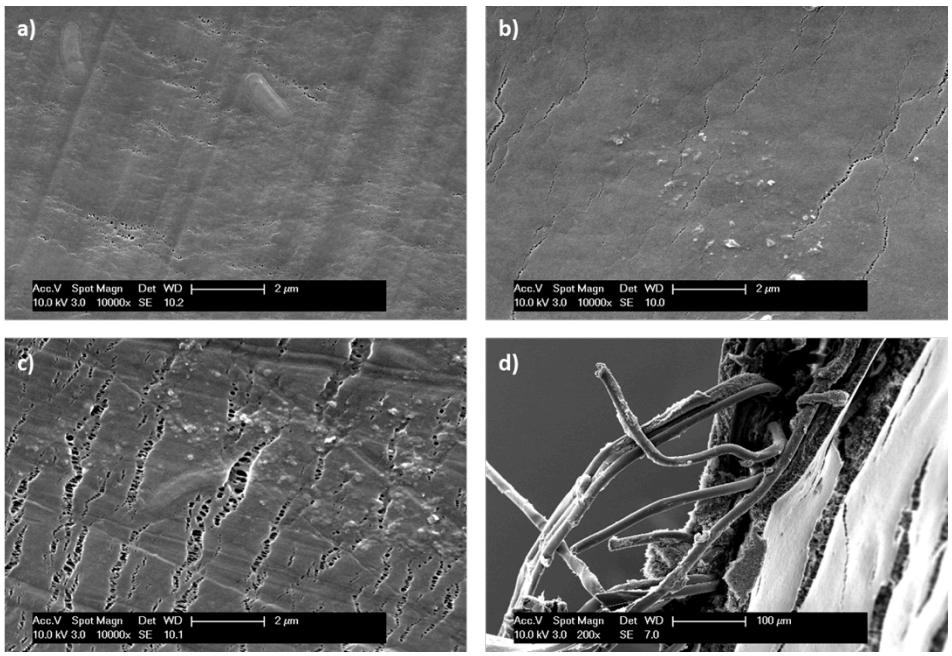

Figure 4-8. SEM micrographs supported ISV119 before and after durability testing. Top surface of membrane a) before and b) after flex testing. c) Top surface and d) cross section of membrane after tensile testing.

To impart target-specific response characteristics, supported ISV membranes were conjugated to hydrolase enzymes, which have demonstrated use in the identification, quantitation, and decontamination of threat agents [95]. Due to the pH-based material response mechanism, functionalization of the ISV membrane focused primarily on enzymes that act on relevant threat agents to produce highly acidic products. Select variants of these catalysts are capable of generating large changes in pH with excellent substrate specificity and rapid response times toward a number of chemical and biological agents of interest. By coupling the selectivity and quick response of enzymes with stimuli responsive materials, a dynamic system can be prepared which responds only to enzyme substrates with high sensitivity. Phosphotriesterase (PTE, EC 3.1.8.1) is known for the rapid detoxification of a wide range of organophosphate pesticides and chemical agents. Hydrolysis of these agents via PTE catalysis generates strong and weak acid products, as shown in Figure 4-12a [75,76,96]. Incorporation of PTE into the ISV membranes

effectively creates a lock-and-key-type permeability barrier to the chemical diffusion of these agents and prevents exposure when incorporated into a protective suit format.

Adsorption is a widely applicable and inexpensive enzyme immobilization method to attach a broad array of protein structures to a surface. Surface adsorption techniques are well established in the manufacture of low-cost protein-based diagnostic and sensing devices. Enzyme coupling was accomplished by immersion of membranes into concentrated enzyme solutions, harnessing the strong interactions between enzymes and P4VP on the outer surface of the ISV membrane [97]. Thickness measurements of enzyme coatings adsorbed on P4VP reference films using ellipsometry revealed the formation of enzyme monolayers that were stable against desorption during repeated washing with deionized water, detergents, and ionic solutions with pH ranging between 4-10. A schematic and images of the ellipsometry thin film samples are shown in Figure 4-9. Measurement results from ellipsometry are presented in Table 4-5 for PI, PS, P4VP, and ISV thin films.

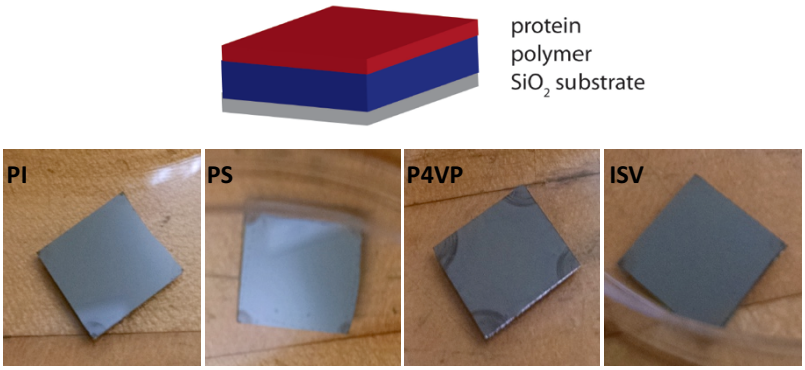

Figure 4-9. Images of protein adsorbed to homopolymer samples spun-cast on silicon wafers.

Table 4-5. Thickness values of silica layer on silicon support, homopolymer layer, and protein adsorption layer as derived from analysis of ellipsometry measurements.

Material	Silica (Å)	Polymer (Å)	Protein (Å)	Protein (ng mm^{-2})
polyisoprene	34.8 ± 0.4	98.9 ± 8.9	3.0 ± 2.3	0.39 ± 0.29
polystyrene	26.2 ± 2.2	153.6 ± 8.2	24.0 ± 8.2	3.12 ± 1.06
poly-4-vinylpyridine	20.0 ± 0.3	200.5 ± 5.2	35.8 ± 5.2	4.65 ± 0.67
ISV	21.1 ± 0.3	142.5 ± 2.2	23.6 ± 5.4	3.06 ±0.07

ISV membranes treated with solutions of PTE demonstrated high nonspecific enzyme binding with potential active enzyme loadings exceeding 150 ng mm-2, as shown in Figure 4-10.

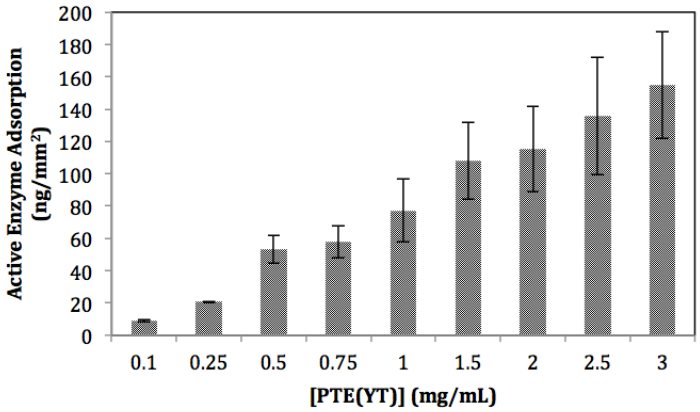

Figure 4-10. Representative quantities of PTE(YT) enzyme adsorption per unit surface area (ng mm^{-2}) to supported ISV119 according to solution-phase enzyme incubation concentration.

The ISV-adsorbed enzyme retained excellent activity in solution and upon drying, even after extended storage, as depicted in Figure 4-11.

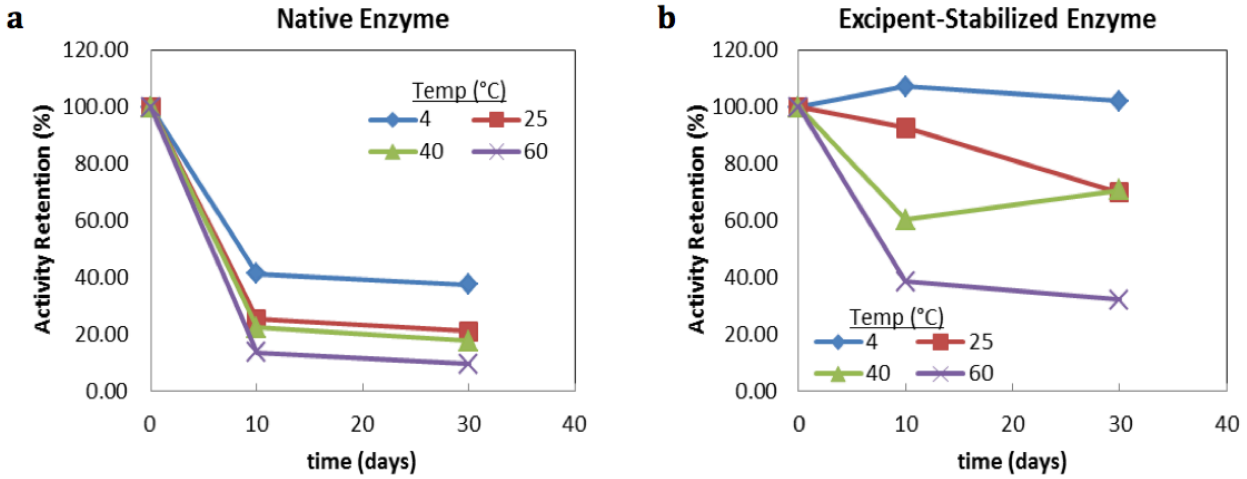

Figure 4-11. Stability of ISV119-adsorbed PTE(YT) enzyme activity to dry storage conditions in the (a) absence or (b) presence of excipient.

Visual detection of ISV-bound enzyme activity was demonstrated through the use of a pH-sensing cyanine indicator dye (dye 1), as presented in Figure 4-12b [98]. The structure of dye 1 was chosen for the pKa = 4.7, which is close to that of the conjugate acid of P4VP that drives the

ISV permeability transition. Upon acidification, the absorption peak of dye 1 shifts from red (λ_{abs} = 755 nm, pH > 5) to blue (λ_{abs} = 513 nm, pH <5) and fluorescence emission is increased in the near-IR region (λ_{em} = 773 nm). These spectroscopic changes in the dye were used to confirm enzyme function and predict potential modulation in the ISV membrane permeability. With this system it was possible to analyze enzyme function under wet and dry conditions to investigate liquid and vapor phase substrate response. Dye and PTE functionalized-ISV membranes were treated with two organophosphate substrates, paraoxon and diisopropylfluorophosphate (DFP) (Figure 4-12c). Acidic liquids, such as aqueous HCl or pre-hydrolyzed DFP, quickly turned both native and enzyme-treated ISV-1 material blue. Aqueous base did not alter material color. Paraoxon (pKa > 5), an excellent PTE substrate, produced an indicative "positive" blue response in only those samples pre-treated with enzyme. Samples without enzyme remained unchanged. These "positive" results were obtained using two PTE sequence variants with differing substrate affinity, (PTE(C23) and PTE(YT)), and demonstrate the potential to address multiple threats in a single platform through designed enzyme selection and combination. Enzyme response was also confirmed for vapor-phase agents using the volatile simulant DFP. As with the liquid challenges (*vide supra*), only materials pre-functionalized with enzyme produced a fluorescent response to DFP vapor while membranes without enzyme remained unchanged (Figure 4-12d). In addition to positive enzyme function, observation of the dry membranes allowed for visualization of response location. Color change of the indicator exclusively in the agent-treated area validated the high spatial selectivity to the immediate zone of contamination, a key aspect of the desired "smart suit" function.

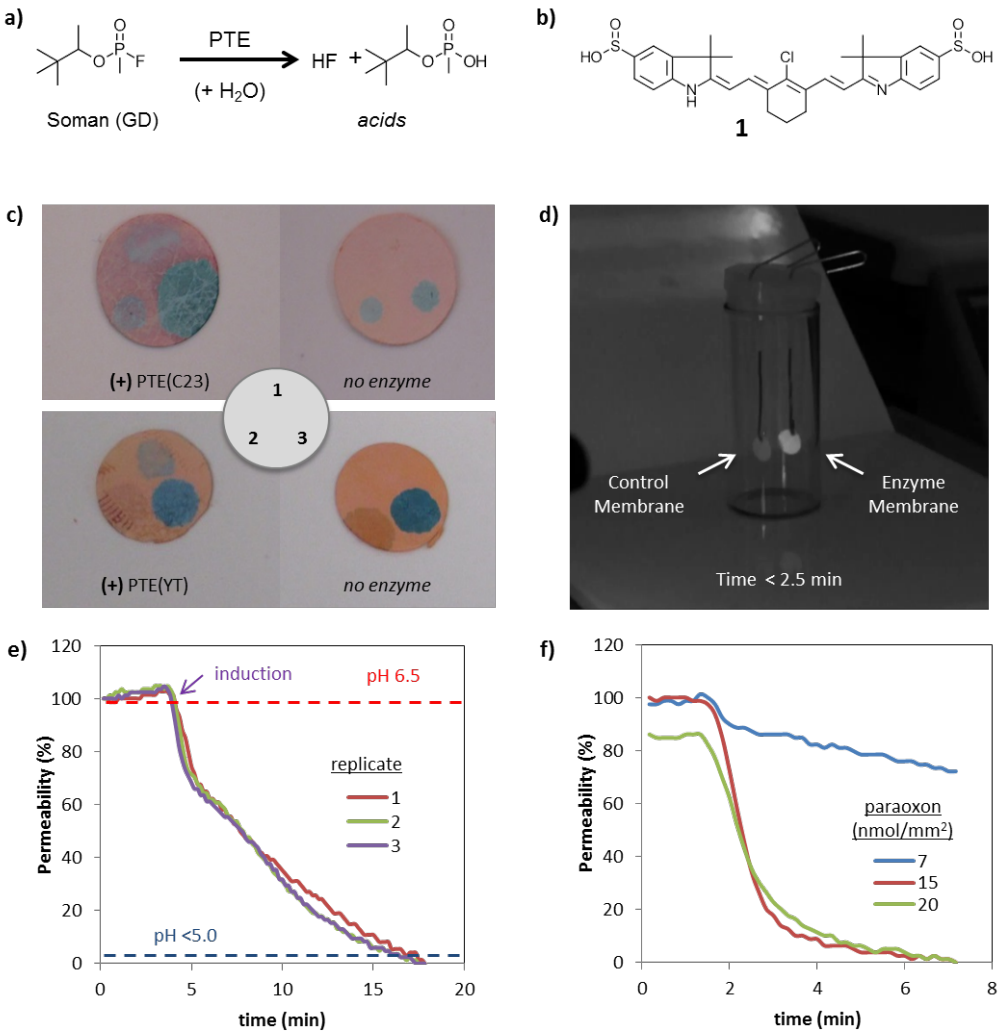

Figure 4-12. Substrate induced dynamic permeability response of enzyme functionalized ISV membranes. a) Reaction of phosphotriesterase (PTE) enzyme-mediated chemical agent hydrolysis creating acidic products that drive pH-dependent ISV permeability response. b) Cyanine dye structure for the colorimetric and fluorescent detection of environmental pH <4.5. c) Visualization of selective substrate turnover in the presence of active enzyme adsorbed on the surface of dyed ISV117 membranes (cast from a 9% polymer solution) in the presence and absence of PTE enzyme variants. Test key: 1. 15.2 mM paraoxon in a 10% methanol water solution; 2. Either neat DFP (top) or 1 M NaOH solution (bottom), 3. 1 M HCl solution. d) Visualization of vapor-phase DFP substrate hydrolysis on dyed enzyme-containing ISV117 membranes (cast from a 9% polymer solution) via fluorescence response. e) Enzyme-functionalized ISV119 material demonstrated a significant, reversible, and reproducible reduction in aqueous permeability in response to enzyme substrate, 3.62 μM paraoxon in 1 mL. f) The speed and magnitude of the membrane permeability response was directly related to the magnitude of the chemical challenge.

Transduction of enzyme-mediated substrate hydrolysis into a permeability response was evaluated by measurement of the pressure-driven water flux across membranes in aqueous solution at varying simulant concentration. Within one minute a reduction of liquid permeability

to about 1dB of the original value was observed, demonstrating the rapid self-regulating characteristics of enzyme-actuated membranes (Figure 4-12e). The rate and magnitude of response increased in correlation with simulant challenge (Figure 4-12f). Final membrane flux was equivalent to the simulated "closed" system (<pH 4.5). Since enzyme-based acid production is confined to the membrane surface, minimal impact on the bulk liquid pH was observed. Localization of enzymes within the ISV membrane minimizes the opposing effects of molecular diffusion to overcome local buffering and enable rapid material response. The permeability transition was stable and highly reproducible with negligible loss of enzyme activity or reduction in the level of material responsivity through several cycles of membrane reset (wash solution pH>5) and repeat agent exposure.

4.5 Conclusions

In conclusion, we have demonstrated a high fidelity, logic-gated "biomimetic" membrane system capable of localized, target selective, rapid modulation of permeability in response to chemical threat simulants. Material function is achieved by the integration of enzymatic recognition capability into pH-responsive asymmetric polymer ultrafiltration membranes with narrow pore size distribution. The mechanical and functional stability, as well as estimated economics of the new materials, are consistent with large-scale production requirements. The simplicity of the fabrication process and versatility of enzyme reactivity offers an intriguing outlook for future material technology facilitated by "biomimetic" membranes. Extension of the current approach to integrate multicomponent enzyme systems could be used to engineer and tailor the response of membranes to a complex range of external parameters, providing sensing, protection, and remediation capabilities.

Chapter 5: Effect of Polymer Graft Architecture on Solution Properties of Polymer-Conjugated Protein Systems

Reference: A manuscript on the work presented in the following chapter is in preparation for submission: R. Ferebee, I.F. Hakem, A. Koch, M. Chen, Y. Wu, D. Loh, D. Wilson, J. Poole, J. Walker, G. Fytas, and M.R. Bockstaller, "Effect of Polymer Graft Architecture on Solution Properties of Polymer-Conjugated Protein Systems."

5.1 Background and Motivation

The tethering of polymeric chains to proteins or enzymes has become ubiquitous in the design of protein-based material technologies. The most well known example is the grafting of poly(ethylene glycol) (PEG) to increase the efficacy of protein biopharmaceuticals. For example, PEGylation has been shown to decrease the rate of clearance of protein therapeutics from the liver and kidney (due to the increased size of the hydrodynamic diameter upon PEGylation) and thus to increase the *in vivo* circulation time of proteins [13,17,40,99–103]. PEGylation has also been shown to reduce self-aggregation and to widen the temperature range for the application of protein pharmaceutics by increasing the temperature required to unfold the protein and reduce activity [13,99,101]. Beyond pharmaceuticals, the combination of high catalytic efficacy along with target specificity has rendered polymer-conjugated proteins or enzymes as building blocks for the design of biomimetic materials with applications ranging from self-regulating membranes to detection and remediation [18]. Here, polymer conjugation is important to enable the integration of proteins within synthetic material hosts and to stabilize proteins against degradation in organic solvent environments.

A prerequisite to the effective application of polymer-conjugated proteins in therapeutics or functional materials is to understand the implications of polymer-conjugation on the structure and physico-chemical properties of protein-polymer conjugates. Two widely used models to describe the structure of PEGylated proteins: (1) The 'shroud model' that assumes the

'wrapping' of the polymer around the globular protein 'core' and (2) the 'dumbbell model' that corresponds to a 'mushroom-type' structure with polymer chains extending from the protein core [103–112]. The conditions favoring each type of structure remain subject of current research; however, recent results suggest that net-attractive polymer-protein interactions favor a 'shroud' state while steric repulsion along with small degree of polymerization of tethered chains appears to favor more 'dumbbell'-like structures. For example, Tilton and coworkers investigated the effect of polymer modification on the radius of gyration (R_G) of chicken-egg lysozyme and human growth hormone, each functionalized with a single 20kDa PEG chain, using small angle neutron scattering (SANS) and concluded a predominantly 'dumbbell' like structure in both cases [101]. Similar results were reported by Middelberg *et al.* on PEGylated human galectin-2 [17]. More recently, Longeville and coworkers systematically investigated the dependence of R_G on the degree of polymerization of polymeric ligands in the case of PEGylated hemoglobin [108,112]. For low molecular PEG grafts (with molecular weight M_{PEG} < 10kDa), a 'dumbbell'-type conformation was observed while high molecular PEG ligands (M_{PEG} > 20 kDa) gave rise to more compact ('shroud'-like) structures. A 'transition regime' was postulated to exist for intermediate molecular weights corresponding to mixed chain conformational characteristics.

Interestingly, the therapeutic efficacy of PEGylated proteins has been found to sensitively depend on the degree of polymerization of PEG ligands – this aspect has been the subject of a number of review articles and we refer the reader to Harris *et al.* for more information on this important subject [106]. While the detailed relationship between conjugation characteristics and biological efficacy is complex and depends (among others) on the details of the protein/PEG, solvent/protein, and solvent/PEG interactions as well as mechanistic aspects, a few trends can be delineated. For example, for a fixed polymer fraction (*i.e.* $\phi_{PEG} = m_{PEG}/(m_{PEG} + m_{prot})$ = constant,

with m_i denoting the mass of component i per polymer conjugate) the circulation half-life of PEGylated proteins is generally observed to increase with molecular weight of PEG tethers – this trend has been rationalized as a consequence of more effective 'masking' of the protein core in the case of high molecular PEG tethers. However, the complex parameter space that determines properties such as 'biological efficacy' of protein-polymer conjugates renders the quantitative interpretation of cause-effect relations difficult. It is the purpose of this study to contribute to the better understanding of the governing parameters that control interactions between PEGylated proteins in dilute aqueous solution. The motivation is twofold: First, although a 'dilute one-component solution' scenario presents a vast oversimplification of the situation under *in vivo* conditions, it is expected that fundamental physicochemical trends that are derived under dilute solution conditions, at least in part, transcend to more complex solution scenarios and hence should help inform the interpretation of observations in more complex systems. Second, the design of protein-based materials typically involves solution processing and hence insights into the relationship between the architecture of protein-PEG conjugates and their solution behavior could benefit the synthesis of improved material formulations with, for example, optimized protein content. The specific question we aim to address is: how does the distribution of PEG tethers affect the interaction between proteins in solution? Is it preferable to 'distribute' a given volume fraction of PEG among multiple short chain ligands as opposed to fewer long chain tethers to improve solubility?

Information about interactions between solutes in solution can be obtained by measurement of the second virial coefficient (A_2), a thermodynamic parameter that can be accessed by light or neutron scattering and that is related to the potential of mean force between two solutes in a dilute solution. The second virial coefficient has been widely used as a diagnostic tool to gauge

the stability of protein solutions since – according to McMillian-Meyer solution theory – positive values of A_2 indicate good solvent behavior (and hence increased solubility) while negative values indicate poor solvent quality and aggregation of solutes [113,114]. However, despite the valuable information provided by A_2 for interpreting the solution behavior of macromolecular systems, only few studies have reported quantitative relationships between the molecular characteristics of PEG ligands and the corresponding A_2 of protein-PEG conjugates in solution. For example, Middelberg *et al.* used SANS to evaluate A_2 of a mono-PEGylated human galectin-2 (with M_{PEG} = 30 kDa) in aqueous solution and found that the grafting of just one PEG chain results in a positive A_2 (6×10^{-4} mol mL/g^2) thus confirming the increased solubility of the mono-PEGylated protein [17]. However, to the authors' knowledge no systematic study has been conducted to assess the role of the number and degree of polymerization of PEG tethers on A_2 of protein-polymer conjugates in solution. The present study aims to close this gap (for the particular case of PEGylated Bovine Serum Albumin).

In general, the second virial coefficient of macromolecules in solution is routinely inferred from a Zimm-type analysis of the concentration dependence of the intensity of scattered light in dilute solution. However, several complicating factors render this 'classical' light scattering analysis challenging in the case of PEGylated protein systems. Most importantly, PEGylation reactions (such as the coupling of a form of 'activated PEG' to reactive sites on a protein) generally exhibit low reaction efficiencies that result in small numbers of tethered chains (typically between one to three). Although this is advantageous from an application perspective (since it allows for a higher protein content in the final PEGylated product) it implies that – because the A_2 of most proteins in aqueous solution is negative – the A_2 of PEGylated proteins with low molecular PEG tethers is also (often) weakly negative. This gives rise to the formation of

aggregates in solution that render the interpretation of the total scattered intensity difficult. Perhaps for this reason, a systematic analysis of the effect of chain length of PEG tethers on the A_2 of proteins in solution has remained elusive. To prevent distortions due to aggregate scattering and hence to enable the selective evaluation of A_2 of (individual dispersed) PEGylated proteins we present an experimental process that is based on the combined static *and* dynamic analysis of the scattered light. In a first step, dynamic light scatting is used to identify the distinct diffusive modes corresponding to dispersed and aggregated particles. Subsequently the scattering intensity contributed by dispersed PEGylated proteins is analyzed as a function of scattering angle and concentration by evaluation of the amplitudes corresponding to the respective mode. Independent evaluation of the (weight-averaged) molecular weight of protein-PEG conjugates by matrix-assisted laser desorption time of flight (MALDI-TOF) spectrometry allows the determination of A_2 using a Zimm-type analysis. Our results reveal that A_2 is a sensitive function of *both* the overall composition but also the distribution of PEG. In agreement with expectation, A_2 increases with the PEG volume fraction of conjugates; however, the effectiveness of PEG tethers to raise A_2 sensitively depends on the distribution of the polymer across the protein. At a given PEG volume fraction, A_2 significantly increases with the degree of polymerization of tethered chains (*i.e.* few 'long' chains are significantly more effective than a larger number of 'short' chains). Analysis of the hydrodynamic radii of protein-PEG conjugates reveals that the increased solubility is concurrent with a structural transition in the case of high molecular PEG grafts that results in a core-shell-type structure consistent with the 'shroud model'. Our results thus provide new insights into the link between architecture and the structure and solubility of protein-PEG conjugates that could benefit the interpretation of the biochemical characteristics of protein conjugates.

5.2 Sample Preparation

5.2.1 Materials

Bovine Serum Albumin (BSA, $M_w \approx 67$kDa) was purchased from Sigma Aldrich, and methoxy-PEG-succinimidyl carboxymethyl ester (mPEG-NHS) and methoxy-PEG (mPEG); M_w = 2kDa, 3kDa, 5kDa, 10kDa, and 30kDa were purchased from JenKem Technology USA. Phosphate buffered saline (PBS) was purchased from Sigma Aldrich (0.01M, pH 7.4, 0.0027 M KCl, 0.138 M NaCl). All materials were used as received.

5.2.2 Synthesis

For each molecular weight, synthesis was performed for different molar concentration ratios of mPEG-NHS:lysine residues to vary the number of PEG grafts on BSA. The solutions were stirred for 1 hour before 3 μL of 0.1 M HCl solution was added to end the reaction. The unreacted mPEG-NHS was filtered by dialysis using a 50 kDa membrane filter (Spectrum Labs Float-A-Lyzer) for 72 hours in DI water. Samples were subsequently lyophilized using a Labconco Cascade FreeZone Plus 2.5 Freeze-Dry System operated at -84 °C and 0.035 mBar. Ultraviolet – Visible Spectroscopy (UV-Vis) was performed to confirm the purity of the dialyzed and lyophilized product. Data was collected using a Cary 300 Scan UV-Vis Spectrophotometer at room temperature in absorption mode over the wavelength range of 200 – 300 nm using a quartz cuvette filled with dilute solutions of BSA-PEG conjugate samples in PBS. It was found that dialysis was an effective purification technique for conjugates.

5.3 Characterization Techniques

5.3.1 Matrix Assisted Laser Desorption/Ionization-Time of Flight (MALDI-TOF)

MALDI-TOF mass spectrometry was performed on an Applied Biosystems Voyager DE-STR mass spectrometer (mass range 1-400 000 Da) equipped with positive and negative ion modes, linear and reflector modes, and a nitrogen laser operating at λ = 337 nm. Ferulic acid and sinapinic acid were used as matrices in a water/acetonitrile mixture.

5.3.2 Static and Dynamic Light Scattering (SLS/DLS)

An ALV/LSE-5004 goniometer/correlator setup with a HeNe laser (λ = 633 nm) at 20 °C over the time range 10^{-7} to 10 s was used to measure the autocorrelation function $g_2(q,t)$

$$g_2(q,t) = \frac{\langle I(q,0)\, I(q,t)\rangle}{\langle |I(q,0)^2| \rangle} \tag{29}$$

of the light scattering intensity $I(q)$ at a scattering vector $q = 4\pi n\lambda^{-1}\sin(\theta/2)$ where n is the medium refractive index, λ is the vacuum wavelength of the incident light, and q is the scattering angle over the range 30° to 150°.

BSA-PEG samples were dissolved in PBS at a concentration of 10 g/L and were filtered through 0.22 μm Millipore filters into round quartz cells (outer diameter of 1 cm). Measurements were performed with vertical (VV) polarization. The Siegert relation is used to compute the normalized light scattering intensity autocorrelation function $g_2(q,t)$

$$g_2(q,t) = 1 + f^* |\alpha g_1(q,t)|^2 \tag{30}$$

where f^* is an experimental instrument factor relating the scattering area to the coherence area via a standard, and α is the fraction of total scattered intensity stemming from fluctuations with correlation times longer than 10^{-7} s.

The normalized field auto-correlation function of the scattered electric field is described by $E(q,t)$

$$g_1(q,t) = \frac{\langle E^*(q,0)\, E(q,t)\rangle}{\langle |E(q,0)^2| \rangle} \tag{31}$$

and can be related to the experimental correlation function, $C(q,t) = \alpha g_1(q,t)$. In a first step, regular cumulant analysis (assuming mono-modal behavior) is performed to qualitatively establish dispersity of samples. In a second step, the Kohlrausch-Williams-Watts (KWW) function $g_1(t) = P_0 + P_1 * e^{-\left[\frac{t}{\tau_1}\right]^{\beta_1}} + P_3 * e^{-\left[\frac{t}{\tau_2}\right]^{\beta_2}}$, where P_0 is the baseline, P_1 is amplitude of the fast process, τ_1 is the relaxation time of the fast process, β_1 is the fast process stretching exponent, P_3 is the amplitude of the slow process, τ_2 is the relaxation time of the slow process, and β_2 is the slow process stretching exponent, is used to establish characteristic relaxation times. For uniform systems, such as low M_w mPEG-NHS, agreement is found between the two types of analysis. Using the diffusion coefficient, $D_0 = \Gamma/q^2$, where Γ is the relaxation rate equal to $1/\tau$, the hydrodynamic radius can be determined using the Stokes-Einstein equation, $R_H = \frac{k_B T}{6\pi\eta_s D_0}$, where R_H is the hydrodynamic radius, k_B is the Boltzmann constant (1.38 x 10^{-23} m^2 kg s^{-2} K^{-1}), T is temperature, and η_s is the solvent viscosity.

Doubly distilled and filtered toluene was used as a standard to evaluate absolute scattering intensities. The absolute scattered intensities are given by the Rayleigh ratio: $R(q) = \left(I_{sample} - I_{solvent}\right) * \frac{R_{toluene}}{I_{toluene}} * \left[\frac{n_{solvent}}{n_{toluene}}\right]^2$ where n is the refractive index. The reduced Rayleigh ratio, $R(q)/(Kc)$ includes the concentration, c, and an optical constant, $K =$

$4\pi^2 n^2 \left(\frac{\delta n}{\delta c}\right)^2 (\lambda^4 N_A)^{-1}$, where n is the refractive index of the solvent, ($\delta n/\delta c$) is the refractive index increment of the sample, λ is the laser wavelength, and N_A is Avogadro's number (6.022 x 10^{23} mol^{-1}).

5.3.3 Optical Interferometry

The refractive indices of BSA, mPEG-NHS, and BSA-PEG conjugates in PBS were measured at concentrations of 1, 2.5, 5, 7.5, and 10 g/L using a Reichert AR7 Series automatic refractometer at 20°C after calibration with DI water. The recorded values were plotted against concentration, and the slope of the line was taken as the refractive index increment of the sample ($\delta n/\delta c$): BSA (0.1684 mL/g), mPEG-NHS2k (0.1246 mL/g), mPEG-NHS3k (0.1261 mL/g), mPEG-NHS5k (0.1216 mL/g), mPEG-NHS10k (0.1216 mL/g), mPEG-NHS30k (0.1293 mL/g), BSA-PEG2k (0.1647 mL/g), BSA-PEG3k (0.1799 mL/g), BSA-PEG5k-1 (0.1569 mL/g), BSA-PEG5k-2 (0.1569 mL/g), BSA-PEG10k-1 (0.1285 mL/g), BSA-PEG10k-2 (0.1216 mL/g), BSA-PEG30k (0.1454 mL/g).

5.3.4 Transmission Electron Microscopy (TEM)

Observation of conjugate dispersion was performed using a JEOL 2000 EX electron microscope operated at 200 kV. Imaging was done by amplitude and phase contrast, and images were acquired using a Gatan Orius SC600 high-resolution camera. Samples were drop cast onto a carbon coated copper grid and stained for 5 min with RuO_4 to increase the contrast between the BSA and the PEG grafts.

5.3.5 Circular Dichroism (CD)

CD was performed using a Jasco J-810 CD Spectropolarimeter in the far-UV region (200-260 nm) at 20°C using a 1 mm path length cell. Five scans were averaged to create each spectrum, and the scans were collected at a speed of 50 nm/min and a bandwidth of 1 nm. The samples were dissolved in PBS at a concentration of 0.8 mg/mL.

5.4 Evaluation of Graft Characteristics

5.4.1 Synthesis

The material system in our study is based on non-specific PEGylated Bovine Serum Albumin (BSA-PEG), a model system that has been widely studied, for example, to establish the role of PEGylation on the structure, thermal, and solution stability of protein-PEG conjugates. The second virial coefficient of BSA in 0.05 M potassium phosphate, pH = 6.2 buffer solution has been reported to be weakly negative ($A_2 = -2 \times 10^{-4}$ mL mol/g^2), see discussion in *2.2.1 Solution Behavior of Polymer-Conjugated Proteins*, while positive values ($A_2 \sim 10^{-3}$ mL mol/g^2, with some variation of values depending on the molecular weight and end groups of the polymer) are reported for pristine PEG consistent with its good solubility in aqueous solution [36–39]. PEGylated samples of BSA were synthesized using an NHS-coupling reaction at room temperature in a PBS (0.01M, pH 7.4, 0.0027 M KCl, 0.138 M NaCl) solution, with five molecular weights of mPEG-NHS (2, 3, 5, 10, and 30 kDa) following procedures found in the literature (see *5.2.2 Synthesis* for more details) [79]. A reaction scheme for the PEGylation of BSA is shown in Figure 5-1.

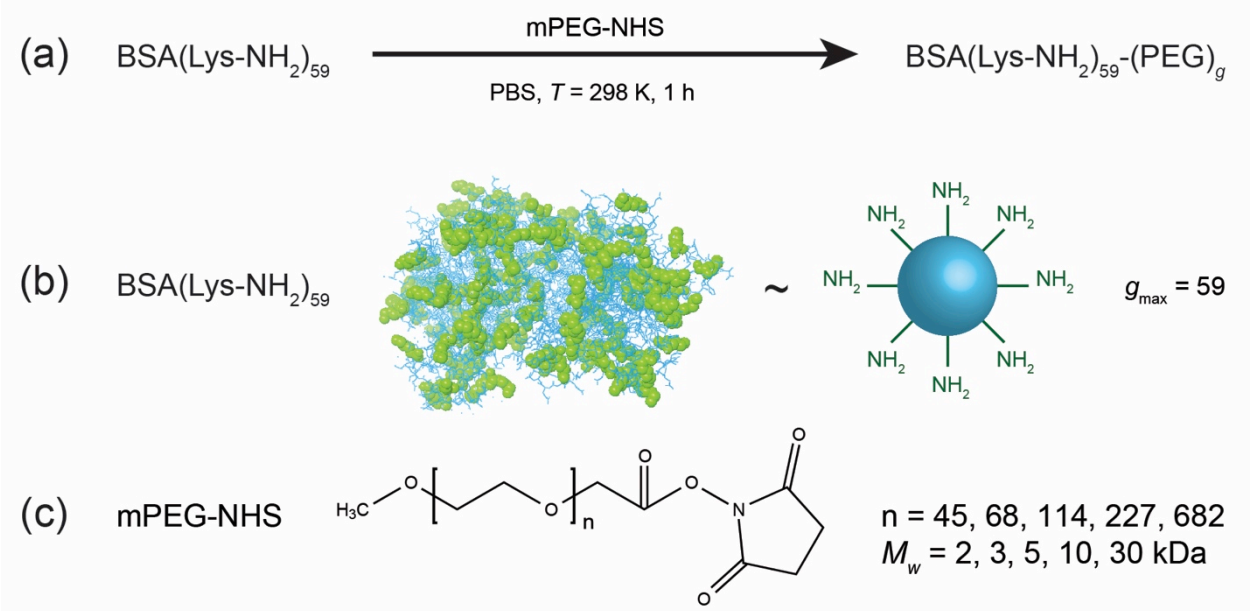

Figure 5-1. (a) Reaction scheme for polymer functionalization of Bovine Serum Albumin (BSA, M_w ~ 67kDa) with mPEG-NHS (M_w ~ 2kDa, 3kDa, 5kDa, 10kDa, and 30kDa). (b) Illustration of the globular protein BSA with its 59 lysines highlighted in green. (c) Chemical structure of methoxy-poly(ethylene glycol)-succinimidyl carboxymethyl ester (mPEG-NHS).

Upon mixing, the mPEG-NHS reacts immediately with the NH_2 groups that are part of the lysines in the BSA amino acid sequence. The NHS group is capped with a hydrogen, leaving the mPEG conjugated to the BSA, as shown in Figure 5-2.

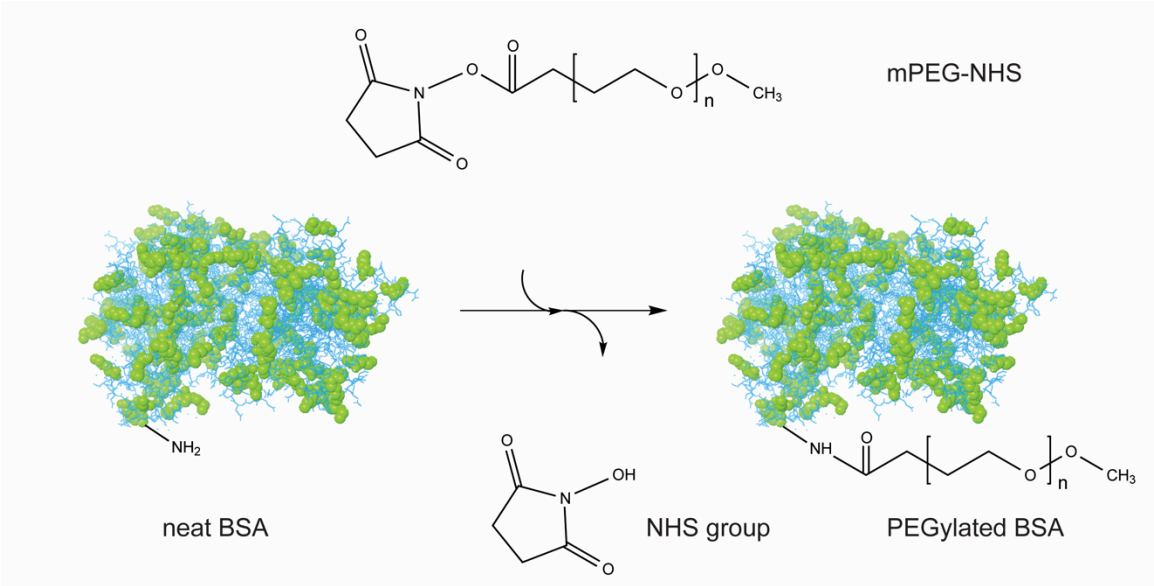

Figure 5-2. PEGylation schematic of mPEG-NHS and BSA depicting the coupling of PEG with the lysine residues (highlighted in green).

Synthesis conditions were varied to determine the optimal reaction time and PEG:lysine residue ratio. BSA was conjugated with PEG of M_w = 2kDa (abbreviated BSA-PEG2k) in separate reactions with reaction times of 5 min, 1 hr, and 24 hr. Mass spectrometry determined that there was no significant change in the reaction efficiency and grafting characteristics with shorter or longer reaction times, as shown in Figure 5-3, so all future conjugations were performed for 1 hr. BSA-PEG5k samples were conjugated with varied PEG:lysine residue ratios, including 0.25:1, 0.57:1, 0.75:1, 1:1, and 10:1. Optimal conjugation (maximum average number of PEG grafts) occurred in the case of the 0.57:1 PEG:lysine residue ratio, as shown by the shift toward increased mass of the 0.57:1 PEG: lysine residue ratio spectrum in Figure 5-3. Literature agrees with this result and suggests that large molar concentration ratios lead to the grafting of few PEG chains due to steric hindrance and crowding of the activated PEG in solution [79]. The optimal molar concentration ratio varies for different proteins due to the difference in size and number of lysines available for PEGylation. Based on the results from the BSA-PEG5k system, all other samples were synthesized with a ratio of 0.57:1 and 10:1, except in some cases due to limitations of materials.

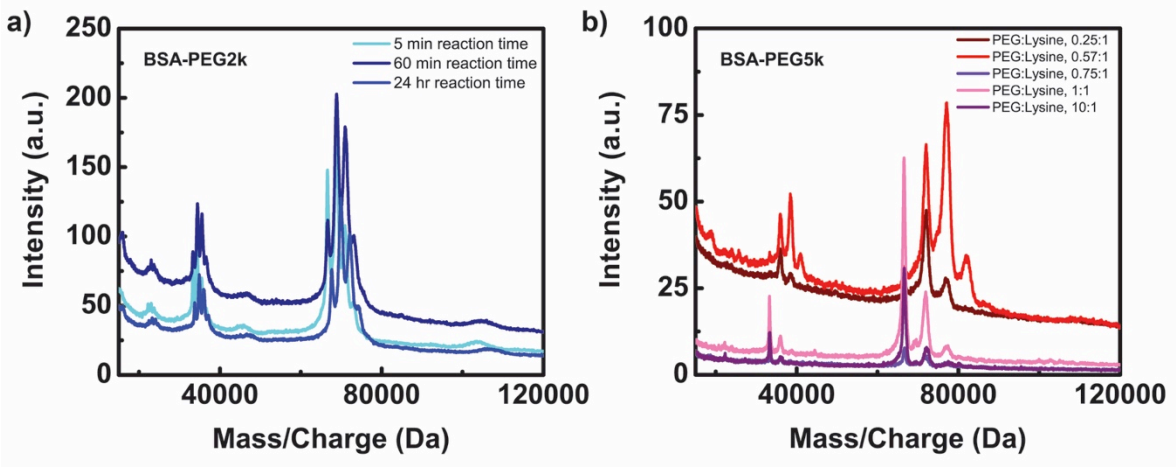

Figure 5-3. (a) MALDI-TOF spectra of BSA-PEG2k samples conjugated with reaction times of 5 min, 1 hr, and 24 hr. (b) MALDI-TOF spectra of BSA-PEG5k samples reacted for 1 hr with molar concentration ratios of 0.25:1, 0.57:1, 0.75:1, 1:1, and 10:1.

5.4.2 Characterization of Compositional Heterogeneity

To determine the molecular composition and degree of PEGylation of reaction products, all samples were dialyzed to remove unreacted mPEG-NHS and subsequently characterized by MALDI-TOF. Instrument calibration and spectra collection was performed according to previously published procedures [13,49]. It is important to note that polymer conjugation reactions of proteins generally result in heterogeneous products (*i.e.* in products that are composed of a mixture of proteins conjugated with a distinct number of tethers) and hence the molecular weight and composition of PEGylation products are characterized by the respective average values [48,49]. To determine the average number of PEG tethers per BSA, the MALDI spectra were fit to the distribution function P(g) that has been shown to describe the statistical distribution of the number of ligands, g, in polymer conjugation reactions.

$$P(g) = \frac{g_{max}!\,\varepsilon^{g}(1-\varepsilon)^{(g_{max}-g)}}{g!\,(g_{max}-g)!} \tag{32}$$

Here, g_{max} denotes the maximum number of possible binding sites (assumed to be equal to the number of available lysines, *i.e.* g_{max} = 59), ε = $\langle g \rangle / g_{max}$ is the reaction efficacy, and $\langle g \rangle$ is the average number of PEG ligands. Note that for a given protein system eq. 32 is a one-parameter equation with ε being the only adjustable parameter. Good agreement between experimental and theoretical distributions was observed for all PEGylated products. Figure 5-4 depicts representative MALDI spectra for BSA and the PEGylated product (M_{PEG} = 10 kDa) as well as the corresponding fit of P(g) to the experimental peak amplitudes. Also shown is a representative TEM image of sample BSA-PEG10k-2 (stained with ruthenium tetroxide). The uniform separation distance of approximately 0.8 nm between adjacent BSA that can be discerned from the micrograph supports the uniform modification of BSA.

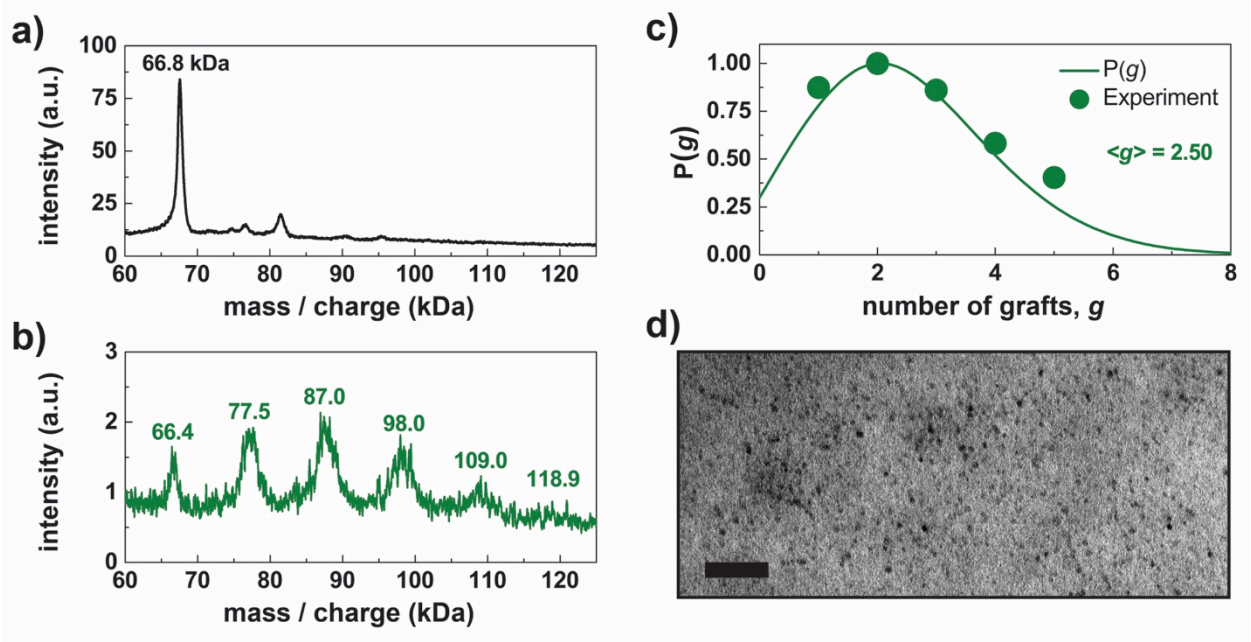

Figure 5-4. (a) MALDI-TOF spectrum for neat BSA (b) MALDI-TOF spectrum for BSA-PEG10k-2 with the mass of each peak labeled (c) Fit of the ligand distribution function P(g) to MALDI data for BSA-PEG10k-2 revealing an average number of grafts equal to 2.5 (d) Bright-field TEM image of BSA-PEG10k-2 (ruthenium tetroxide stain). BSA appears as 'black dots' of about 2.3 nm radius. The scale bar is equal to 50 nm.

From the respective ligand distribution functions P(g), the number (M_n) and weight average (M_w) molecular weight of BSA-PEG conjugates follow as

$$M_n = M_{BSA} + \langle g \rangle M_{PEG} \tag{33a}$$

$$M_w = \frac{M_{BSA}^2 + 2M_{BSA}M_{PEG}\langle g \rangle + M_{PEG}^2\langle g^2 \rangle}{M_{BSA} + \langle g \rangle M_{PEG}} \tag{33b}$$

where the average number of PEG ligands is $\langle g \rangle = \int gP(g)\,dg$ (since P(g) is normalized). Table 5-1 summarizes the molecular characteristics of all BSA-PEG systems that are the subjects of the present study along with the respective sample ID.

Table 5-1. Summary of molecular characteristics and composition of BSA-PEG systems.[1]

Sample ID	<*g*>	Φ_{PEG} (vol. %)	f_{PEG} (wt. %)	M_W (Da)
BSA-PEG2k	1.1	0.04	0.03	69165
BSA-PEG3k	1.2	0.06	0.05	70394
BSA-PEG5k-1	1.3	0.11	0.09	73892
BSA-PEG5k-2	2.3	0.17	0.14	78743
BSA-PEG10k-1	0.8	0.13	0.11	76190
BSA-PEG10k-2	2.5	0.31	0.27	94408
BSA-PEG30k	0.8	0.31	0.27	99732

The table reveals that the average number of PEG ligands varies between 1 and 2.5, which is consistent with previously reported results for NHS-based coupling reactions. Sample compositions were chosen to selectively test the role of molecular weight and number of ligands as well as the overall fraction PEG. In particular, sample series BSA-PEG2k/3k/5k-1/10k-1/30k selectively tests the role of chain length on (approximately) mono-PEGylated BSA. In contrast, sample pairs BSA-PEG5k-1/10k-1 as well as BSA-PEG10k-2/30k evaluate the role of distribution of PEG segments at approximately constant overall composition BSA:PEG, respectively.

[1] For the relation between weight (f_{PEG}) and volume (ϕ_{PEG}) fraction of PEG the densities of PEG and BSA were assumed to be ρ_{PEG} = 1.125 g/cm^3 and ρ_{BSA} = 1.35 g/cm^3, respectively [116,127].

5.5 Determination of A_2 using Light Scattering

5.5.1 Photon Correlation Spectroscopy

The effect of PEG-ligand architecture on the solution characteristics of BSA-PEG conjugates in PBS solution was established by static and dynamic light scattering. The combination of static *and* dynamic light scattering was found to be of paramount importance for the characterization of PEGylated BSA because in samples with low molecular PEG ligands, a small but non-negligible degree of aggregate formation was observed that could not be removed regardless of sample preparation. We hypothesize that aggregate formation is caused by a small amounts of residual mPEG-NHS that might be retained even after three days of sample dialysis. The distinctively negative A_2 of mPEG-NHS in PBS solution (see discussion below) is expected to drive formation of aggregates. Because the intensity of scattered light depends on the square of the volume of scatterers ($I_s \sim V^2$) even a small volume fraction of aggregates can significantly add to the total intensity of the scattered light and hence impede the interpretation of data in classical static light scattering. Dynamic light scattering was thus used to decompose the scattering contributions due to individual PEGylated BSA as well as aggregates and to enable the select analysis of the scattering of individual BSA-PEG. The process is illustrated in the following for the particular example of BSA-PEG10k-2. Figure 5-5 depicts a representative field autocorrelation function $g_1(t)$ of a c = 10 g/L solution of BSA-PEG10k-2 measured at $q = 1.87\times10^{-2}$ nm^{-1} corresponding to a scattering angle of 90°.

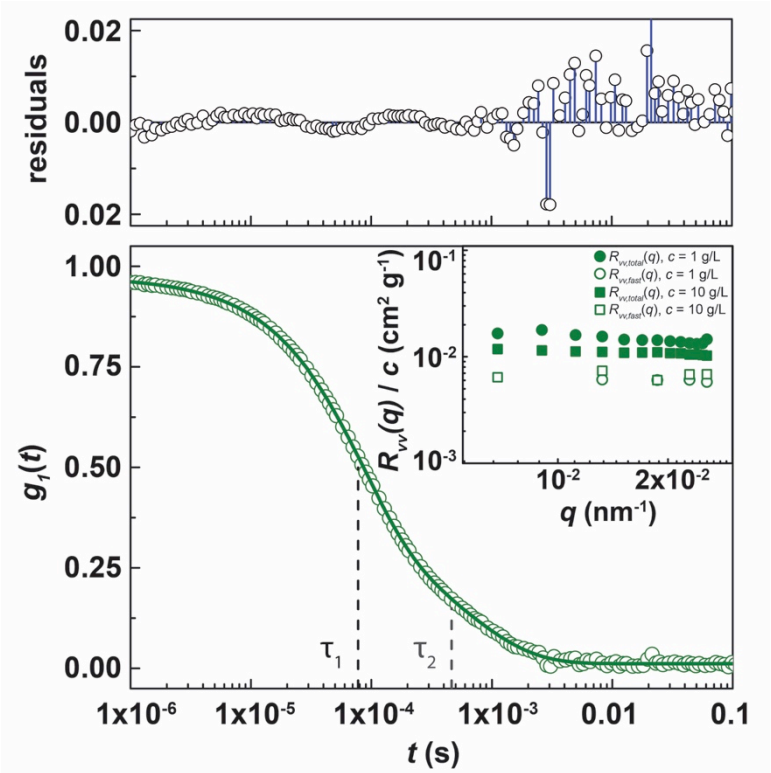

Figure 5-5. Field auto-correlation function of BSA-PEG10k-2 recorded at $q = 1.87\text{x}10^{-2}$ nm^{-1}. The relaxation times of the fast component (BSA-PEG) and the slow component (aggregates and impurities) are marked with vertical dashed lines. Inset shows total scattered intensity ($R(q)$, filled markers) and the fast component ($R_{fast}(q)$, open markers) of the scattered intensity normalized by concentration vs. q for BSA-PEG10k-2 at concentrations of 1 g/L (circles) and 10 g/L (squares). The fast component of the scattered intensity displays q-independence. Residuals are plotted on the same x-axis to show goodness of fit.

Cumulant analysis of $g_1(t)$ reveals the presence of a broad relaxation process that cannot be adequately represented as unimodal relaxation (as discerned from the systematic deviation of the residuals of the cumulant fit, not shown here). In contrast, KWW analysis provides an excellent fit (with random variation of residuals, see inset in Figure 5-5) to the experimental data assuming two distinct relaxation modes at $\tau_1 = 7.88\text{x}10^{-5}$ s and $\tau_2 = 4.23\text{x}10^{-4}$ s, respectively, that can be attributed to diffusive processes by establishing the relationship $\tau^{-1} \sim q^2$ (result not shown). Evaluation of the hydrodynamic radius using Stokes-Einstein relation $R_H = k_B T/(6\pi\eta D_0)$, where k_B denotes the Boltzmann constant, $T = 298$ K, $\eta = 1.3341$ the viscosity of PBS, and D_0 the self diffusion coefficient (determined by extrapolation of $D = \tau^{-1}q^{-2}$ to infinite dilution), yields $R_H \sim$ 5.3 nm for the fast mode, consistent with the expected hydrodynamic size for of PEGylated BSA.

The contribution of the fast mode to the total scattering intensity $R(q)$ can be determined from the relaxation time distribution $H(\ln \tau)$ using

$$R_{\text{fast}}(q) = \int_{\ln \tau_{\min}}^{\ln \tau_{\max}} H(\ln \tau)\, \mathrm{d}(\ln \tau) \tag{34}$$

Where $\tau_{\min}$ and $\tau_{\max}$ correspond to the minimum and maximum relaxation time associated with the fast mode. Eq. 34 can be evaluated by standard methods of autocorrelation function analysis (such as CONTIN or using the Kohlrausch-Williams-Watts function, see *5.3.2 Static and Dynamic Light Scattering*). $R_{\text{fast}}(q)$ is subsequently interpreted using a Zimm-type analysis. Because of the significant efforts involved with the decomposition of scattering contributions of fast and slow modes, the analysis was performed for only a limited set of scattering angles, *i.e.* θ = 30°, 60°, 90°, 120°, and 150° (corresponding to q_1 = 0.0068 nm^{-1}, q_2 = 0.0132 nm^{-1}, to q_3 = 0.0187 nm^{-1}, q_4 = 0.0229 nm^{-1}, q_5 = 0.0256 nm^{-1}). The results of the analysis for BSA-PEG10k-2 are depicted in the inset of Figure 5-5. Several pertinent features are noted: first, $R_{\text{fast}}(q)$ is observed to be q-independent in contrast to the total scattering intensity $R(q)$ that shows clearly discernible angle dependence. Analysis shows that the latter is caused by the angle dependence of the scattering contribution of the slow mode $R_{\text{slow}}(q)$. This highlights the relevance of decomposing the scattering contributions of fast and slow modes that otherwise result in misinterpretation of the scattering characteristics of protein conjugates. We note that the independence of $R_{\text{fast}}(q)$ on the scattering angle is consistent with the small size of scattering centers that remains well below the limit of $R_G/\lambda < 1/20$ (where R_G denotes the radius of gyration) that – for weakly scattering systems – is associated with the Rayleigh scattering regime [115]. In the following we will therefore make the assumption of Rayleigh scattering to interpret the light scattering of conjugated BSA in a PBS solution.

Under the assumption of Rayleigh scattering, the effective refractive index increment of PEGylated BSA systems can be determined using optical interferometry (see *5.3.3 Optical Interferometry* for a list of the respective ($\delta n/\delta c$) values that were determined for the different PEGylated samples). Measurement of the refractive index increment allows calculation of the optical constant $K = (2\pi n(\delta n/\delta c))^2(N_{Av}\lambda^4)^{-1}$ from which the second virial coefficient can subsequently be determined using Zimm's relation

$$\frac{R_{fast}}{Kc} = \left[\frac{1}{M_w} + 2A_2c\right]^{-1} \tag{35}$$

Where R_{fast} is the angle averaged Rayleigh ratio of the fast mode and M_w represents the weight-averaged molecular weight of BSA-PEG conjugates.[2]

Using the values for M_w from MALDI-TOF and eq. 33b, the second virial coefficient can be determined for each polymer conjugate system. Following this procedure, the second virial coefficients of all BSA-PEG systems were determined for a reference concentration of 10 g/L. The latter was chosen as a practical compromise between the requirement of sufficient dilution such that only two-body interactions are expected to be relevant (this condition is assumed to be fulfilled in the present case since the average distance between particles in solution $(V/N_p)^{1/3} = (VM_{BSA\text{-}PEG}/m_{BSA\text{-}PEG}N_p)^{1/3} >> R_H$ for all BSA-PEG systems) as well as sufficient signal-to-noise ratio to allow for unambiguous analysis of autocorrelation functions.[3]

---

[2] In the application of eq. 35 we make use of the assumption $\langle(\delta n/\delta c)^2\rangle = \langle(\delta n/\delta c)\rangle^2$ since a finite dispersity of the PEGylated products has to be considered. This approximation can be shown to be valid in the limit of narrow-disperse systems as well as similar values of ($\delta n/\delta c$) of the respective components (here PEG and BSA). In the present case the error introduced by this approximation is estimated to be less than 10%.

[3] We note that in the classical Zimm analysis of the (time-averaged) total intensity of the scattered light an extrapolation to infinite dilution $c \rightarrow 0$ is performed. In contrast, the approach presented here rests on the decomposition of the scattering intensity by analysis of autocorrelation functions. The accuracy of this method sensitively depends on the quality of autocorrelation functions and in particular the absence of parasitic scatterers such as dust – the latter depends in practice on the ability to clean solutions (difficult for aqueous systems!) as well as the signal-to-noise ratio that defines the minimum duration of data accumulation. In the present case a concentration of 10 g/L was found to be a 'lower concentration limit' to enable the practical collection of high quality autocorrelation data.

Figure 5-6 summarizes the respective values of $A_{2,app}$ for all PEGylated BSA as well as pristine BSA and PEG systems that were determined in 0.01M PBS solution (where $A_{2,app}$ represents the 'apparent second virial coefficient' corresponding to a concentration of c = 10 g/L).

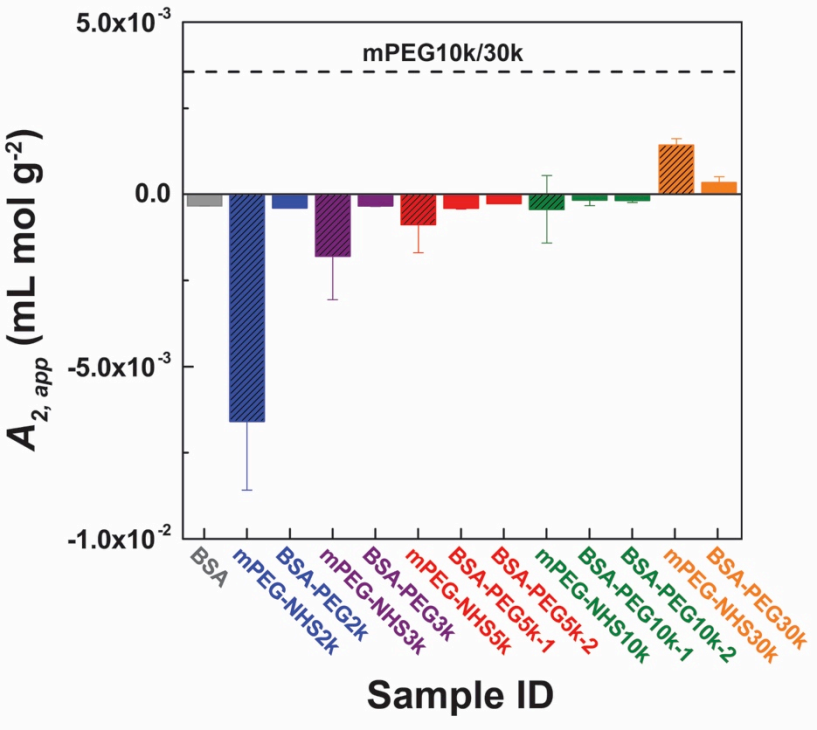

Figure 5-6. Second virial coefficient ($A_{2,app}$) data plotted for BSA, mPEG-NHS, and BSA-PEG conjugates (bar graphs color coded by PEG M_w and organized by increasing PEG M_w) and averaged mPEG (dashed line).

Several pertinent features can be discerned from Figure 5-6: first, $A_{2,app}$ for pristine BSA is found to be -3.2x10^{-4} mL mol/g^2, in good agreement with previously reported values. Second, pristine mPEG-NHS exhibits distinctively negative values of $A_{2,app}$ (with the exception of the 30kDa system for which a weakly positive value is obtained) indicating poor solubility in 0.01M PBS solution. This surprising finding is in contrast to the behavior of 'regular PEG' for which good solubility in aqueous solution is expected. Indeed, reference solutions (c = 10 g/L in 0.01M PBS) of M_w = 10 kDa and 30 kDa methoxy-terminated PEG show a consistent value of $A_{2,app}$ = 3.6×10^{-}

^{3} mL mol g^{-2} (see dashed gray line in Figure 5-6 and correlation curve in Figure 5-7). Therefore, we rationalize the negative $A_{2,app}$ in case of mPEG-NHS as a consequence of the NHS end-group that becomes increasingly influential with decreasing molecular weight (hence the decrease of $A_{2,app}$ with decreasing M_w of the respective mPEG-NHS). Figure 5-6 furthermore reveals that with the exception of BSA-PEG30k all conjugate systems exhibit a weakly negative $A_{2,app}$.

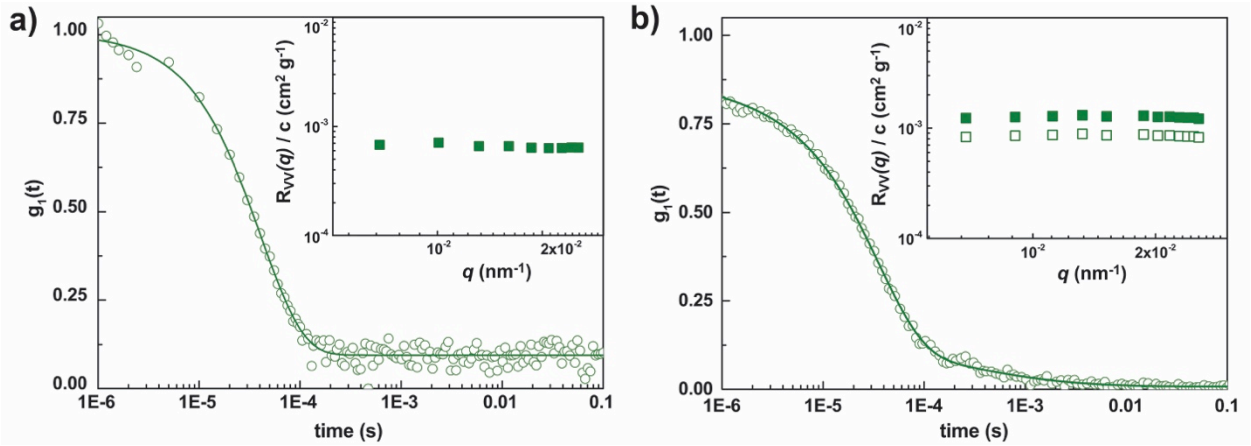

Figure 5-7. (a) Correlation curve of mPEG10k in PBS (10 g/L) recorded at an angle of 90° with (inset) total scattering intensity plotted as a function of q. (b) Correlation curve of mPEG-NHS10k in DI water (10 g/L) recorded at an angle of 90° with (inset) total scattering intensity (filled squares) and fast component scattering intensity (open squares) plotted as a function of q.

The $A_{2,app}$ values for mPEG-NHS10k in PBS, mPEG-NHS10k in DI water, and mPEG10k in PBS are plotted in Figure 5-8. mPEG10k in PBS without the NHS end group has an $A_{2,app}$ value closest to the literature value of PEG in water.

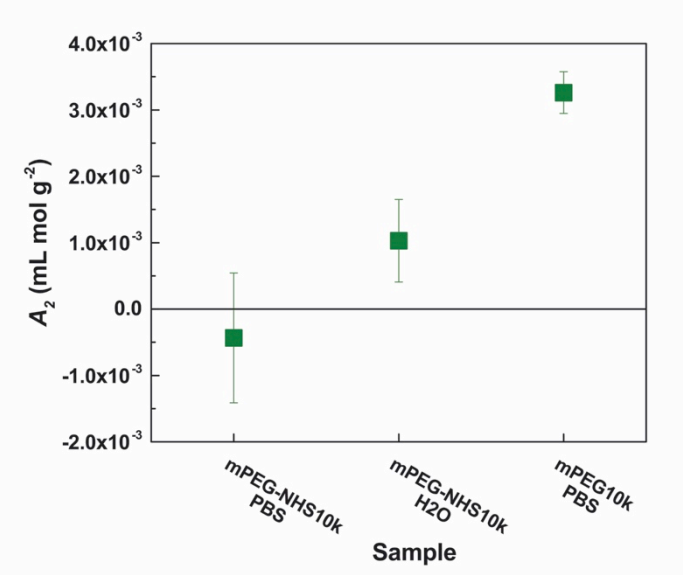

Figure 5-8. $A_{2,app}$ values for mPEG-NHS10k in PBS, mPEG-NHS10k in DI water, and mPEG10k in PBS. The NHS end group has an effect on the $A_{2,app}$ values, bringing them below the values reported in literature.

To better delineate the select influence of composition and distribution of PEG segments on the interaction between BSA-PEG systems in solution, Figure 5-9 depicts the dependence of $A_{2,app}$ on the composition (Fig. 5-9a) and molecular weight of PEG ligands (Fig. 5-9b), respectively.

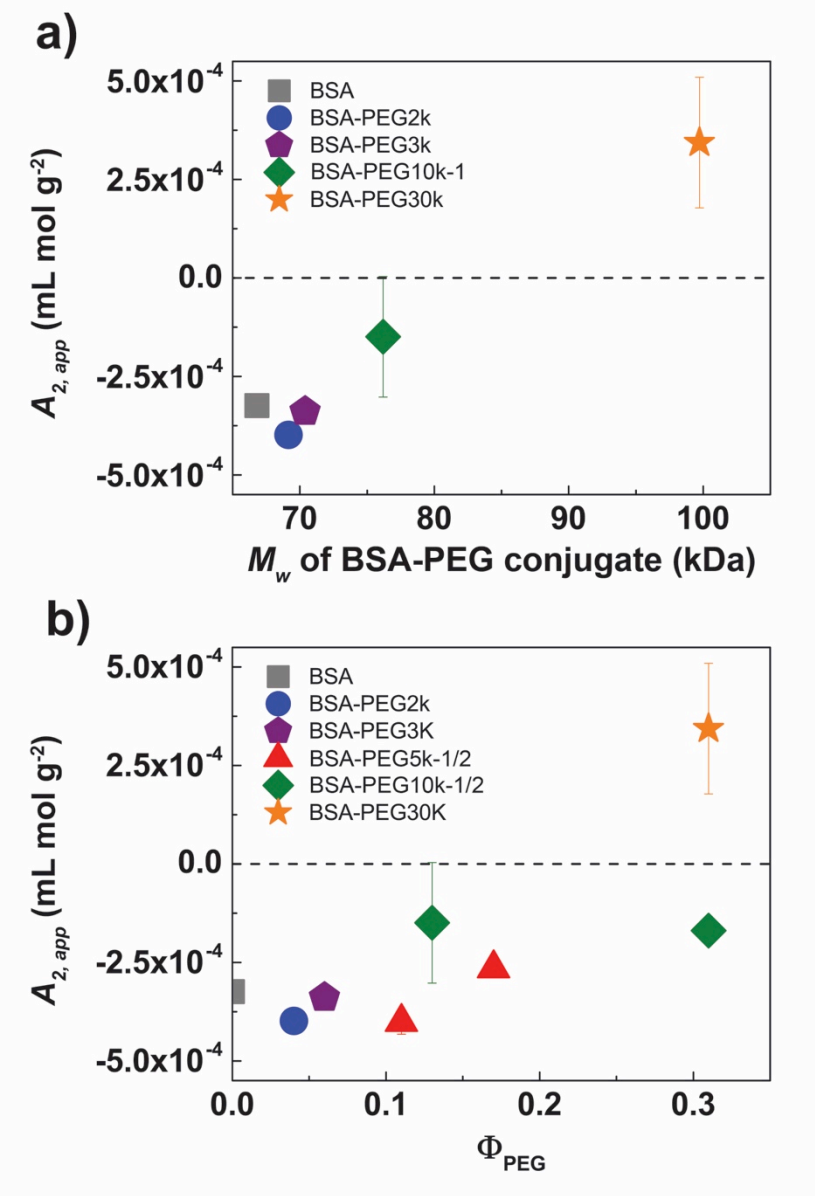

Figure 5-9. Second virial coefficient ($A_{2,app}$) plotted for BSA-PEG conjugates as a function of (a) the conjugate molecular weight for samples where $\langle g \rangle \sim 1$ and (b) the volume percent conjugated PEG.

Figure 5-9a reveals that for mono-functionalized BSA, $A_{2,app}$ increases with the degree of polymerization of PEG-ligands, ultimately assuming positive values for high molecular weight (M_w = 30 kDa) PEG ligands. This is consistent with expectations given the increasing number of favorable solute-solvent interactions that are contributed by the increased number of PEG segments (here we note that the end-functionality of PEG tethers is constituted by the methoxy-group while the NHS group is removed during the coupling reaction). However, closer

inspection of the depicted trend of $A_{2,app}$ on the composition of BSA-PEG conjugates reveals a more subtle dependence of solution interactions on the architecture of conjugate systems. In particular, Figure 5-9b reveals that – at constant overall BSA:PEG ratio – the increase of $A_{2,app}$ is more pronounced for mono-PEGylated systems as compared to double-PEGylated analogs (compare BSA-PEG5k-2/10k-1 and BSA-PEG10k-2/30k sample pairs in Fig. 5-9b). To confirm that the observed trend was due to the effect of PEG ligand only rather than related to unfolding transitions of BSA, circular dichroism (CD) spectroscopy was performed on all BSA-PEG systems in solution. The excellent agreement between the CD spectra of all BSA-PEG systems, as presented in Figure 5-10, supports that the tertiary structure of BSA is indeed retained during the PEGylation and dissolution/measurement process.

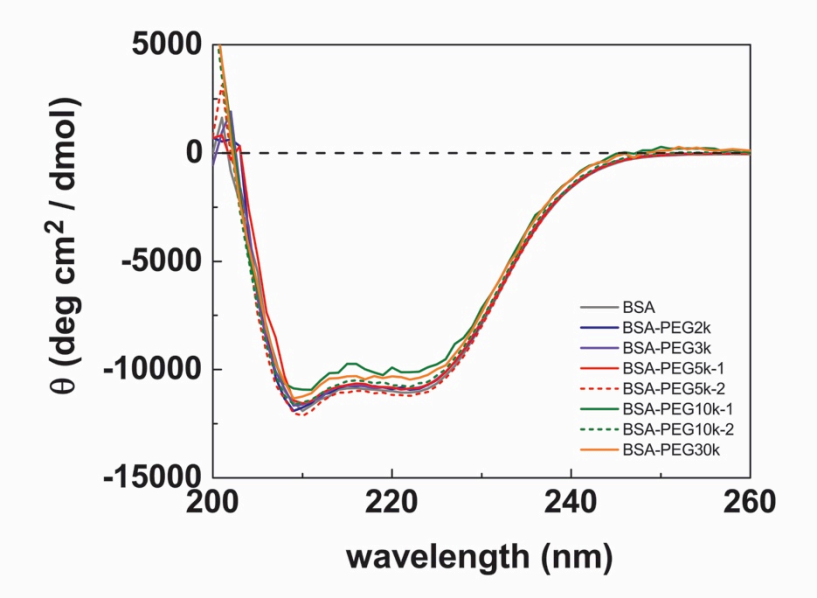

Figure 5-10. Circular dichroism (CD) spectra for BSA-PEG conjugates and unmodified BSA in PBS, indicating that BSA has not unfolded in response to the PEGylation process.

The trend shown in Figure 5-9 suggests longer chains are found to be more effective in solubilizing BSA as compared to a correspondingly larger number of shorter chains. This result should be of significance, for example, in the context of designing protein-based functional

materials with tailored compatibility and maximized protein content. It also presents an interesting analogy to the improved *in-vivo* stability of long-chain tethered proteins that has been widely reported in the literature [103]. While the latter is commonly attributed to the a reduction of the renal sieving efficacy with increasing hydrodynamic size of protein-PEG conjugates, the increased solubility (indicated by the increase of $A_{2,app}$ in case of higher molecular PEG tethers) could also be of relevance to explain the observed behavior.

An intriguing question is whether the observed effect of ligand chain length on the solution characteristics is related to structural changes in BSA-PEG conjugates. As elaborated above, previous (neutron scattering) studies on PEGylated proteins in a variety of aqueous solutions indicate a change of the ligand conformation from an extended state (the 'dumbbell model') to the formation of a dense shell through the wrapping of the ligand around the globular protein core ('shroud model'). To elucidate the role of structural transitions in the BSA-PEG systems that are subject to this study, the hydrodynamic size was evaluated against the predicted trends corresponding to extended and 'wrapped' chain conformations. To estimate the respective trends, the hydrodynamic radius of 'limiting configurations' was calculated on the basis of 'effective hydrodynamic shapes.' To represent a 'shroud case' with 'wrapped' conformation of tethered chains, a concentric 'core-shell' structure consisting of a dense BSA-core and PEG-shell was assumed to represent the diffusive characteristics of the BSA-PEG conjugate. The hydrodynamic radius of the core-shell sphere was then taken as the total radius that was calculated under the assumption of density of $\rho_{PEG} = 1.125$ g/cm^3 [116]. To estimate the effective hydrodynamic size in the case of extended chain conformations for mono-PEGylated BSA ('dumbbell case'), an effective ellipsoid of revolution was constructed with long and short axes equal to $a = R_{H,BSA} + R_{H,PEG}$ and $b = \max(R_{H,BSA}, R_{H,PEG})$ where $R_{H,i}$ is the hydrodynamic radius

of component *i* (measured by DLS); max($R_{H,BSA}$, $R_{H,PEG}$) is the greater of the respective hydrodynamic values. The effective hydrodynamic radius of a respective ellipsoid of revolution is subsequently calculated using the Stokes-Einstein relation (see discussion above), where the self-diffusion coefficient of the ellipsoid is given by Perrin's equation

$$D = \frac{KT}{6\pi\eta R} \frac{\left(\frac{b}{a}\right)^{2/3} \ln\left[\frac{1+\sqrt{1-(b/a)^2}}{b/a}\right]}{\sqrt{\left[1-\frac{b}{a}^2\right]}} \tag{36}$$

where η = 1.3341 is the solution viscosity of 0.01M PBS [117,118]. From eq. 36 the hydrodynamic radius can be determined using Stokes Einstein equation (see above). The process of determining the effective hydrodynamic size of 'shroud' and 'dumbbell' states is illustrated in Figure 5-11.

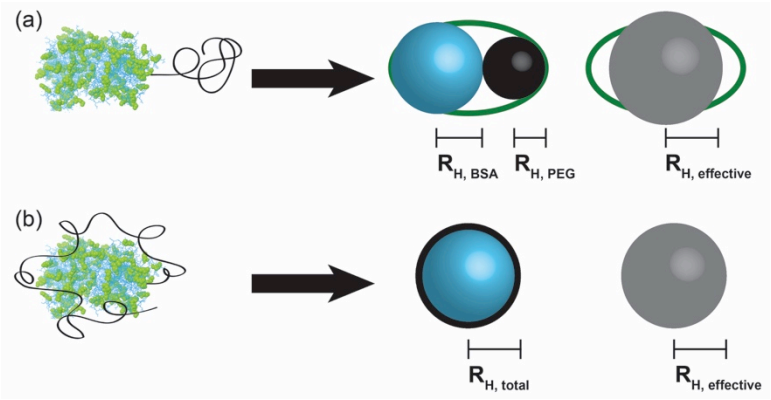

Figure 5-11. Schematic representations of BSA conjugated with one PEG graft and the resulting R_H for (a) the 'dumbbell' conformation and (b) the 'shroud' conformation.

Figure 5-12 presents a comparison of the trend of experimental hydrodynamic radii of the mono-PEGylated PEG-BSA systems with those of the respective 'reference shapes' corresponding to the 'shroud' and 'dumbbell' model.

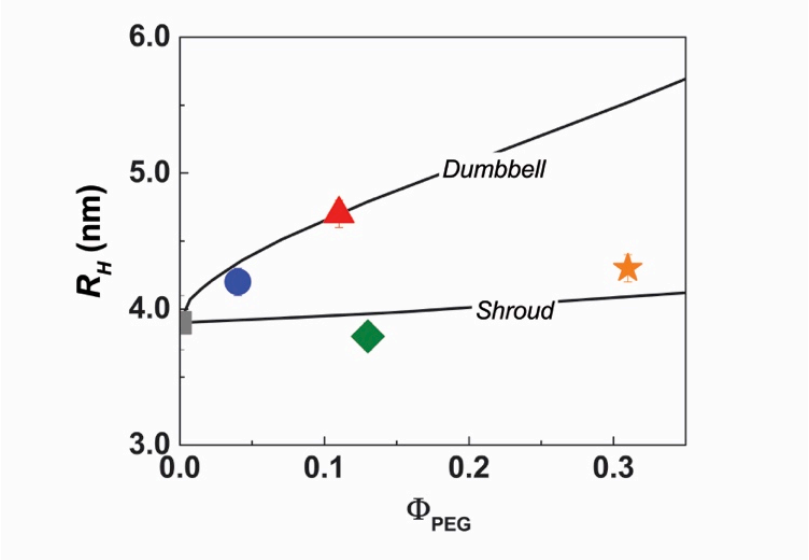

Figure 5-12. Plot of R_H as a function of volume fraction PEG for mono-PEGylated BSA-PEG samples. Low M_w grafted samples take on a 'dumbbell' conformation, while high M_w samples take on a 'shroud' conformation, with the transition occurring for samples with 10kDa for the graft M_w.

The figure reveals a remarkable agreement between calculated and experimental values and suggests a gradual transition from the 'dumbbell' to the 'shroud' state with increasing molecular weight of the tethered PEG. The observed conformational transition is in qualitative agreement with previous reports by Longeville *et al.* who concluded (on the basis of neutron scattering analysis of hemoglobin-PEG conjugates) that low molecular grafts (under 10kDa) adopt 'dumbbell' conformations while high molecular grafts (well above 10kDa) tend to form more compact, 'shroud'-like structures. Our results therefore suggest that rather than the total number of PEG segments in protein-PEG conjugates, it is the structure assumed by the polymeric tethers that determines the net effect of polymer-conjugation on the solubility of proteins. The sensitivity to structure rather than composition should be an important consideration in the design of protein-conjugates for functional material or pharmaceutical applications. It could also provide a basis for the interpretation of previous reports that have found the effectiveness of PEG-ligands to stabilize proteins under *in-vivo* conditions to depend on the configuration of chains (such as linear *vs.* branched) [106,119]. The methods presented in this work should be

equally applicable to the analysis of the solution properties of these more complex chain architectures.

5.6 Conclusions

We have evaluated the implications of polymer-conjugation on the interactions (as measured by the second virial coefficient) between proteins in solution for the particular example of single- and double-PEGylated BSA in dilute PBS solution. The effect of PEGylation on A_2 is found to sensitively depend on *both* the composition and the distribution of PEG segments within the conjugate. For mono-PEGylated BSA, A_2 increases with the degree of polymerization (and hence volume fraction) of PEG, in the limit of high molecular tethers (M_w = 30 kDa) good solvent characteristics are observed. At constant PEG volume fraction, A_2 significantly increases with the degree of polymerization of tethered chains – this suggests that 'a fewer number of long chains is more effective in raising the stability of protein-conjugates in solution than a correspondingly larger number of short chains'. The analysis of the hydrodynamic radii of protein-PEG conjugates suggests that the increased solubility in the case of high molecular tethers is concurrent with a structural transition that results in the conformation of more core-shell type structures ('shroud' structure). Our results thus provide new insights into the link between architecture and the structure and solubility of protein-PEG conjugates that we hope will benefit the understanding of the biochemical characteristics of protein conjugates and the design of protein-conjugates for functional material applications.

Chapter 6: Polymer-Functionalized Proteins as Fillers in Block Copolymer Systems

6.1 Background and Motivation

As explained in the introduction to this thesis document, the present work is part of a bigger effort to develop enzyme-actuated block copolymer membranes. One possible strategy to facilitate the incorporation of enzymes into the block copolymer template is the co-assembly of the copolymer with enzyme fillers that are functionalized to allow for selective enrichment of the enzyme in a respective block copolymer domain. The purpose of this section is to develop understanding of the fundamental governing parameters that define structure formation and solubilization in binary block copolymer/enzyme blend systems. In the following text, a brief review will be provided on relevant previous work in the field of block copolymer/protein blend systems as well as the general topic of block copolymer/nanoparticle blend systems that contributes the broader context for the present work. Three major routes have been described in the literature to facilitate the incorporation of proteins into BCPs: adsorption to the surface of the membrane, substitution of protein as one block in the BCP, and co-assembly of the protein and the BCP cast from the same solution [18,67]. Liu *et al.* demonstrated that an array of BSA can be created by preferentially adsorbing the protein to PS in ordered PS-*b*-PI [68]. Olsen *et al.* have investigated the incorporation of proteins into matrices by synthesizing a protein-polymer BCP, mCherry-*b*-PNIPAM [69–71]. Upon solvent annealing the sample, they observe lamellar and cylindrical structures using TEM and SAXS. They also maintained 70-95% of the protein function after casting. Previous work on the co-assembly of enzymes with block copolymer matrices, the focus of this study, is limited. Xu *et al.* demonstrated that biologically active proteins and their cofactors could be incorporated together in thin films of cylindrical PS-*b*-PEO

while preserving the protein's structure and activity [72]. Russell *et al.* demonstrated in 2005 that ferritin-PEG conjugates could be incorporated into lamellar diblock copolymer thin films via the co-assembly process (P2VP-*b*-PEO) [73]. They observed a suppression of PEO crystallization with the addition of the ferritin-PEG using optical microscopy and AFM. In 2010, Russell *et al.* cast thin films of PS-*b*-PEO with neat ferritin and ferritin-polyPEGMA that maintained their cylindrical structure but experienced an increase in spacing [74]. Beyond this proof of concept, no systematic study on dispersion of polymer-functionalized proteins in a BCP exists in literature.

To optimize the effectiveness of the enzyme compatibilization approach, information about miscibility, dispersion, order-order transitions, and solubility limits in co-assembled systems is required. The ideal system would contain the minimum volume fraction of polymer grafts (necessary for maintaining miscibility and preventing aggregation) and would contain the maximum amount of enzyme (active component of the system). Therefore, a systematic study of the effect of polymer grafts on dispersion behavior and transitions that occur in a model BCP is necessary to provide understanding of these technologically relevant systems.

As elaborated on in the *Background* section, a significant amount of research has focused on understanding the governing parameters controlling dispersion of particle fillers in block copolymer blends. In analogy to particle-in-homopolymer blends, miscibility of additives is expected in the case of favorable interactions between fillers and matrix for the grafting of chains with sufficient chain length to facilitate homogenization.

In addition, theoretical studies by Balazs and coworkers point to the relevance of characteristic length scales on both the compatibility as well as dispersion characteristics on particle fillers in BCP templates. Specifically, these authors predict particles to exhibit a characteristic transition between interfacial vs. domain center alignment with increasing characteristic ratio D/L, where D

is the particle size and *L* is the block copolymer domain thickness [57]. It is a major objective of this study to test whether these predicted structural transitions also occur for soft particle filler (protein) / BCP blends.

Previous work by Ausserré *et al.* and Listak *et al.* has experimentally evaluated the role of filler size on dispersion of nanoparticles and homopolymer in model BCP systems [62,120]. Specifically, Listak *et al.* investigated the role of characteristic length scales for the case of PS-functionalized gold particles dispersed in poly(isoprene-*b*-styrene-*b*-isoprene) triblock copolymers. Overall, the experimental observation confirmed previous theoretical work by Balazs [57].

Balazs *et al.* have suggested that evaluation of dispersion is size-dependent and not related to the chemical identify of the filler [57]. Yu *et al.* have performed simulations varying the number of grafts and the length of the grafts to predict dispersion of Au-PS in PS-*b*-P2VP, where Au is preferential to P2VP and PS grafts are enthalpically neutral with the PS domain in the BCP [121]. They found that for particles with very few short grafts, dispersion occurred along the IMDS and for particles many long grafts, dispersion occurred at the center of the PS domain. However, nanoparticles with an intermediate number of grafts with an intermediate length dispersed at both the IMDS and the center of the PS domain, and the volume fraction of the graft was important, since a nanoparticle with many short chains could disperse the same way as a nanoparticle with few long chains.

As is apparent from the previous discussion, research on structure formation in BCP/particle blends has mostly focused on inorganic particle fillers. It is not clear whether the conclusions derived on this basis also pertain to biological fillers. Differences could arise, for example, due to the different density of polymer ligands (typically high for inorganic particles and low for organic fillers) or due to the 'softness' of the particle core that could affect interactions in blend

systems. Also, biological fillers, due to their intrinsic uniform structure, might provide better model systems to test theoretical predictions as compared to inorganic particles that often exhibit distributions of particle size.

The objective of the work performed in this chapter is to elucidate structure formation processes in BCP/'protein particle' systems and to determine how structural parameters such as number and molecular weight affect the solubility limit, order-order transition, and dispersion characteristics of polymer-conjugated protein in BCP matrices.

The system in our study consists of Bovine Serum Albumin (BSA) modified with poly(ethylene glycol) (PEG) ligands dispersed in symmetric poly(styrene-*b*-methyl methacrylate) (PS-*b*-PMMA) copolymers. BSA was chosen based on its availability and relative stability. BSA is frequently used by researchers at FLIR Systems, our collaborators, as a model system to test product designs. PS-*b*-PMMA was selected because of its amorphous character and well-established structure formation, and PEG ligands were chosen because of the slightly favorable interactions between PEG and PMMA that should promote BSA dispersion. In particular, the relevant χ parameters for the present system are $\chi_{PS/PMMA} = 0.0044$, $\chi_{PEG/PMMA} = -0.005$ and $\chi_{PEG/PS} = 0.0644$, at $T = 25°C$ [122,123].

The original objective of this study was to evaluate the role of ligand composition as well as characteristic length scales by using combined TEM and SAXS analysis of blend systems with varying number and degree of polymerization of PEG conjugates as well as distinct PS-*b*-PMMA molecular weights (at about equal volume composition). Due to instrument limitations, SAXS analysis has not been performed; however, a description of the data acquisition procedure and data interpretation steps is provided.

6.2 Sample Preparation

6.2.1 Materials

Bovine Serum Albumin (BSA, $M_w \approx 67$kDa) was purchased from Sigma Aldrich, and methoxy-PEG-succinimidyl carboxymethyl ester (mPEG-NHS, M_w = 2kDa, 3kDa, 5kDa, 10kDa, and 30kDa) was purchased from JenKem Technology USA. The block copolymers, poly(styrene)-*b*-poly(methyl methacrylate) (PS-*b*-PMMA, $M_{w\,PS}$ = 50k g/mol, $M_{w\,PMMA}$ = 48k g/mol, PDI = 1.12; $M_{w\,PS}$ = 42.2k g/mol, $M_{w\,PMMA}$ = 42.2k g/mol, PDI = 1.06; PS-*b*-PMMA, $M_{w\,PS}$ = 21k g/mol, $M_{w\,PMMA}$ = 21k g/mol, PDI = 1.07; PS-*b*-PMMA, $M_{w\,PS}$ = 203.5k g/mol, $M_{w\,PMMA}$ = 203.5k g/mol, PDI=1.10), were purchased from PolymerSource (98k and 42k) and PSS (84k and 407k). Phosphate buffered saline (PBS) was purchased from Sigma Aldrich (pH 7.4, 0.0027 M KCl, 0.138 M NaCl). Pyridine was purchased from Fisher Scientific. All materials were used as received.

6.2.2 Synthesis

The protein-polymer conjugates were synthesized using a non-specific coupling reaction between mPEG-NHS and the lysine residues of BSA in a phosphate buffered saline solution. For each molecular weight, synthesis was performed for different molar concentration ratios of mPEG-NHS:lysine residues to vary the number of PEG grafts on BSA. The solutions were stirred for 1 hour before 3 μL of 0.1 M HCl solution was added to end the reaction. The unreacted mPEG-NHS was filtered by dialysis using a 50 kDa membrane filter (Spectrum Labs Float-A-Lyzer) for 72 hours in DI water. Samples were subsequently lyophilized using a Labconco Cascade FreeZone Plus 2.5 Freeze-Dry System operated at -84 °C and 0.035 mBar. Ultraviolet – Visible Spectroscopy (UV-Vis) was performed to confirm the purity of the dialyzed

and lyophilized product. Data was collected using a Cary 300 Scan UV-Vis Spectrophotometer at room temperature in absorption mode over the wavelength range of 200 – 300 nm using a quartz cuvette filled with dilute solutions of BSA-PEG conjugate samples in PBS. It was found that dialysis was an effective purification technique for conjugates.

6.2.3 Block Copolymer/Protein-Polymer Blend Preparation

A neat film of PS-*b*-PMMA was solvent cast from an 8.5 wt. % polymer solution in pyridine over two weeks. Slow solvent evaporation in a solvent environment allows for an equilibrium structure to be obtained. Samples were placed under vacuum conditions at room temperature for six weeks to remove additional solvent from the bulk films. Three samples were made from the resulting 1 mm thick film: 'as cast' and '3 days thermally annealed' with the thermal annealing taking place in a vacuum oven set to 150°C, above the glass transition temperatures of the constituent blocks. Blends were made by adding 1, 5, and 10 wt.% BSA-PEG samples to the polymer solution in pyridine. Film preparation for the blend systems followed the same procedure described for the neat block copolymer film.

6.2.4 Solvent Selection

Pyridine was selected as the solvent for this study, after consideration of the solubility of PS, PMMA, PEG, and PEG-protein in several organic solvents including tetrahydrofuran (THF), chloroform, toluene, dimethylformamide (DMF), dichloromethane, and cyclohexanone. The solubility parameter of pyridine ($\delta_{pyridine}$ = 10.9 $(cal/cm^3)^{1/2}$) is very close to the solubility parameter of each of the system components (δ_{PS} = 9.8 $(cal/cm^3)^{1/2}$, δ_{PMMA} = 9.2 $(cal/cm^3)^{1/2}$, and δ_{PEG} = 9.9 $(cal/cm^3)^{1/2}$) [124,125]. Each of the three polymers was dissolved at a concentration of 30

mg/mL and left stirring for 24 hours, before the turbidity was visually examined. PEGylated trypsin (a model enzyme) was also dissolved at a concentration of 5.8 mg/mL and left stirring for 24 hours. Pyridine was the only solvent of those tested that successfully dissolved all components of the system.

6.3 Characterization Techniques

6.3.1 Transmission Electron Microscopy (TEM)

Films were microsectioned at −120 °C using a LEICA EM FCS cryoultramicrotome. To enhance contrast, 70 nm thick microsections were stained for 5 to 15 minutes using ruthenium tetroxide (obtained from EM Sciences), which preferentially stains the PS domain [86]. TEM was performed using a JEOL 2000 EX electron microscope operated at 200 kV. Imaging was done by amplitude and phase contrast, and images were acquired using a Gatan Orius SC600 high-resolution camera.

6.3.2 Small Angle X-ray Scattering (SAXS)

SAXS data was acquired under vacuum using a Rigaku S-Max3000 with a 2D multiwire detector. Two-dimensional SAXS patterns were azimuthally integrated to obtain plots of scattered intensity vs. momentum transfer vector, $q = (4\pi/\lambda)\ sin\ \theta$, where θ is half the scattering angle and $\lambda = 1.54$ Å. Peaks were fit with Gaussian functions to determine the locations of the peak maxima.

6.3.3 Analysis of Particle Dispersion Morphologies using SAXS

Changes observed in lamellar spacing measured using SAXS can be described by the following equations:

$$L = L_0(1 + \frac{\phi_{filler}}{3}) \tag{37a}$$

$$L = L_0(1 + \phi_{filler}) \tag{37b}$$

for homogeneous dispersion and for center segregation, respectively, where L is the lamellar spacing of the blend system, L_0 is the lamellar spacing of the neat BCP, and ϕ is the volume fraction of the filler [62].

6.4 Evaluation of Lamellar Spacing

6.4.1 Neat Block Copolymer

PS-*b*-PMMA is a model block copolymer system that has been widely studied. It has an amorphous structure, and the PMMA block is miscible with PEG, which was used to functionalize BSA in this study ($\chi_{PEG/PMMA}$ = -0.005 and $\chi_{PEG/PS}$ = 0.0644, at T = 25°C) [122]. Due to the symmetric molecular weights of the two blocks, the equilibrium structure consists of lamellae equal in size. This was confirmed for the neat BCP, PS-*b*-PMMA (50k-*b*-48k), using SAXS, an X-ray technique suitable for periodic materials with length scales on the order of tens of nanometers. The schematic in Figure 6-1 depicts the X-ray beam incident upon the sample (K_0) and the X-ray beam scattered by the sample (K). The momentum transfer vector q is the difference between K_0 and K and is defined by the following equation:

$$q = \left(\frac{4\pi}{n\lambda}\right) sin\theta \tag{38}$$

where θ is half the scattering angle and λ = 1.54 Å. The lamellar spacing, L, can be calculated

using q^* (the first scattering peak) via the following relation:

$$L = \frac{2\pi}{q*} \tag{39}$$

For a lamellar structure, the characteristic ratios of the scattering vectors are the integers, $q/q^* = 1, 2, 3, 4, 5$. When the volume fractions of the two blocks in a lamellar system are symmetric ($\phi_A = \phi_B = 0.5$), the even peaks are suppressed. This can be seen by the equation for scattering intensity: $I \sim sin^2(n \phi \pi)$, which equals zero when n (the peak number) is even.

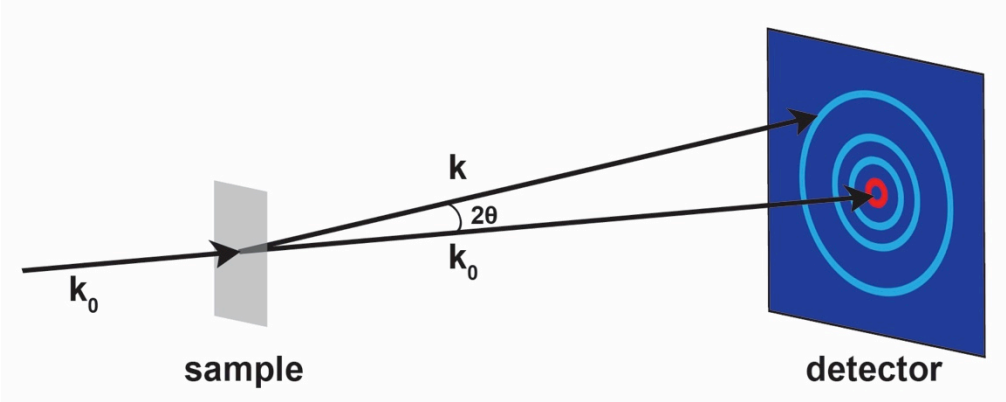

Figure 6-1. Schematic depicting the detection of scattered X-rays in SAXS.

In this study, samples of neat PS-*b*-PMMA with varied M_w as well as similar samples blended with BSA-PEG were cast and evaluated using TEM. Due to limitations regarding SAXS data acquisition, a comparative study of lamellar spacings for neat and blended BCPs could not be completed to determine the segregation of BSA-PEG in the BCP as a function of the graft characteristics. Preliminary data shown in Figure 6-2 for PS-*b*-PMMA (50k-*b*-48k) exhibits a lamellar structure supported by TEM and SAXS.

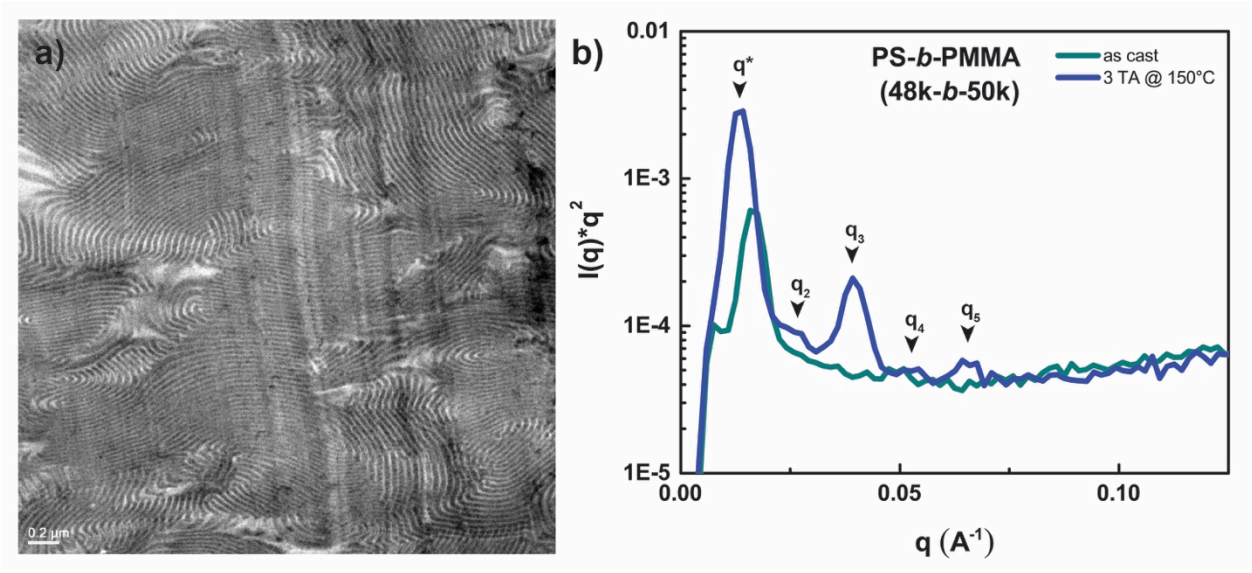

Figure 6-2. (a) TEM micrograph of PS-*b*-PMMA (48k-*b*-50k, PDI = 1.12) solvent cast in pyridine for 5.5 days and thermally annealed for 3 days at 150°C. The sample was stained with RuO_4, a selective stain for PS, for 5 mins. prior to imaging in bright field mode. (b) SAXS intensity profile for the same PS-*b*-PMMA sample in the 'as cast' condition and after thermally annealing for 3 days at 150°C. Peaks for the 3TA sample are indicated with arrows.

The theoretical lamellar spacing can be calculated using the following equations:

$$R_{G,PS}^2 = \frac{N_{PS}^{2\upsilon} * a_{PS}^2}{(2\upsilon+1)(2\upsilon+2)} \tag{40a}$$

$$R_{G,PMMA}^2 = \frac{N_{PMMA}^{2\upsilon} * a_{PMMA}^2}{(2\upsilon+1)(2\upsilon+2)} \tag{40b}$$

$$R_{G,PS-b-PMMA} = \sqrt{R_{G,PS}^2 + R_{G,PMMA}^2} \tag{40c}$$

where R_G is the radius of gyration, N is the degree of polymerization, a is the Kuhn length (1.8 nm for PS and 1.7 nm for PMMA), and υ is the Flory Parameter (1/2 for a theta solvent, 3/5 for a good solvent) [126].

Slight differences in lamellar spacing occur when comparing results from SAXS with those from TEM. TEM surveys micron-sized areas, while SAXS is representative of the whole sample. For this reason, SAXS data is more suitable for this analysis. However, TEM remains a useful tool

for confirming a lamellar structure and/or identifying the presence of aggregates for blends reaching the solubility limit.

6.4.2 Block Copolymer/Polymer-Functionalized Protein Blends

PS-*b*-PMMA/BSA-PEG blend systems can be used to answer the following questions:

1. What is the role of polymer graft characteristics on dispersion of polymer-functionalized proteins in a model block copolymer system?
2. At what filling fraction does the block copolymer undergo an order-order phase transition?
3. What is the solubility limit of polymer-functionalized proteins in a block copolymer matrix?

To determine the role of polymer graft characteristics on dispersion, several blend samples were fabricated. Dispersion of fillers in a BCP can be along the IMDS or in the center of the compatible polymer domain. In both cases, TEM and SAXS can be used to detect the dispersion, TEM with visual inspection of micrographs (provided the contrast is sufficient) and SAXS with changes in lamellar spacing (L). Literature on BCP/inorganic nanoparticle blend systems has suggested that the ratio of filler diameter to lamellar spacing (D/L) can predict the type of dispersion. A ratio of $D/L \leq 2$ indicates dispersion along the IMDS, while a ratio of $D/L \geq 3$ indicates center segregation in the compatible polymer domain. By dispersing the same sample in BCPs with varied molecular weights, dispersion in systems with several D/L ratios can be examined. PS-*b*-PMMA with molecular weights of 21k-*b*-21k, 42.2k-*b*-42.2k, and 203.5k-*b*-203.5k g/mol served as the matrices for a wide range of BSA-PEG samples, as shown in Table 6-1.

Table 6-1. Matrix of samples with varied filling fraction of BSA-PEG conjugates in a PS-*b*-PMMA matrix of low, medium, or high M_w.

Protein-Polymer Conjugate	Matrix PS-*b*-PMMA 21k-*b*-21k g/mol	Matrix PS-*b*-PMMA 42.2k-*b*-42.2k g/mol	Matrix PS-*b*-PMMA 203.5k-*b*-203.5k g/mol
BSA-PEG2k		1, 5, 10%	
BSA-PEG3k		1, 5, 10, 25, 50%	
BSA-PEG5k-1		1, 2.5, 5%	
BSA-PEG5k-2	1, 5, 10%	1, 5, 10%	1, 5, 10%
BSA-PEG10k-1		1, 5, 10%	
BSA-PEG10k-2	1, 5, 10%	1, 5, 10%	1, 5, 10%
BSA-PEG30k		1, 5, 10%	

Comparisons of different samples in the matrix yield information about the role of various graft characteristics. A series of relevant samples blended with PS-*b*-PMMA (42.2k-*b*-42.2k g/mol) are described here. Evaluation of BSA-PEG10k-1 and BSA-PEG10k-2 in PS-*b*-PMMA (42.2k-*b*-42.2k g/mol) can show the importance of the average number of grafts, while holding the graft length constant. Comparison of BSA-PEG10k-2 and BSA-PEG30k in PS-*b*-PMMA (42.2k-*b*-42.2k g/mol) can offer insight into the importance of graft M_w and average number of grafts ($\langle g \rangle$ = 2.5 for BSA-PEG10k-2 and $\langle g \rangle$ = 0.83 for BSA-PEG30k), while holding the mass percent of PEG constant. The evaluation of four samples with $\langle g \rangle \sim 1$ in PS-*b*-PMMA (42.2k-*b*-42.2k g/mol) can show the importance of graft M_w ($\langle g \rangle$ = 0.83 for BSA-PEG10k-2 and BSA-PEG30k, while $\langle g \rangle$ = 1.15 for BSA-PEG2k and BSA-PEG3k). Another comparison of two samples with similar average number of grafts ($\langle g \rangle \sim 2.5$) in PS-*b*-PMMA (42.2k-*b*-42.2k g/mol) offers additional insight into the importance of graft M_w ($\langle g \rangle$ = 2.25 for BSA-PEG5k-2 and $\langle g \rangle$ = 2.5 BSA-PEG10k-2). The importance of filling fraction on the miscibility limit can be evaluated with the BSA-PEG3k samples in PS-*b*-PMMA (42.2k-*b*-42.2k g/mol) (χN = 34.3) at filling

fractions of 1, 5, 10, 25, and 50%. A filling fraction of 50% is calculated to be a filling fraction of 100% with respect to the PMMA domain.

Two BSA-PEG samples were also blended with PS-*b*-PMMA 21k-*b*-21k and 203.5k-*b*-203.5k g/mol to evaluate the role of the characteristic ratio, *D/L*, on the dispersion behavior for conjugates with similar average number of grafts ($<g> \sim 2.5$) but different graft M_w and R_H as measured by DLS (R_H = 4.3 nm for BSA-PEG5k-2 and R_H = 5.3 for BSA-PEG10k-2). The characteristic ratio ranges from 0.10 to 0.38 and from 0.19 to 0.59 for BSA-PEG5k-2 assuming good and theta solvents, respectively. The characteristic ratio ranges from 0.12 to 0.46 and from 0.23 to 0.73 for BSA-PEG10k-2 assuming good and theta solvents, respectively, as shown in Table 6-2.

Table 6-2. (*D*/*L*) values for each combination of PS-*b*-PMMA/BSA-PEG5k-2 and PS-*b*-PMMA/BSA-PEG10k-2. They span a wide range and include the value 0.2 and 0.3, shown in literature to be important predictors of dispersion behavior for inorganic fillers.

Matrix PS-*b*-PMMA M_w (g/mol)	***D/L* (Good Solvent) BSA-PEG5k-2**	***D/L* (Good Solvent) BSA-PEG10k-2**	***D/L* (Theta Solvent) BSA-PEG5k-2**	***D/L* (Theta Solvent) BSA-PEG10k-2**
21k-*b*-21k	0.38	0.46	0.59	0.73
42.2k-*b*-42.2k	0.24	0.29	0.41	0.50
203.5k-*b*-203.5k	0.10	0.12	0.19	0.23

Selected samples were microtomed and stained in preparation for TEM analysis. Figures 6-3a&d show that for neat PS-*b*-PMMA 21k-*b*-21k and 42.2k-*b*-42.2k, the 'as cast' samples do not exhibit an equilibrium lamellar structure. After thermally annealing the samples for 3 days at 150°C, a lamellar structure begins to become visible using TEM, as shown in Figures 6-3b&e. The lamellar structure is maintained after blending with BSA-PEG5k-2 (10%) and thermally annealing for 3 days at 150°C, as depicted in Figures 6-3c&f.

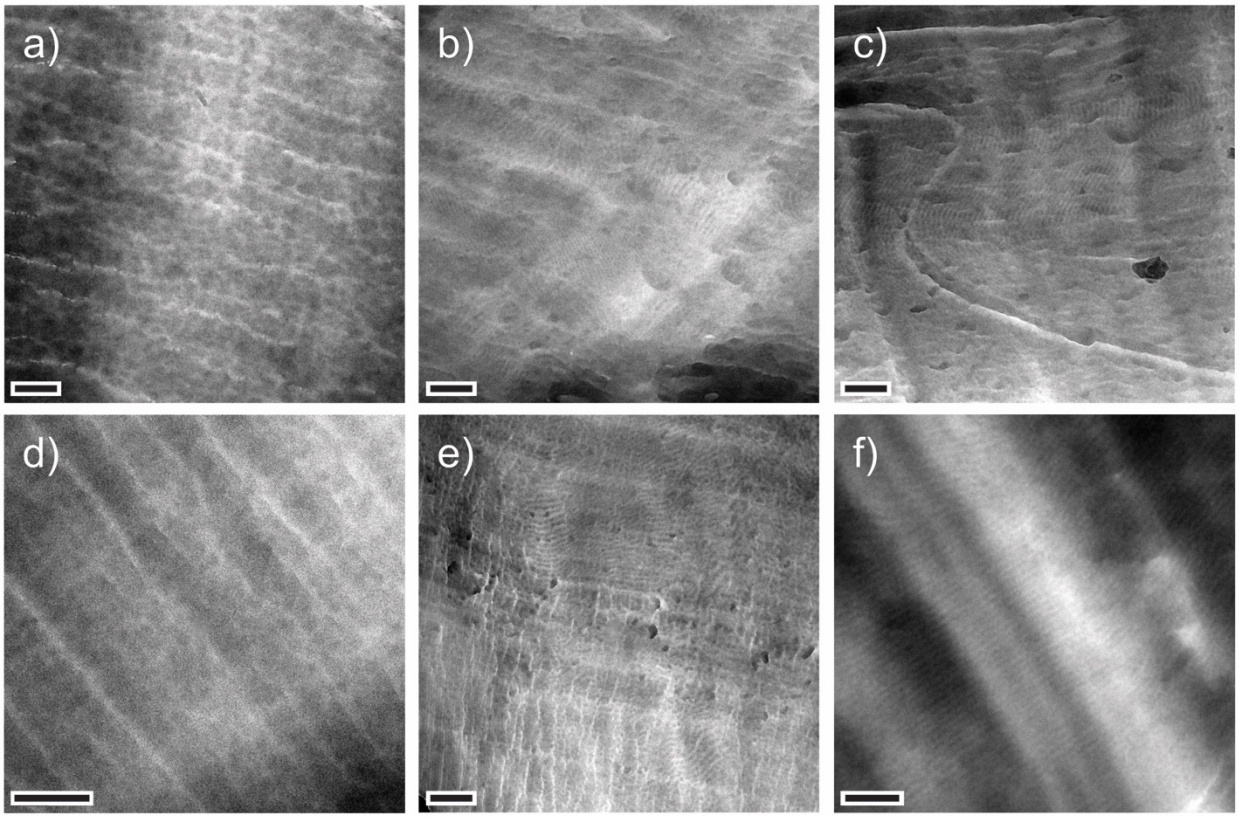

Figure 6-3. TEM micrograph of PS-*b*-PMMA 21k-*b*-21k in the (a) 'as cast' state, (b) after thermal annealing for 3 days at 150°C, and (c) blended with BSA-PEG5k-2 (10%) and thermally annealed for 3 days at 150°C. TEM micrograph of PS-*b*-PMMA 42.2k-*b*-42.2k in the (d) 'as cast' state, (e) after thermal annealing for 3 days at 150°C, and (f) blended with BSA-PEG5k-2 (10%) and thermally annealed for 3 days at 150°C. Scale bar is 200 nm for all images.

These samples don't exhibit phase separation and are suitable for analysis using SAXS and WAXS. These experiments would investigate the dispersion of polymer-functionalized proteins in BCP matrices and would fill gaps in the literature regarding the extension of observations made for inorganic nanoparticle fillers to biological nano-sized fillers.

6.5 Conclusions

BSA-PEG conjugates were blended with PS-*b*-PMMA matrices with varied M_w using a solvent annealing casting method. A lamellar structure was obtained after thermally annealing the samples for 3 days at 150°C. The structure was maintained for filling fractions of up to 10%. The sample matrix was carefully selected to evaluate the effect of a wide range of parameters on the dispersion behavior of protein-polymer conjugates in a BCP matrix, such as the average number of grafts, the length (M_w) of the grafts, and the mass fraction of grafts. The maximum filling fraction and the importance of the characteristic ratio (size of the filler to the domain spacing) were also of interest. Due to instrument limitations, SAXS analysis could not be performed; however, once collected, this data would provide information on the lamellar spacings and subsequently, the dispersion behavior of polymer-functionalized organic fillers.

Chapter 7: Conclusions and Future Work

7.1 Conclusions

This thesis aims to elucidate (some of) the governing parameters that control the dispersion of protein-based fillers in solvent as well as polymer and block copolymer matrix materials. The aim is to both contribute to the fundamental understanding of how 'polymer graft characteristics' (such as degree of polymerization and grafting density) relate to changes in the miscibility characteristics and to develop guidelines that will allow the fabrication of block copolymer/enzyme blend materials with maximum enzyme loading. In a collaborative effort with industrial and academic partners, a "biomimetic" membrane system consisting of a porous triblock terpolymer decorated with enzymes has been developed. The enzymes are matched to selected toxins of interest and can neutralize them by cleaving bonds, producing acid that triggers swelling of a pH-responsive polymer lining the pores. Mechanical and functional stability have been evaluated, and scale up of the membranes is being pursued. The role of graft architecture on the solubility (via A_2) of protein-polymer conjugates in dilute aqueous solutions was evaluated using a combination of Static and Dynamic Light Scattering. It was found that solubility increases with increasing mass percent PEG, and that for samples with different graft architecture but similar average number of grafts or mass percent PEG, higher M_w grafts increase solubility. In addition, the hydrodynamic radius determined by light scattering matched expected radii calculated for the cases of 'dumbbell' and 'shroud' conformations, for low and high M_w grafts, respectively, with a transition occurring at grafts of 10kDa M_w. This is an important finding, since it provides guidance on the optimization of protein-polymer conjugates designed for use in a variety of applications ranging from military garments and filtration devices to pharmaceutical drug delivery. To evaluate dispersion in a model BCP matrix, the protein-

polymer conjugates were blended with PS-*b*-PMMA, and a lamellar structure was achieved after thermally annealing the samples above the *Tg* of the BCP components for 3 days. This structure was maintained for filling fractions up to 10%. A matrix of samples was constructed selected to evaluate the effect of a wide range of parameters on the dispersion behavior of protein-polymer conjugates in a BCP matrix, such as the average number of grafts, the length (M_w) of the grafts, and the mass fraction of grafts. The maximum filling fraction and the importance of the characteristic ratio (size of the filler to the domain spacing) were also of interest. Due to instrument limitations, SAXS analysis could not be performed; however, once collected, this data would provide information on the lamellar spacings and subsequently, the dispersion behavior of polymer-functionalized organic fillers.

7.2 Future Work

Future work includes the analysis of the dispersion morphologies of BSA-PEG in a symmetric (i.e. lamellar structure forming) model block copolymer matrix (based on poly(styrene-*b*-methyl methacrylate), PS-*b*-PMMA). As described in *Chapter 6*, blends with 1, 5, and 10% of selected BSA-PEG conjugates have been blended with PS-*b*-PMMA with M_w of 21k-*b*-21k, 42.2k-*b*-42.2k, and 203.5k-*b*-203.5k. Due to equipment limitations, these samples have not yet been analyzed using SAXS. This analysis would allow for the evaluation of parameters such as the solubility limit, the maximum protein loading, order-order transitions as well as the dispersion morphology of fillers within copolymer domains as a function of copolymer molecular weight and BSA-PEG composition. These results would add to the better understanding of the structure formation in block copolymer/particle filler blend materials that have attracted significant attention for the case of inorganic derived particle systems. One question yet to be addressed is the role of the filler/domain size ratio that was found to be an important parameter for inorganic

particle filled systems. To this end preliminary experiments have been performed to (i) identify a common solvent that enables casting of PS-*b*-PMMA/BSA-PEG blend systems and (ii) establish the equilibrium domain structure of four distinct PS-*b*-PMMA materials with varying molecular weight.

Appendix A – MALDI-TOF Data

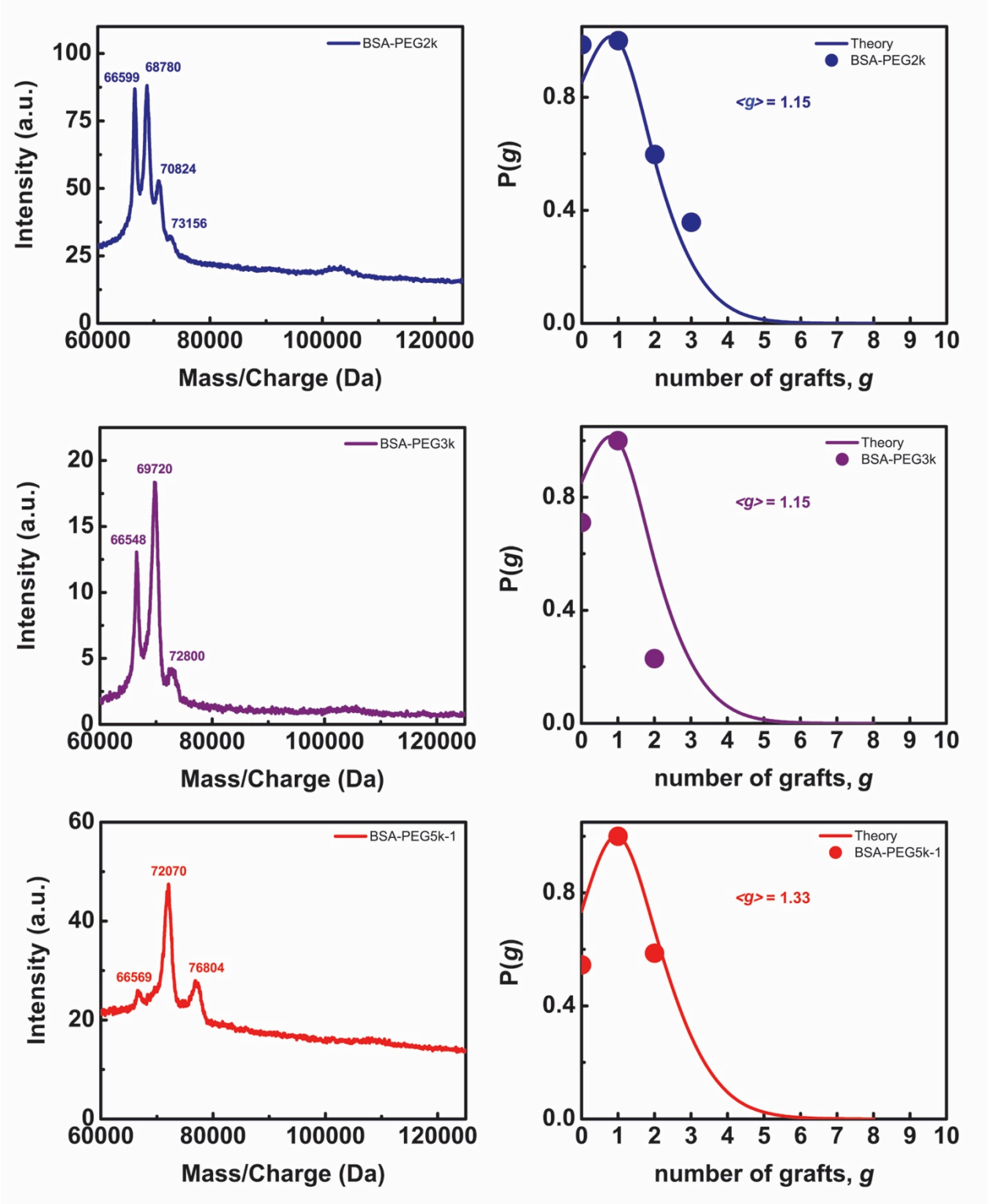

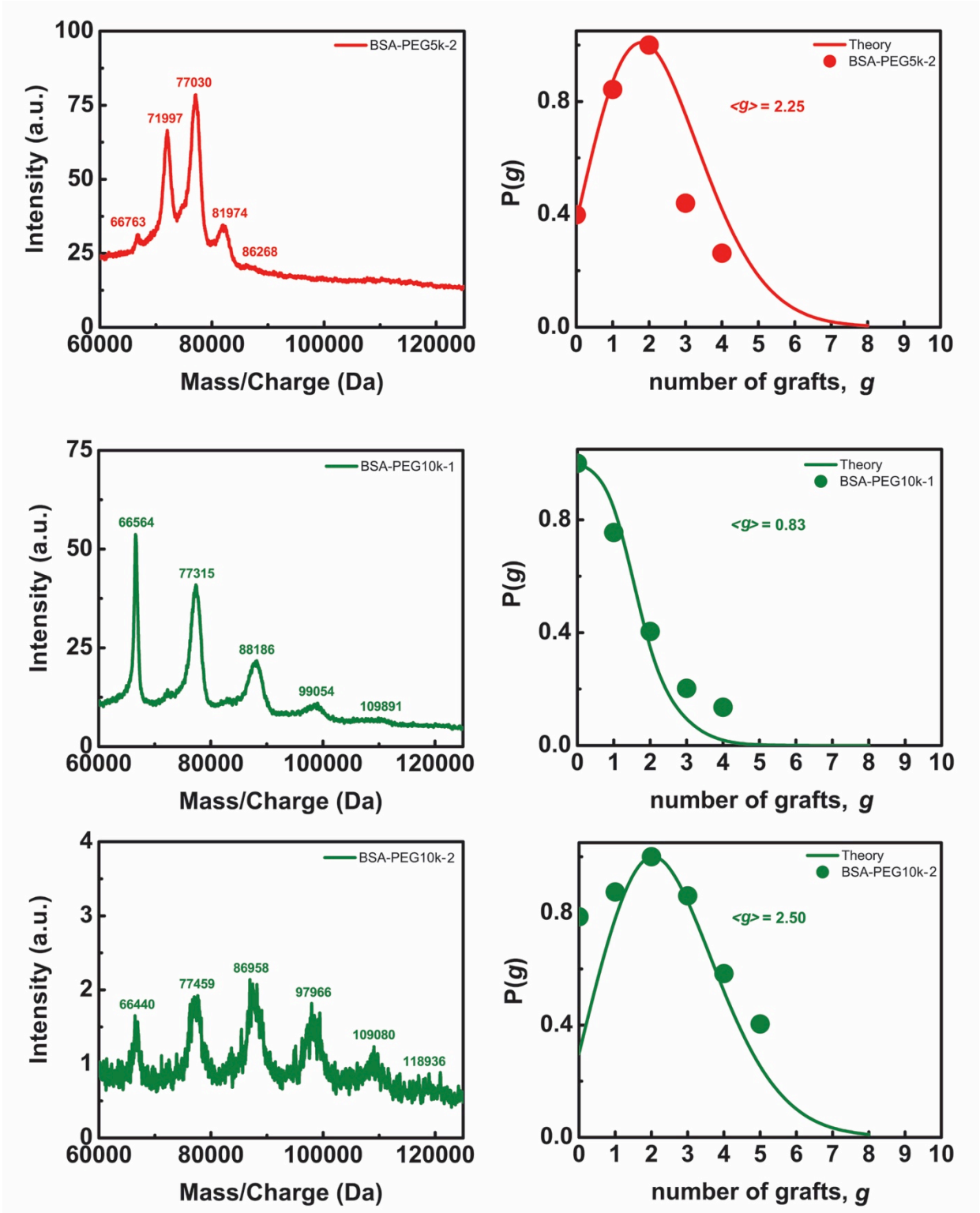
BSA-PEG5k-2
Intensity (a.u.)
Mass/Charge (Da)
66763
71997
77030
81974
86268
Theory
BSA-PEG5k-2
<g> = 2.25
P(g)
number of grafts, g
BSA-PEG10k-1
66564
77315
88186
99054
109891
<g> = 0.83
BSA-PEG10k-2
66440
77459
86958
97966
109080
118936
<g> = 2.50

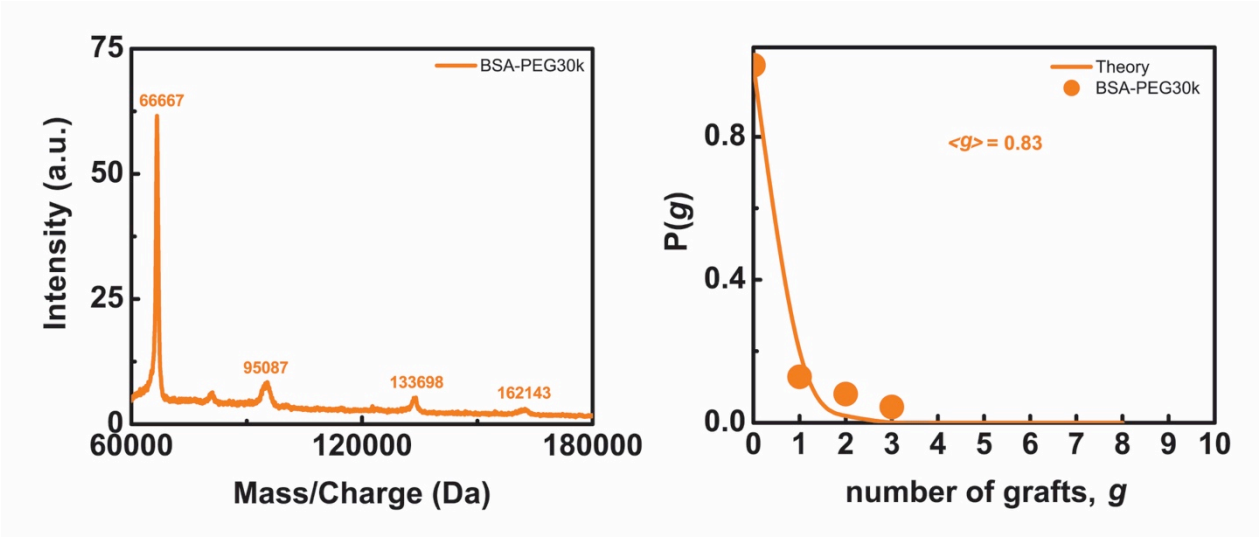
BSA-PEG30k
66667
95087
133698
162143
Intensity (a.u.)
Mass/Charge (Da)
Theory
BSA-PEG30k
<g> = 0.83
P(g)
number of grafts, g

Appendix B – SLS Data

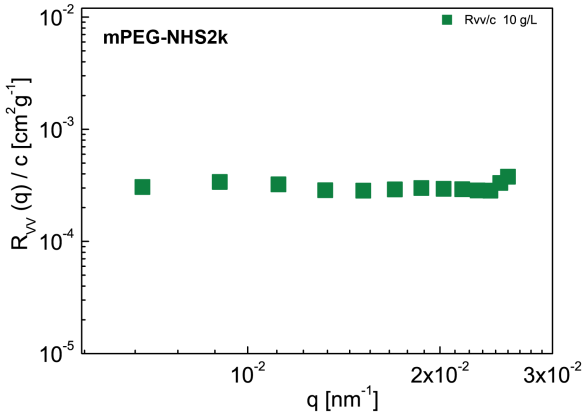

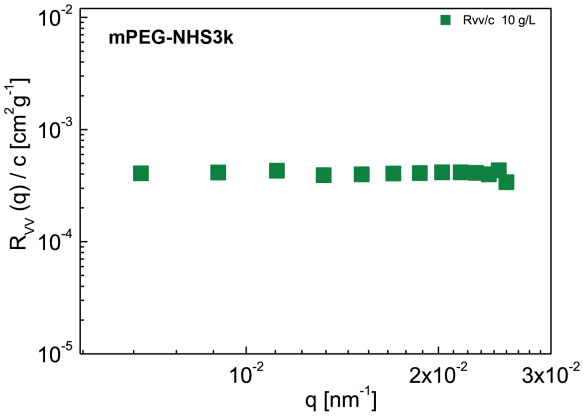

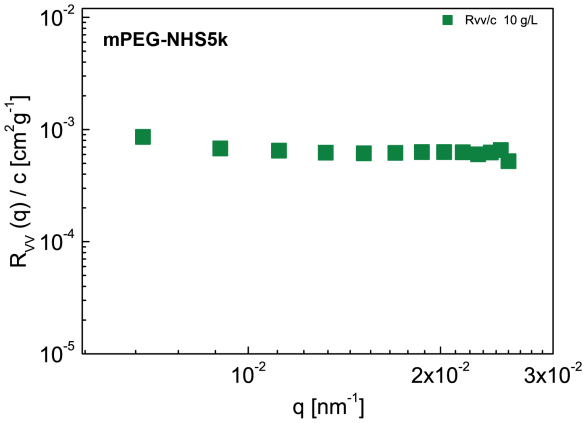

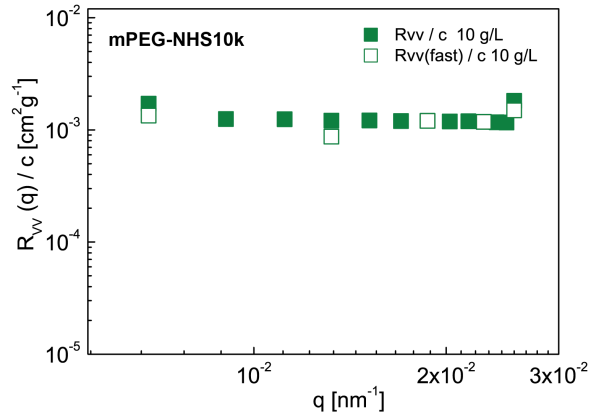

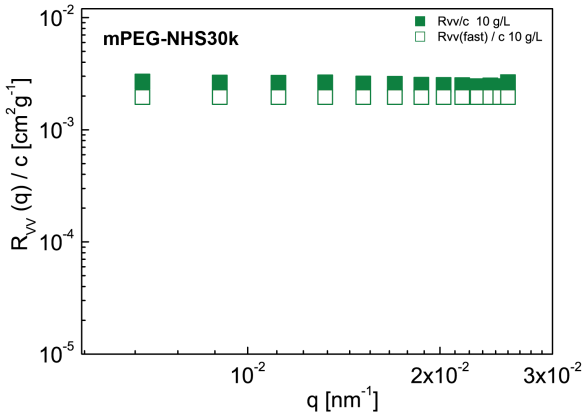

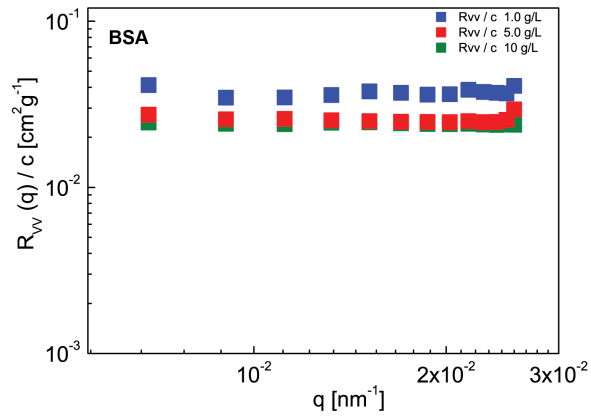

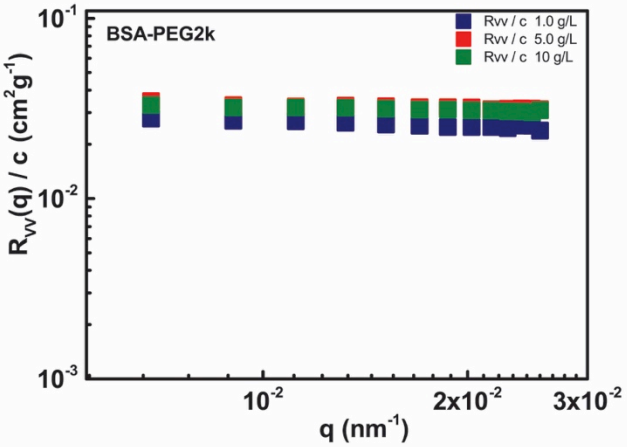
BSA-PEG2k
Rvv / c 1.0 g/L
Rvv / c 5.0 g/L
Rvv / c 10 g/L
$R_{VV}(q) / c\ (cm^2 g^{-1})$
10^{-1}
10^{-2}
10^{-3}
10^{-2}
$2x10^{-2}$
$3x10^{-2}$
q (nm^{-1})

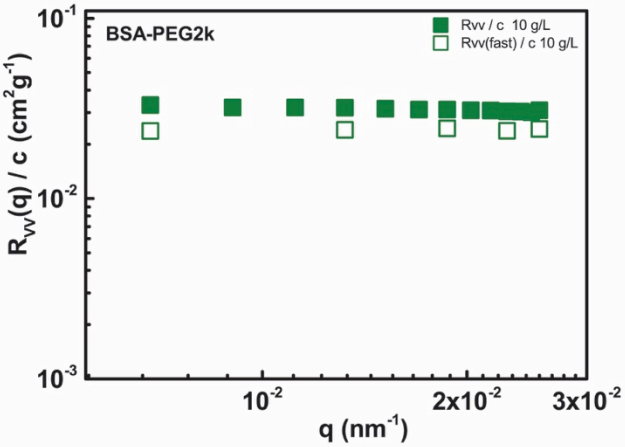
BSA-PEG2k
Rvv / c 10 g/L
Rvv(fast) / c 10 g/L
$R_{VV}(q) / c\ (cm^2 g^{-1})$
10^{-1}
10^{-2}
10^{-3}
10^{-2}
$2x10^{-2}$
$3x10^{-2}$
q (nm^{-1})

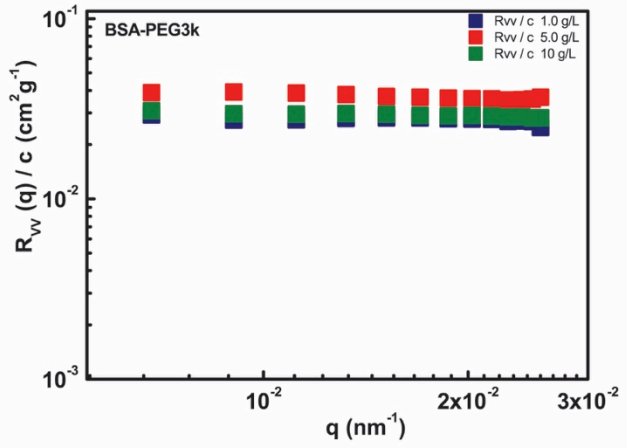
BSA-PEG3k
Rvv / c 1.0 g/L
Rvv / c 5.0 g/L
Rvv / c 10 g/L
$R_{VV}(q) / c\ (cm^2 g^{-1})$
10^{-1}
10^{-2}
10^{-3}
10^{-2}
$2x10^{-2}$
$3x10^{-2}$
q (nm^{-1})

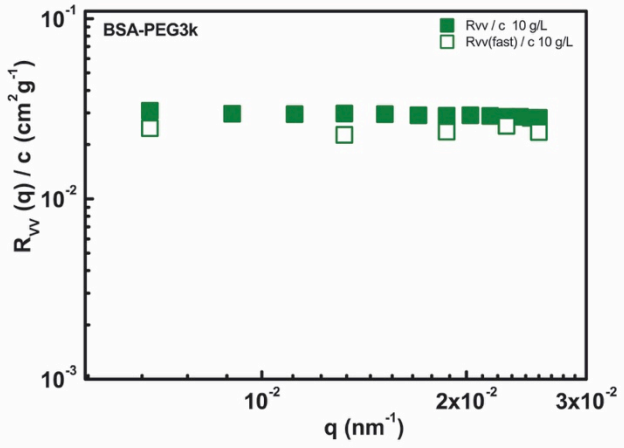
BSA-PEG3k
Rvv / c 10 g/L
Rvv(fast) / c 10 g/L
$R_{VV}(q) / c\ (cm^2 g^{-1})$
10^{-1}
10^{-2}
10^{-3}
10^{-2}
$2x10^{-2}$
$3x10^{-2}$
q (nm^{-1})

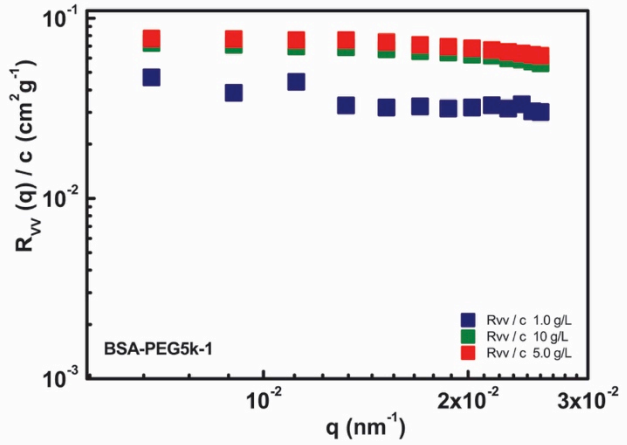
BSA-PEG5k-1
Rvv / c 1.0 g/L
Rvv / c 10 g/L
Rvv / c 5.0 g/L
$R_{VV}(q) / c\ (cm^2 g^{-1})$
10^{-1}
10^{-2}
10^{-3}
10^{-2}
$2x10^{-2}$
$3x10^{-2}$
q (nm^{-1})

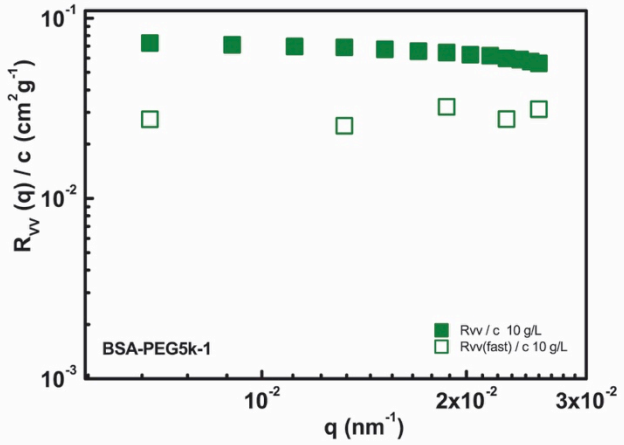
BSA-PEG5k-1
Rvv / c 10 g/L
Rvv(fast) / c 10 g/L
$R_{VV}(q) / c\ (cm^2 g^{-1})$
10^{-1}
10^{-2}
10^{-3}
10^{-2}
$2x10^{-2}$
$3x10^{-2}$
q (nm^{-1})

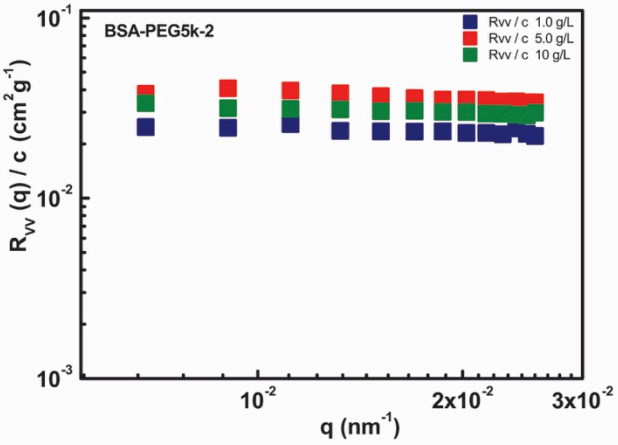
BSA-PEG5k-2
Rvv / c 1.0 g/L
Rvv / c 5.0 g/L
Rvv / c 10 g/L
R_{VV} (q) / c ($cm^2 g^{-1}$)
q (nm^{-1})

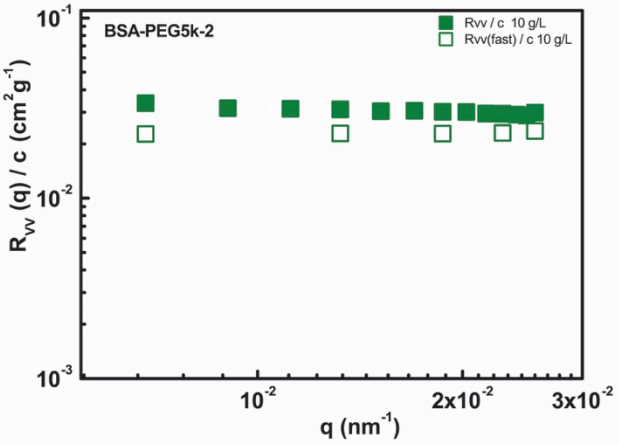
BSA-PEG5k-2
Rvv / c 10 g/L
Rvv(fast) / c 10 g/L
R_{VV} (q) / c ($cm^2 g^{-1}$)
q (nm^{-1})

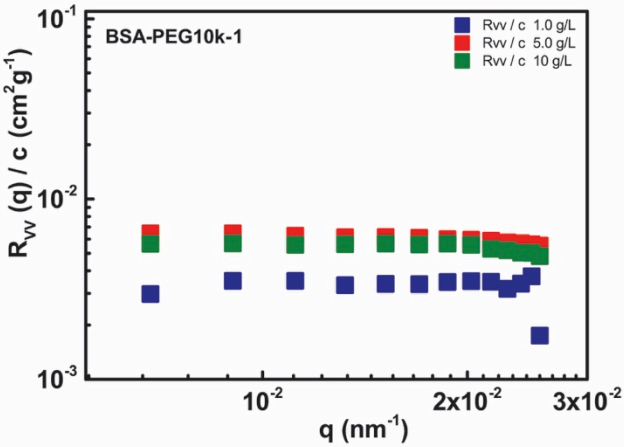
BSA-PEG10k-1
Rvv / c 1.0 g/L
Rvv / c 5.0 g/L
Rvv / c 10 g/L
R_{VV} (q) / c ($cm^2 g^{-1}$)
q (nm^{-1})

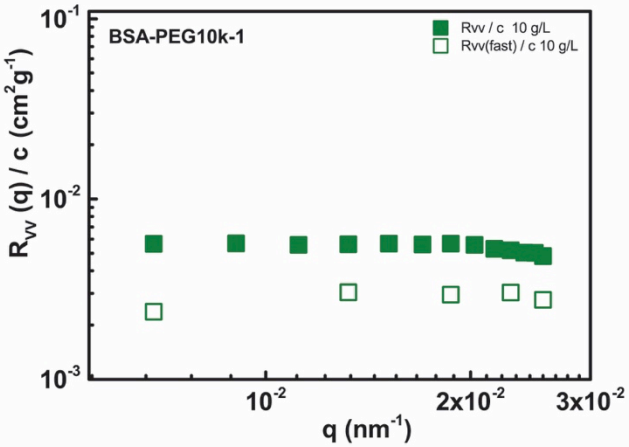
BSA-PEG10k-1
Rvv / c 10 g/L
Rvv(fast) / c 10 g/L
R_{VV} (q) / c ($cm^2 g^{-1}$)
q (nm^{-1})

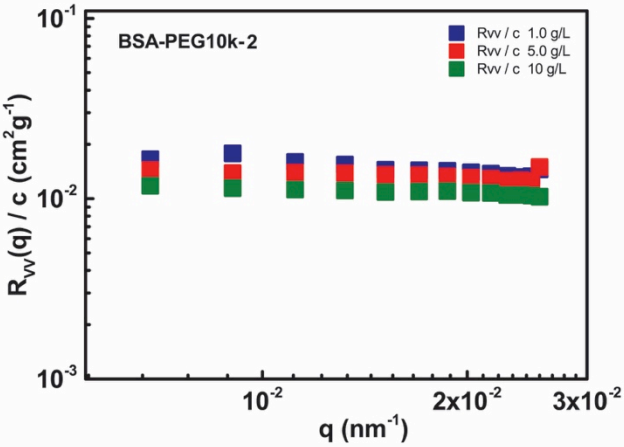
BSA-PEG10k-2
Rvv / c 1.0 g/L
Rvv / c 5.0 g/L
Rvv / c 10 g/L
R_{VV}(q) / c ($cm^2 g^{-1}$)
q (nm^{-1})

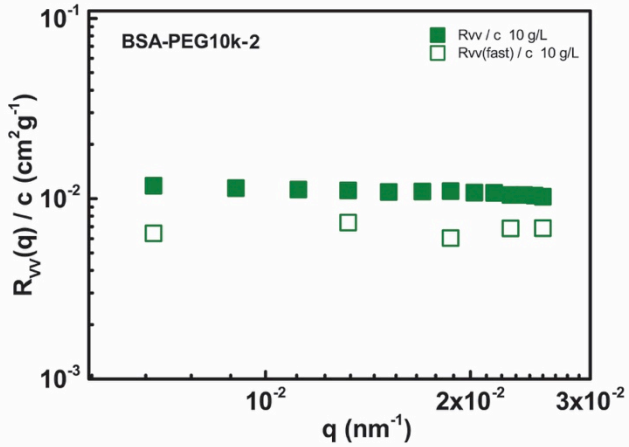
BSA-PEG10k-2
Rvv / c 10 g/L
Rvv(fast) / c 10 g/L
R_{VV}(q) / c ($cm^2 g^{-1}$)
q (nm^{-1})

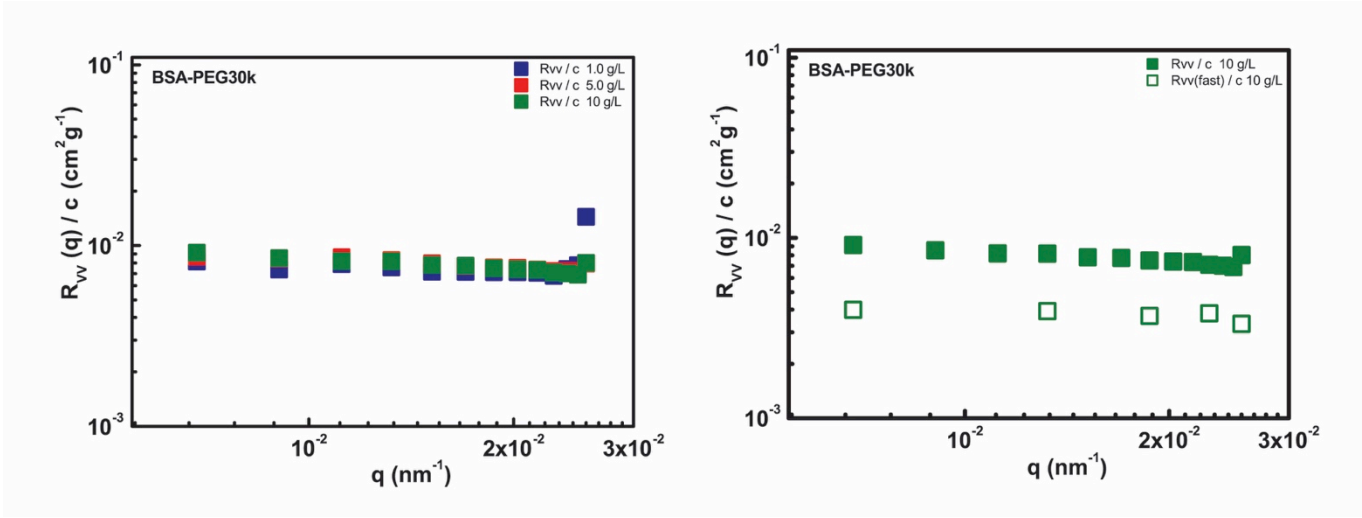
BSA-PEG30k
Rvv / c 1.0 g/L
Rvv / c 5.0 g/L
Rvv / c 10 g/L
R_{VV} (q) / c (cm^{2}g^{-1})
10^{-1}
10^{-2}
10^{-3}
10^{-2}
$2x10^{-2}$
$3x10^{-2}$
q (nm^{-1})
BSA-PEG30k
Rvv / c 10 g/L
Rvv(fast) / c 10 g/L
R_{VV} (q) / c (cm^{2}g^{-1})
10^{-1}
10^{-2}
10^{-3}
10^{-2}
$2x10^{-2}$
$3x10^{-2}$
q (nm^{-1})

Appendix C – DLS Data

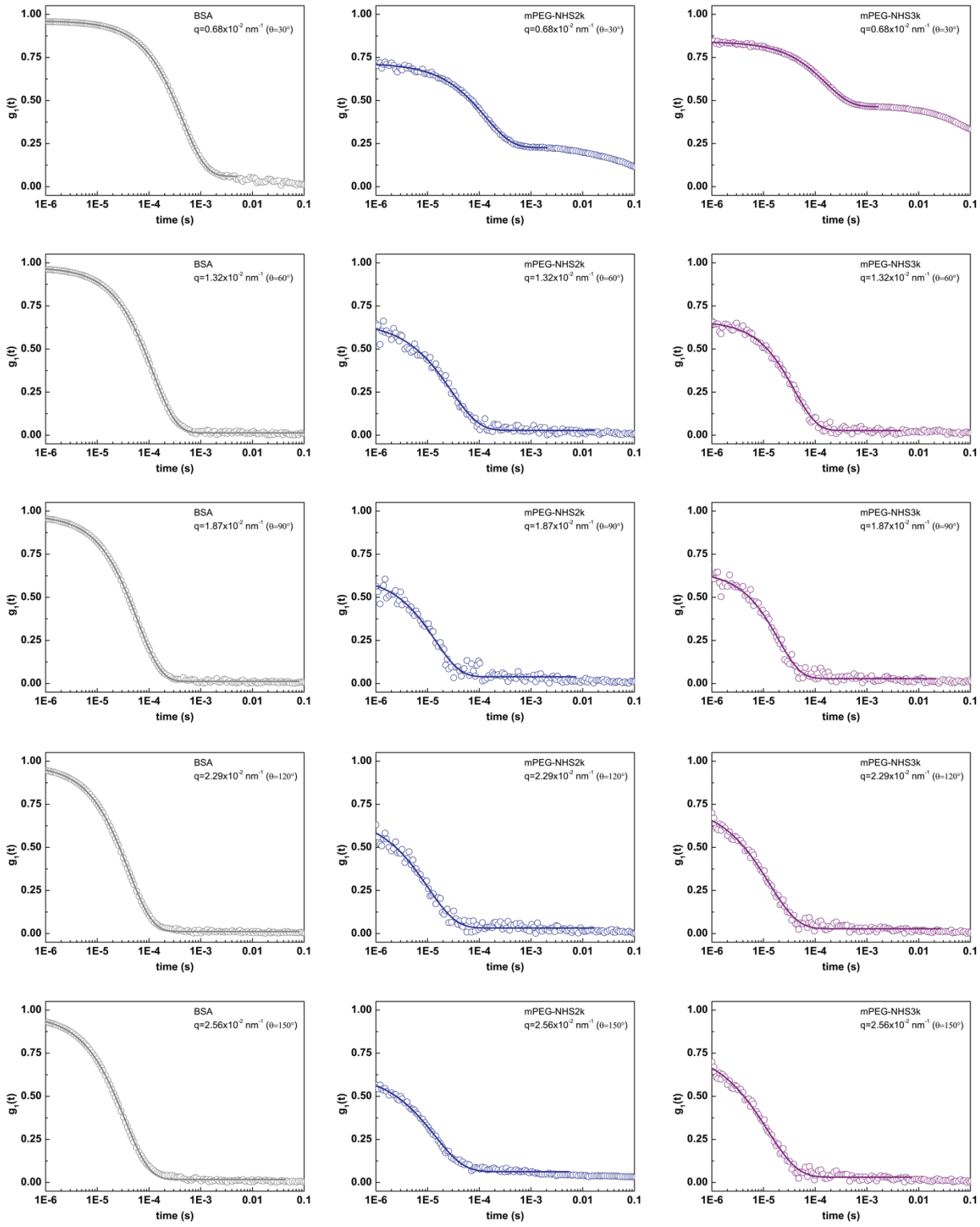

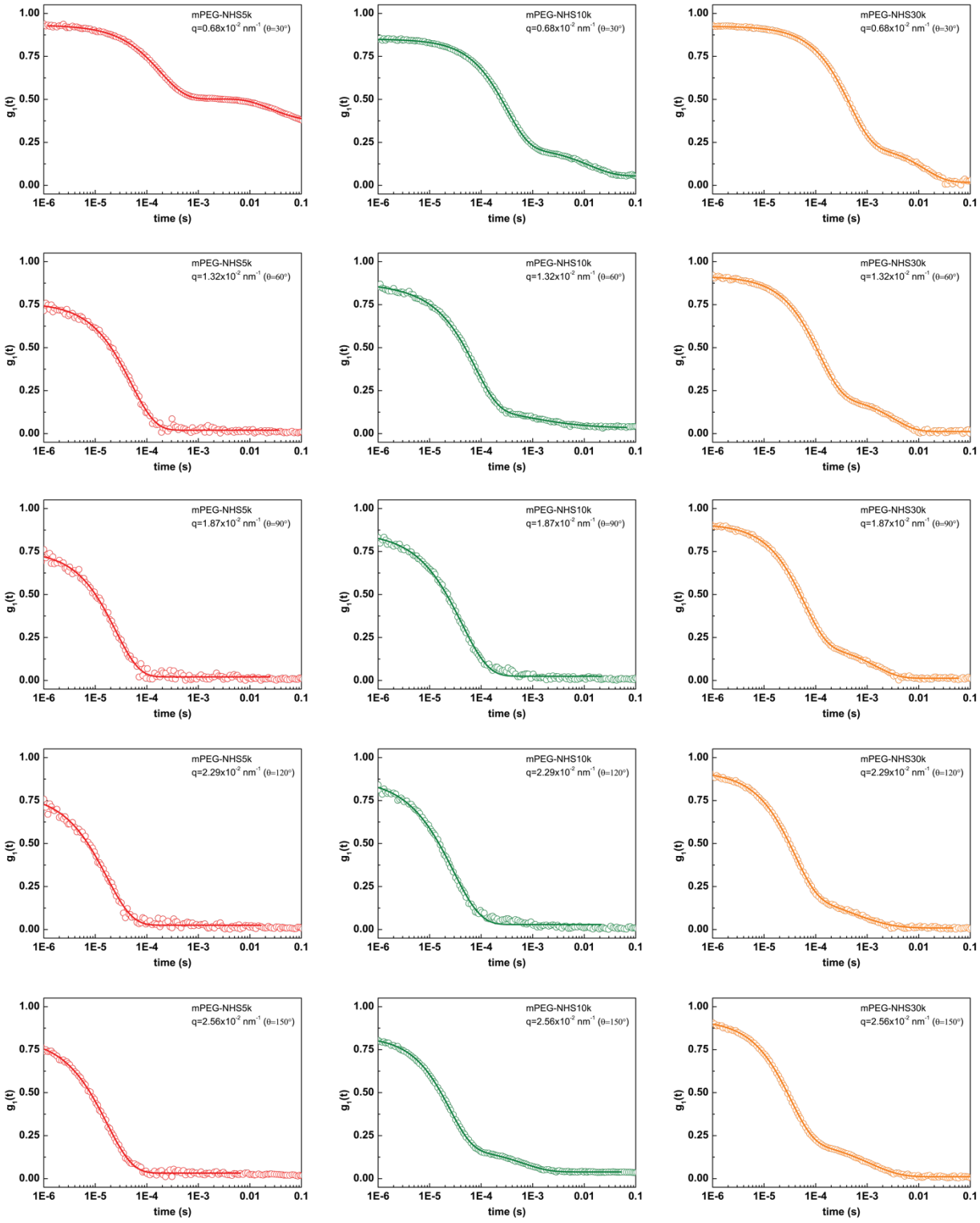
mPEG-NHS5k
q=0.68x10^{-2} nm^{-1} (θ=30°)
mPEG-NHS10k
q=0.68x10^{-2} nm^{-1} (θ=30°)
mPEG-NHS30k
q=0.68x10^{-2} nm^{-1} (θ=30°)
mPEG-NHS5k
q=1.32x10^{-2} nm^{-1} (θ=60°)
mPEG-NHS10k
q=1.32x10^{-2} nm^{-1} (θ=60°)
mPEG-NHS30k
q=1.32x10^{-2} nm^{-1} (θ=60°)
mPEG-NHS5k
q=1.87x10^{-2} nm^{-1} (θ=90°)
mPEG-NHS10k
q=1.87x10^{-2} nm^{-1} (θ=90°)
mPEG-NHS30k
q=1.87x10^{-2} nm^{-1} (θ=90°)
mPEG-NHS5k
q=2.29x10^{-2} nm^{-1} (θ=120°)
mPEG-NHS10k
q=2.29x10^{-2} nm^{-1} (θ=120°)
mPEG-NHS30k
q=2.29x10^{-2} nm^{-1} (θ=120°)
mPEG-NHS5k
q=2.56x10^{-2} nm^{-1} (θ=150°)
mPEG-NHS10k
q=2.56x10^{-2} nm^{-1} (θ=150°)
mPEG-NHS30k
q=2.56x10^{-2} nm^{-1} (θ=150°)
g$_1$(t)
time (s)
1.00
0.75
0.50
0.25
0.00
1E-6
1E-5
1E-4
1E-3
0.01
0.1

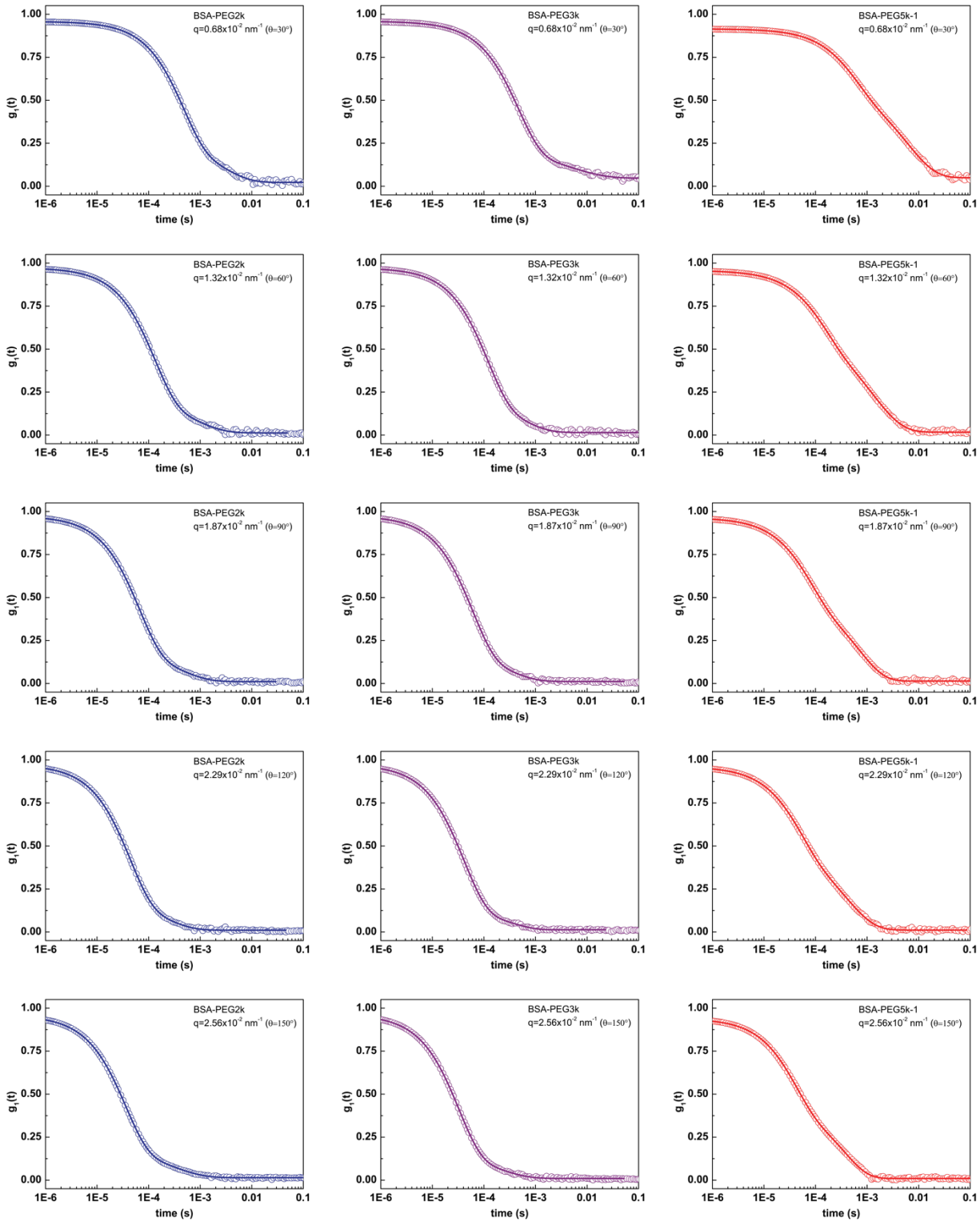
BSA-PEG2k
q=0.68x10-2 nm-1 (θ=30°)
BSA-PEG3k
q=0.68x10-2 nm-1 (θ=30°)
BSA-PEG5k-1
q=0.68x10-2 nm-1 (θ=30°)
BSA-PEG2k
q=1.32x10-2 nm-1 (θ=60°)
BSA-PEG3k
q=1.32x10-2 nm-1 (θ=60°)
BSA-PEG5k-1
q=1.32x10-2 nm-1 (θ=60°)
BSA-PEG2k
q=1.87x10-2 nm-1 (θ=90°)
BSA-PEG3k
q=1.87x10-2 nm-1 (θ=90°)
BSA-PEG5k-1
q=1.87x10-2 nm-1 (θ=90°)
BSA-PEG2k
q=2.29x10-2 nm-1 (θ=120°)
BSA-PEG3k
q=2.29x10-2 nm-1 (θ=120°)
BSA-PEG5k-1
q=2.29x10-2 nm-1 (θ=120°)
BSA-PEG2k
q=2.56x10-2 nm-1 (θ=150°)
BSA-PEG3k
q=2.56x10-2 nm-1 (θ=150°)
BSA-PEG5k-1
q=2.56x10-2 nm-1 (θ=150°)
g1(t)
time (s)
1.00
0.75
0.50
0.25
0.00
1E-6
1E-5
1E-4
1E-3
0.01
0.1

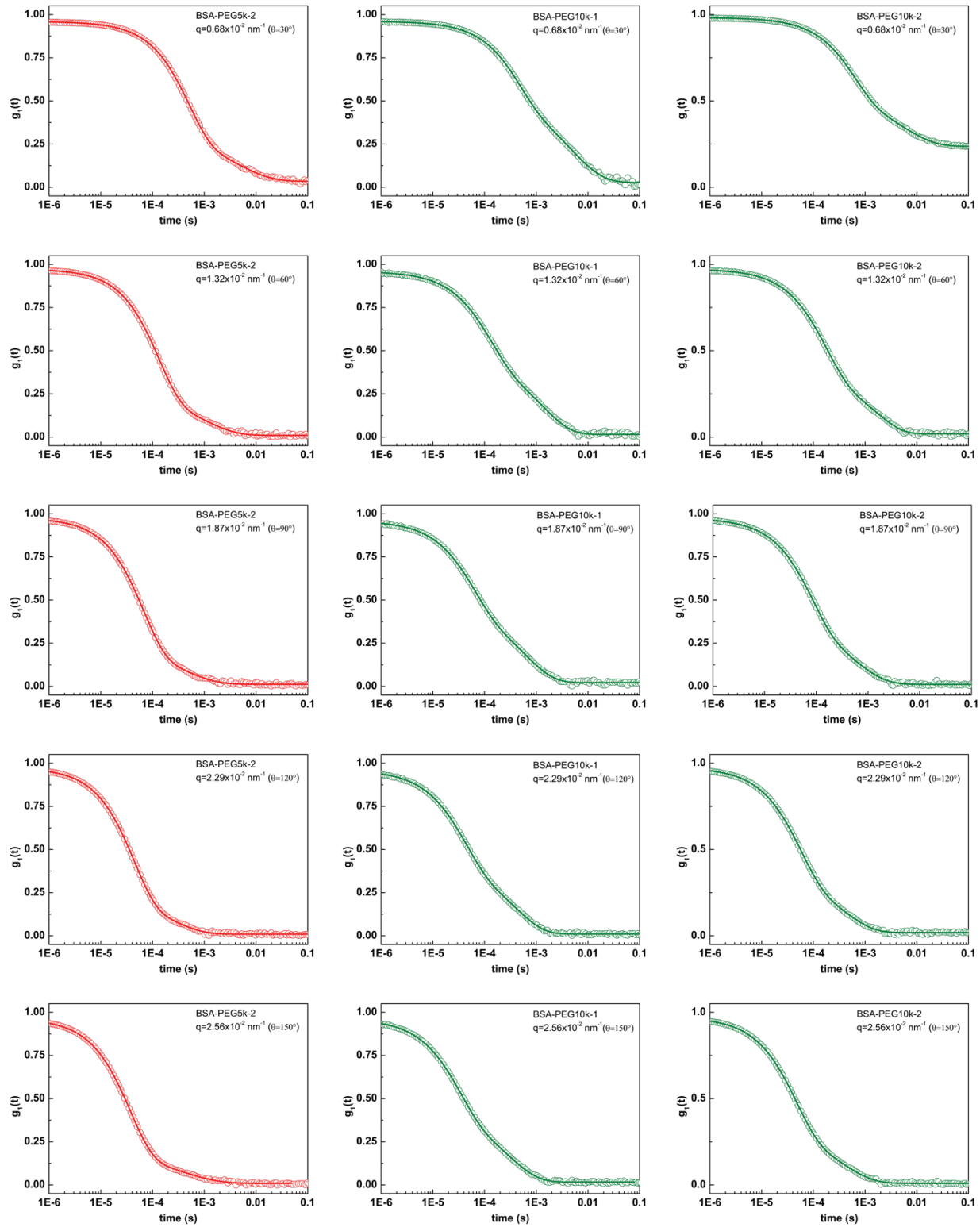
BSA-PEG5k-2
q=0.68x10-2 nm-1 (θ=30°)
BSA-PEG10k-1
q=0.68x10-2 nm-1 (θ=30°)
BSA-PEG10k-2
q=0.68x10-2 nm-1 (θ=30°)
BSA-PEG5k-2
q=1.32x10-2 nm-1 (θ=60°)
BSA-PEG10k-1
q=1.32x10-2 nm-1 (θ=60°)
BSA-PEG10k-2
q=1.32x10-2 nm-1 (θ=60°)
BSA-PEG5k-2
q=1.87x10-2 nm-1 (θ=90°)
BSA-PEG10k-1
q=1.87x10-2 nm-1 (θ=90°)
BSA-PEG10k-2
q=1.87x10-2 nm-1 (θ=90°)
BSA-PEG5k-2
q=2.29x10-2 nm-1 (θ=120°)
BSA-PEG10k-1
q=2.29x10-2 nm-1 (θ=120°)
BSA-PEG10k-2
q=2.29x10-2 nm-1 (θ=120°)
BSA-PEG5k-2
q=2.56x10-2 nm-1 (θ=150°)
BSA-PEG10k-1
q=2.56x10-2 nm-1 (θ=150°)
BSA-PEG10k-2
q=2.56x10-2 nm-1 (θ=150°)
g1(t)
time (s)
1E-6
1E-5
1E-4
1E-3
0.01
0.1

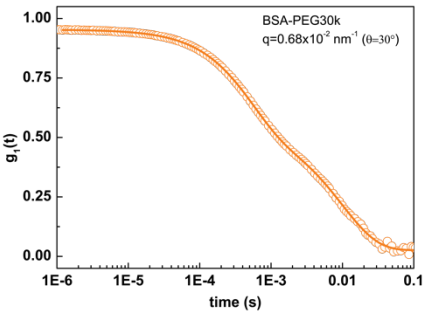
BSA-PEG30k
q=0.68x10-2 nm-1 (θ=30°)
g1(t)
time (s)

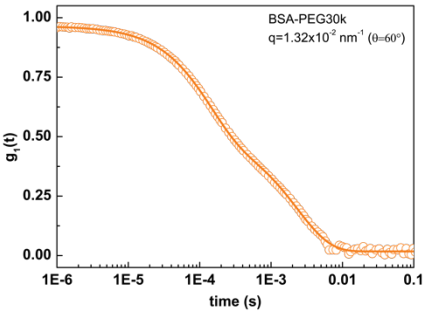
BSA-PEG30k
q=1.32x10-2 nm-1 (θ=60°)
g1(t)
time (s)

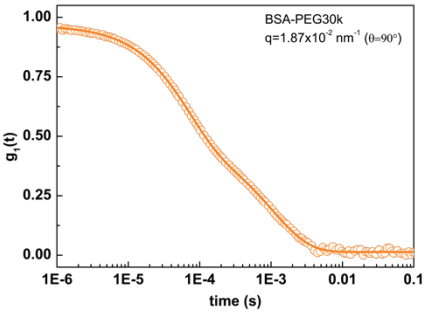
BSA-PEG30k
q=1.87x10-2 nm-1 (θ=90°)
g1(t)
time (s)

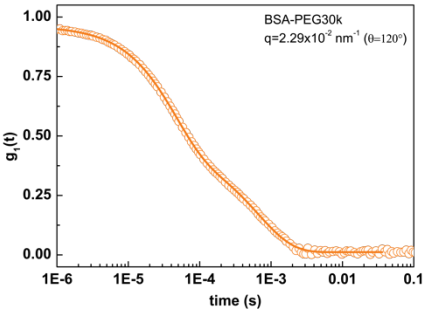
BSA-PEG30k
q=2.29x10-2 nm-1 (θ=120°)
g1(t)
time (s)

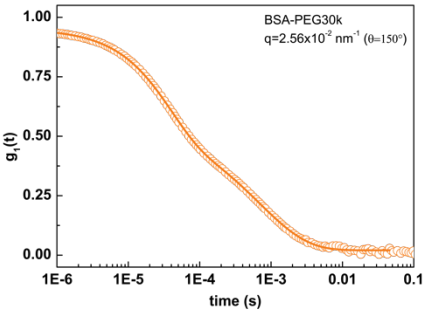
BSA-PEG30k
q=2.56x10-2 nm-1 (θ=150°)
g1(t)
time (s)

Appendix D – References

[1] A. Akthakul, A. Hochbaum, F. Stellacci, A. Mayes, *Adv. Mater.* **2005**, *17*, 532.

[2] K.-V. Peinemann, V. Abetz, P. F. W. Simon, *Nat. Mater.* **2007**, *6*, 992.

[3] M. M. Pendergast, R. Mika Dorin, W. Phillip, U. Wiesner, E. M. V Hoek, *J. Memb. Sci.* **2013**, *444*, 461.

[4] R. M. Dorin, H. Sai, U. Wiesner, *Chem. Mater.* **2014**, *26*, 339.

[5] W. Phillip, R. Mika Dorin, J. Werner, E. M. V Hoek, U. Wiesner, M. Elimelech, *Nano Lett.* **2011**, *11*, 2892.

[6] R. M. Dorin, W. Phillip, H. Sai, J. Werner, M. Elimelech, U. Wiesner, *Polymer.* **2014**, *55*, 347.

[7] M. J. Roberts, M. D. Bentley, J. M. Harris, *Adv. Drug Deliv. Rev.* **2012**, *64*, 116.

[8] A. Abuchowski, J. R. McCoy, N. C. Palczuk, T. van Es, F. F. Davis, *J. Biol. Chem.* **1977**, *252*, 3582.

[9] S. Cohen, T. Yoshioka, M. Lucarelli, L. H. Hwang, R. Langer, *Pharm. Res.* **1991**, *8*, 713.

[10] S. Syed, P. Schuyler, M. Kulczycky, W. Sheffield, *Blood* **1997**, *89*, 3243.

[11] J. Lyczak, S. Morrison, *Arch. Virol.* **1994**, *139*, 189.

[12] C. Mateo, J. Lombardero, E. Moreno, A. Morales, G. Bombino, J. Coloma, L. Wims, S. Morrison, R. Pérez, *Hybridoma* **2000**, *19*, 463.

[13] I. F. Hakem, A. M. Leech, J. Bohn, J. P. Walker, M. R. Bockstaller, *Biopolymers* **2013**, *99*, 427.

[14] M. Rubinstein, R. Colby, *Polymer Physics*, Oxford University Press, New York City, **2003**.

[15] P. Painter, M. Coleman, *Essentials of Polymer Science and Engineering*, DEStech Publications, **2008**.

[16] W. Brown, *Light Scattering Principles and Development*, Oxford University Press, New York City, **1996**.

[17] L. He, H. Wang, V. M. Garamus, T. Hanley, M. Lensch, H. J. Gabius, C. J. Fee, A. Middelberg, *Biomacromolecules* **2010**, *11*, 3504.

[18] J. Y. Shu, B. Panganiban, T. Xu, *Annu. Rev. Phys. Chem.* **2013**, *64*, 631.

[19] H. G. Börner, H. Schlaad, *Soft Matter* **2007**, *3*, 394.

[20] H.-A. Klok, G. W. M. Vandermeulen, H. Nuhn, A. Rösler, I. W. Hamley, V. Castelletto, H. Xu, S. S. Sheiko, *Faraday Discuss.* **2005**, *128*, 29.

[21] T. J. Deming, *Adv. Mater.* **1997**, *9*, 299.

[22] W. Petka, J. L. Harden, K. P. McGrath, D. Wirtz, D. Tirrell, *Science.* **1998**, *281*, 389.

[23] C. Wang, R. J. Stewart, J. Kopecek, *Nature* **1999**, *397*, 417.

[24] J. D. Hartgerink, E. Beniash, S. Stupp, *Science.* **2001**, *649*, 1684.

[25] A. P. Nowak, V. Breedveld, L. Pakstis, B. Ozbas, D. J. Pine, D. Pochan, T. J. Deming, *Nature* **2002**, *417*, 424.

[26] M. Sarikaya, C. Tamerler, D. T. Schwartz, F. Baneyx, *Annu. Rev. Mater. Res.* **2004**, *34*, 373.

[27] G. W. M. Vandermeulen, D. Hinderberger, H. Xu, S. S. Sheiko, G. Jeschke, H. A. Klok, *ChemPhysChem* **2004**, *5*, 488.

[28] J. Y. Shu, C. Tan, W. F. DeGrado, T. Xu, *Biomacromolecules* **2008**, *9*, 2111.

[29] L. C. Palmer, S. I. Stupp, *Acc. Chem. Res.* **2008**, *41*, 1674.

[30] S. Zhang, *Nat. Biotechnol.* **2003**, *21*, 1171.

[31] S. V. Kazakov, I. Y. Galaev, B. Mattiasson, *Int. J. Thermophys.* **2002**, *23*, 161.

[32] Y. Park, G. Choi, *Korean J. Chem. Eng.* **2009**, *26*, 193.

[33] D. Knolls, J. Hermans, *J. Biol. Chem.* **1983**, *258*, 5710.

[34] Y. Moon, R. Curtis, C. Anderson, H. Blanch, J. Prausnitz, *J. Solution Chem.* **2000**, *29*, 699.

[35] V. L. Vilker, C. K. Colton, K. a Smith, *J. Colloid Interface Sci.* **1981**, *79*, 548.

[36] A. George, W. W. Wilson, *Acta Crystallogr. D. Biol. Crystallogr.* **1994**, *50*, 361.

[37] C. Haynes, R. Beynon, R. King, H. Blanch, J. Prausnitz, *J. Phys. Chem.* **1989**, *93*, 5612.

[38] H. Hasse, H.-P. Kany, R. Tintinger, G. Maurer, *Macromolecules* **1995**, *28*, 3540.

[39] J. Bloustine, T. Virmani, G. M. Thurston, S. Fraden, *Phys. Rev. Lett.* **2006**, *96*, 1.

[40] F. M. Veronese, *Biomaterials* **2001**, *22*, 405.

[41] R. Clark, K. Olson, G. Fuh, M. Marian, D. Mortensen, G. Teshima, S. Chang, H. Chu, V. Mukku, E. Canova-Daivs, T. Somers, M. Cronin, M. Winkler, J. Wells, *J. Biol. Chem.* **1996**, *271*, 21969.

[42] A. Matsushima, H. Nishimura, Y. Ashihara, Y. Yokota, Y. Inada, *Chem. Lett.* **1980**, 773.

[43] H.-J. Gais, S. Ruppert, *Tetrahedron Lett.* **1995**, *36*, 3837.

[44] T. Miron, M. Wilchek, *Bioconjug. Chem.* **1993**, *4*, 568.

[45] C. O. Beauchamp, S. L. Gonias, D. P. Menapace, S. V Pizzo, *Anal. Biochem.* **1983**, *131*, 25.

[46] M. C. Carter, M. E. Meyerhoff, *J. Immunol. Methods* **1985**, *81*, 245.

[47] D. G. Mullen, M. M. Banaszak Holl, *Acc. Chem. Res.* **2011**, *44*, 1135.

[48] D. G. Mullen, M. Fang, A. Desai, J. R. Baker, B. G. Orr, M. M. Banaszak Holl, *ACS Nano* **2010**, *4*, 657.

[49] I. F. Hakem, A. M. Leech, J. D. Johnson, S. J. Donahue, J. P. Walker, M. R. Bockstaller, *J. Am. Chem. Soc.* **2010**, *132*, 16593.

[50] F. S. Bates, G. H. Fredrickson, *Annu. Rev. Phys. Chem.* **1990**, *41*, 525.

[51] I. W. Hamley, *Introduction to Block Copolymers*, John Wiley & Sons, Ltd., **2004**.

[52] C. M. Bates, M. J. Maher, D. W. Janes, C. J. Ellison, C. G. Willson, *Macromolecules*

2014, *47*, 2.

[53] D. Trimbach, K. Feldman, N. D. Spencer, D. J. Broer, C. W. M. Bastiaansen, *Langmuir* **2003**, *19*, 10957.

[54] M. Park, C. Harrison, P. M. Chaikin, R. A. Register, D. H. Adamson, *Science.* **1997**, *276*, 1401.

[55] P. G. Ferreira, L. Leibler, *J. Chem. Phys.* **1996**, *105*, 9362.

[56] P. G. Ferreira, A. Ajdari, L. Leibler, *Macromolecules* **1998**, *31*, 3994.

[57] R. B. Thompson, V. V Ginzburg, M. W. Matsen, A. C. Balazs, *Science.* **2001**, *292*, 2469.

[58] M. R. Bockstaller, R. A. Mickiewicz, E. L. Thomas, *Adv. Mater.* **2005**, *17*, 1331.

[59] H. Tanaka, H. Hasegawa, T. Hashimoto, *Macromolecules* **1991**, *24*, 240.

[60] K. I. Winey, E. L. Thomas, L. J. Fetters, *Macromolecules* **1991**, *24*, 6182.

[61] J. J. Chiu, B. J. Kim, E. J. Kramer, D. J. Pine, *J. Am. Chem. Soc.* **2005**, *127*, 5036.

[62] J. Listak, I. F. Hakem, H. J. Ryu, S. Rangou, N. Politakos, K. Misichronis, A. Avgeropoulos, M. R. Bockstaller, *Macromolecules* **2009**, *42*, 5766.

[63] D. Dukes, Y. Li, S. Lewis, B. Benicewicz, L. Schadler, S. K. Kumar, *Macromolecules* **2010**, *43*, 1564.

[64] P. Voudouris, J. Choi, N. Gomopoulos, R. Sainidou, H. Dong, K. Matyjaszewski, M. R. Bockstaller, G. Fytas, *ACS Nano* **2011**, *5*, 5746.

[65] J. Choi, C. M. Hui, J. Pietrasik, H. Dong, K. Matyjaszewski, M. R. Bockstaller, *Soft Matter* **2012**, *8*, 4072.

[66] J. Pietrasik, C. M. Hui, W. Chaladaj, H. Dong, J. Choi, J. Jurczak, M. R. Bockstaller, K. Matyjaszewski, *Macromol. Rapid Commun.* **2011**, *32*, 295.

[67] J. Malmström, J. Travas-Sejdic, *J. Appl. Polym. Sci.* **2014**, *131*, 1.

[68] D. Liu, T. Wang, J. L. Keddie, *Langmuir* **2009**, *25*, 4526.

[69] C. S. Thomas, M. J. Glassman, B. D. Olsen, *ACS Nano* **2011**, *5*, 5697.

[70] C. S. Thomas, L. Xu, B. D. Olsen, *Biomacromolecules* **2012**, *13*, 2781.

[71] C. N. Lam, M. Kim, C. S. Thomas, D. Chang, G. E. Sanoja, C. U. Okwara, B. D. Olsen, *Biomacromolecules* **2014**, *15*, 1248.

[72] A. D. Presley, J. J. Chang, T. Xu, *Soft Matter* **2011**, *7*, 172.

[73] Y. Lin, A. C. Balazs, T. P. Russell, *Nature* **2005**, *434*, 55.

[74] Y. Hu, D. Samanta, S. S. Parelkar, S. W. Hong, Q. Wang, T. P. Russell, T. Emrick, *Adv. Funct. Mater.* **2010**, *20*, 3603.

[75] P.-C. Tsai, N. Fox, A. N. Bigley, S. P. Harvey, D. P. Barondeau, F. M. Raushel, *Biochemistry* **2012**, *51*, 6463.

[76] I. Cherny, P. Greisen, Y. Ashani, S. D. Khare, G. Oberdorfer, H. Leader, D. Baker, D. S. Tawfik, *ACS Chem. Biol.* **2013**, *8*, 2394.

[77] R. M. Dorin, D. S. Marques, H. Sai, U. Vainio, W. A. Phillip, K.-V. Peinemann, S. P.

Nunes, U. Wiesner, *ACS Macro Lett.* **2012**, *1*, 614.

[78] A. Oh, *Heat Mass Transf.* **2007**, *44*, 375.

[79] H. Xu, J. L. Kaar, A. J. Russell, W. R. Wagner, *Biomaterials* **2006**, *27*, 3125.

[80] *British Standard 7209 - Specification for Water Vapour Permeable Apparel Fabrics*, **1990**.

[81] N. E. Clough, *ePTFE Innov. Pap.* **2009**, 1.

[82] Y. Fink, A. M. Urbas, M. G. Bawendi, J. D. Joannopoulos, E. L. Thomas, *J. Light. Technol.* **1999**, *17*, 1963.

[83] R. L. Bruce, F. Weilnboeck, T. Lin, R. J. Phaneuf, G. S. Oehrlein, B. K. Long, C. G. Willson, A. Alizadeh, *J. Vac. Sci. Technol. B Microelectron. Nanom. Struct.* **2011**, *29*, 041604.

[84] J. Vörös, *Biophys. J.* **2004**, *87*, 553.

[85] A. Fisher, M. Labenski, T. Monks, S. Lau, in *Methods Mol. Biol.*, **2011**, pp. 303–316.

[86] L. Sawyer, D. Grubb, G. Meyers, *Polymer Microscopy*, Springer New York, New York, **2008**.

[87] J. Calderone, *Sci. Am.* **2014**, *312*, 19.

[88] M. a C. Stuart, W. T. S. Huck, J. Genzer, M. Müller, C. Ober, M. Stamm, G. B. Sukhorukov, I. Szleifer, V. V Tsukruk, M. Urban, F. Winnik, S. Zauscher, I. Luzinov, S. Minko, *Nat. Mater.* **2010**, *9*, 101.

[89] P. J. Schatz, *Bio/technology* **1993**, *11*, 1138.

[90] B. D. Moore, L. Stevenson, A. Watt, S. Flitsch, N. J. Turner, C. Cassidy, D. Graham, *Nat. Biotechnol.* **2004**, *22*, 1133.

[91] D. J. Woo, S. K. Obendorf, *RSC Adv.* **2014**, *4*, 15727.

[92] E. López-Maya, C. Montoro, L. M. Rodríguez-Albelo, S. D. Aznar Cervantes, A. A. Lozano-Pérez, J. L. Cenís, E. Barea, J. A. R. Navarro, *Angew. Chemie Int. Ed.* **2015**, *54*, 6790.

[93] J. Zhu, G. Sun, *RSC Adv.* **2014**, *4*, 50858.

[94] A. Singh, Y. Lee, W. J. Dressick, *Adv. Mater.* **2004**, *16*, 2112.

[95] Y. J. Rosenberg, J. Walker, X. Jiang, S. Donahue, J. Robosky, M. Sack, J. Lees, L. Urban, *Sci. Rep.* **2015**, *5*, 13247.

[96] A. N. Bigley, C. Xu, T. J. Henderson, S. P. Harvey, F. M. Raushel, *J Am Chem Soc* **2013**, *135*, 10426.

[97] R. Maki-Ontto, K. de Moel, W. Odorico, M. Stamm, *Adv. Mater.* **2001**, *13*, 117.

[98] H. Lee, W. Akers, K. Bhushan, S. Bloch, G. Sudlow, R. Tang, S. Achilefu, *Bioconjug. Chem.* **2011**, *22*, 777.

[99] B. Plesner, C. J. Fee, P. Westh, A. D. Nielsen, *Eur. J. Pharm. Biopharm.* **2011**, *79*, 399.

[100] P. Bailon, A. Palleroni, C. A. Schaffer, C. L. Spence, W. J. Fung, J. E. Porter, G. K. Ehrlich, W. Pan, Z. X. Xu, M. W. Modi, A. Farid, W. Berthold, *Bioconjug. Chem.* **2001**,

12, 195.

[101] S. S. Pai, B. Hammouda, K. Hong, D. C. Pozzo, T. M. Przybycien, R. D. Tilton, *Bioconjug. Chem.* **2011**, *22*, 2317.

[102] G. Digilio, L. Barbero, C. Bracco, D. Corpillo, P. Esposito, G. Piquet, S. Traversa, S. Aime, *J. Am. Chem. Soc.* **2003**, *125*, 3458.

[103] A. Abuchowski, T. van Es, N. C. Palczuk, F. F. Davis, *J. Biol. Chem.* **1977**, *252*, 3578.

[104] R. B. Greenwald, Y. H. Choe, J. McGuire, C. D. Conover, *Adv. Drug Deliv. Rev.* **2003**, *55*, 217.

[105] C. J. Fee, J. M. Van Alstine, *Bioconjug. Chem.* **2004**, *15*, 1304.

[106] J. M. Harris, R. B. Chess, *Nat. Rev. Drug Discov.* **2003**, *2*, 214.

[107] M. J. Roberts, M. D. Bentley, J. M. Harris, *Adv. Drug Deliv. Rev.* **2002**, *54*, 459.

[108] B. N. Manjula, A. Tsai, R. Upadhya, K. Perumalsamy, P. K. Smith, A. Malavalli, K. Vandegriff, R. M. Winslow, M. Intaglietta, M. Prabhakaran, J. M. Friedman, A. S. Acharya, *Bioconjug. Chem.* **2003**, *14*, 464.

[109] A. S. Morar, J. R. L. Schrimsher, M. D. Chavez, *Biopharm Int.* **2006**, *19*, 1.

[110] H. García-Arellano, B. Valderrama, G. Saab-Rincón, R. Vazquez-Duhalt, *Bioconjug. Chem.* **2002**, *13*, 1336.

[111] D. Li, B. N. Manjula, A. S. Acharya, *Protein J.* **2006**, *25*, 263.

[112] C. Le Cœur, S. Combet, G. Carrot, P. Busch, J. Teixeira, S. Longeville, *Langmuir* **2015**, *31*, 8402.

[113] C. Haas, J. Drenth, W. W. Wilson, *J. Phys. Chem. B* **1999**, *103*, 2808.

[114] W. W. Wilson, L. J. DeLucas, *Acta Crystallogr. Sect. F* **2014**, *70*, 543.

[115] M. Kerker, *The Scattering of Light and Other Electromagnetic Radiation*, **1969**.

[116] H. B. Lu, C. T. Campbell, D. G. Castner, *Langmuir* **2000**, *16*, 1711.

[117] F. Perrin, *J. Chem. Phys.* **1942**, *10*, 415.

[118] B. Berne, R. Pecora, *Dynamic Light Scattering: With Applications to Chemistry, Biology, and Physics*, **2013**.

[119] F. Veronese, P. Caliceti, O. Schiavon, *J. Bioact. Compat. Polym.* **1997**, *12*, 196.

[120] B. Hamdoun, D. Ausserré, V. Cabuil, S. Joly, *J. Phys. II* **1996**, *6*, 503.

[121] G. K. Xu, X. Q. Feng, S. W. Yu, *Nano Res.* **2010**, *3*, 356.

[122] P. J. Costanzo, F. L. Beyer, *Macromolecules* **2007**, *40*, 3996.

[123] R. Stadler, C. Auschra, J. Beckmann, U. Krappe, I. Voigt-Martin, L. Leibler, *Macromolecules* **1995**, *28*, 3080.

[124] J. A. Brydson, in *Plast. Mater.*, **1999**, pp. 72–105.

[125] Q. W. Yuan-Huffman, in *Polym. Handb.*, **2009**, pp. 690–700.

[126] J. Guo, P. Andre, M. Adam, S. Panyukov, M. Rubinstein, J. M. DeSimone, *Macromolecules* **2006**, *39*, 3427.

[127] B. Jachimska, M. Wasilewska, Z. Adamczyk, *Langmuir* **2008**, *24*, 6866.